論文 / 著書情報
Article / Book Information

題目(和文)	
Title(English)	Mechanics of paraffin droplet impacted and solidified on metal substrate
著者(和文)	康 超
Author(English)	Chao Kang
出典(和文)	学位:博士（工学）, 学位授与機関:東京工業大学, 報告番号:甲第11740号, 授与年月日:2022年3月26日, 学位の種別:課程博士, 審査員:阪口 基己,轟 章,佐藤 千明,伏信 一慶,井上 裕嗣
Citation(English)	Degree:Doctor (Engineering), Conferring organization: Tokyo Institute of Technology, Report number:甲第11740号, Conferred date:2022/3/26, Degree Type:Course doctor, Examiner:,,,,
学位種別(和文)	博士論文
Type(English)	Doctoral Thesis

Doctoral Dissertation

Mechanics of paraffin droplet impacted and solidified on metal substrate

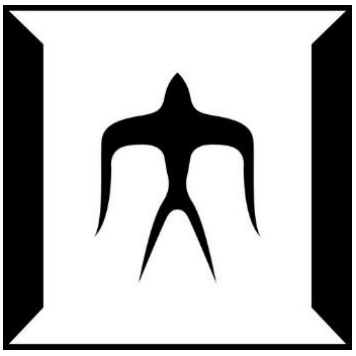

Tokyo Institute of Technology

Supervisors

Assoc. Prof. Motoki Sakaguchi

Prof. Hirotsugu Inoue

Chao Kang

February 2022

Abstract

Residual stress is inevitably generated during thermal spraying and plays a critical role in the performance of thermal barrier coatings. It is of great significance to understand the mechanisms of stress evolution and fracture behaviors in thermal sprayed coatings. In this dissertation, a model experiment was carried out to evaluate the mechanics of paraffin droplets during the impact, solidification, and cooling process, which partly simulated the deposition of thermal spray particles. In the experiment, molten paraffin droplet was dropped onto a pre-cooled 430 stainless steel substrate. Evolutions of strain and temperature at the substrate back surface were measured by a bi-axial strain gauge and several thermocouples, respectively. During the solidification and cooling process of the paraffin droplet, tensile residual strain was developed at the substrate back surface. Effects of substrate pre-set temperature, drop height (impact velocity), droplet temperature, and paraffin wax materials on the residual strains were fully investigated. Experimental results suggested that the residual strains increase with the reduction of substrate pre-set temperature, drop height, and droplet temperature. Cracking and debonding were observed in solidified splats depending on the experimental conditions.

An elastic finite element (FE) analysis was conducted to calculate the distribution of splat stress and interfacial stresses as driving forces for cracking and debonding, respectively. Comparison between calculated splat stress and paraffin's tensile strength provided a reasonable explanation for the cracking behaviors observed in the splats. Interfacial debonding criteria were estimated by comparing the calculated interfacial stresses and observed debonding behaviors. Coupled thermo-mechanical FE analysis was then performed to calculate the evolutions of residual strain and substrate temperature during the solidification and cooling process of paraffin droplets. The effect of creep of solidified splat was considered by using a strain hardening form of creep law, in which the creep properties were measured by a four-point bending method. Calculation results revealed that creep deformation is a critical factor influencing the stress-strain evolution. Based on the calculation results, the effect of interfacial adhesion on residual strains was

investigated considering several drop impact conditions. It verified that a poor adhesion at the splat/substrate interface induced a higher degree of stress relaxation.

Debonding of solidified splat with a substrate is a crucial issue dominating the reliability of thermal sprayed coatings and was therefore specifically investigated. It was found that the debonding is prone to take place at lower substrate pre-set temperature, lower drop height, and lower droplet temperature. A scraping method was employed to measure the adhesion strength of splats formed under various impact conditions. The results showed good accordance with debonding behaviors in drop impact experiments. The scraping tests also indicated that the residual tensile stress in splats reduces the scraping forces, and prevents the complete removal of splats during the scraping process. Numerical results of stress distributions along splat/substrate interface coupled with scraping tests provided reasonable explanations for observed debonding behaviors of single splats.

Based on the model experiments and numerical simulations, the evolution of residual strain, cracking and debonding behaviors, and splat/substrate adhesion strength was fully discussed considering the effects of several experimental conditions. Findings from a series of experiments and analyses showed some similarities to actual phenomena during thermal spraying. These can help to understand the fundamental mechanisms of the deposition of single particles and provide important guidance for optimizing thermal spraying processes.

Contents

Chapter 1

Introduction

1.1 Industrial manufacturing processes with solidification and thermal stress development

Solidification is a common phenomenon that exists in a diverse range of industrial processes, such as casting [1, 2], welding [3, 4], 3-dimensional (3D) printing [5, 6], and thermal spraying [7, 8]. Casting is a highly economic and important manufacturing techniques. It is a simple process in which liquid materials are poured into the cavity of mold and then cooled down. Sand casting, investment casting, plaster casting, and die casting are the most popular types of casting processes. Welding is one of the most well-known methods for the joining of metallic or thermoplastic materials through melting materials in the area of joint. Welding is applied in wide areas of applications such as aerospace engineering [9], metro transport systems [10], and the automotive industry [11]. 3D printing is a relatively new manufacturing technique, which was initially introduced by C. Hull [12] in the 1980s, and widely available commercially in the last decade. It has become one of the most revolutionary and popular manufacturing tools because of its ability to precisely fabricate complex 3D objects [13]. Thermal spraying is a group of processes using a heat source to melt metallic or nonmetallic materials and spray them on a pre-heated substrate to produce a dense coating. The most common thermal spraying processes are atmospheric plasma spraying (APS) [14], high-velocity oxy-fuel coating spraying (HVOF) [15], wire arc spraying [16], and flame spraying [17]. They are widely used in many industrial areas, such as aerospace engineering and the semiconductor industry.

In these manufacturing processes, the phase transformation from liquid to solid is one of the most significant matters that should be particularly noted. This is because thermal and

mechanical properties usually vary remarkably between two different phases, which may result in many problems due to phase change. For example, high temperature in the welding process, and thermal shrinkage occurring during the solidification and cooling process, always result in severe deformations and extreme residual stresses, which may influence the performance of welded structures [18, 19]. The properties of thermal sprayed coatings such as adhesion strength and adherence to the substrate are significantly affected by local micro-cracks, interfacial delamination, and debonding due to the relaxation of residual stresses generated within the sprayed coatings [20]. Hence, it is of great significance to understand the mechanisms of residual stress evolution and predict the levels of deformation and residual stresses those are taken place during the solidification and cooling processes of liquid materials.

1.2 Residual stress during thermal spraying

Thermal spraying is one of the most common coating methods for adding thermal, wear, erosion, or corrosion resistance onto various industrial components such as turbine blades [21], automotive engines [22], and power generation system equipment [23]. During thermal spraying, coating feedstock materials are heated and sprayed onto solid substrates in the form of molten or semi-molten particles to fabricate a dense coating [24]. Thermal barrier coatings (TBCs) are widely employed as protective coatings against high temperature environments [25]. TBCs can typically achieve a temperature reduction of 200 °C for the coated substrate, which is mainly attributed to its low thermal conductivity as illustrated in Fig. 1.1 [26].

APS is one of the most popular methods to manufacture TBCs [27], in which a plasma jet is used to spray and deposit coating materials onto a metallic substrate in the form of molten particles. A typical plasma spraying process is illustrated in Fig. 1.2 [28]. During the impact, solidification, and cooling process of sprayed particles, residual stress is inevitably built up in the coatings. This residual stress plays a critical role in the cracking

and debonding of TBCs during the operation period [29, 30-33]. Many investigations have been made to clarify the development of residual stress during thermal spraying [24, 27, 34-40].

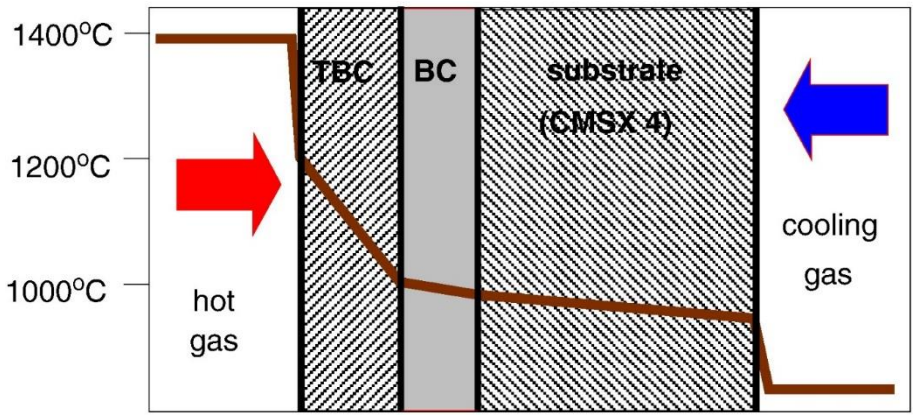

Fig. 1.1 Temperature reduction due to TBC system. Adapted from [26].

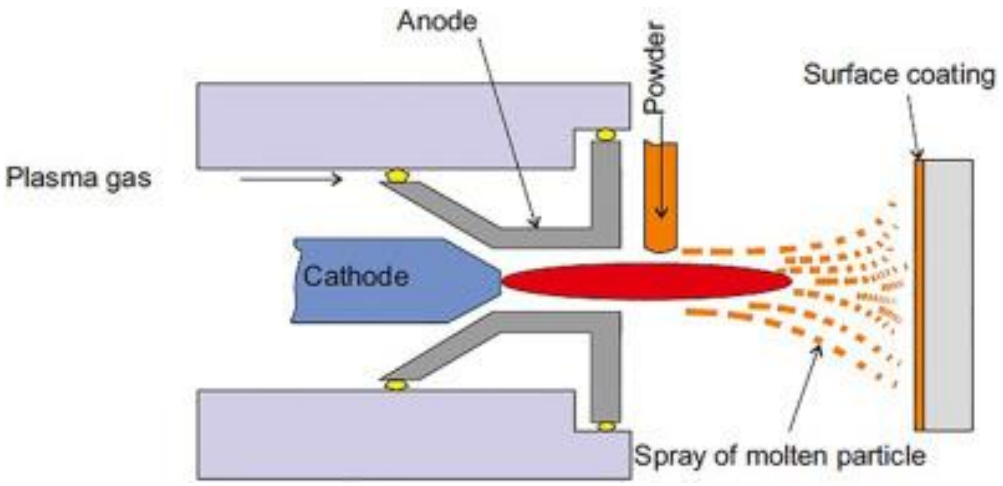

Fig. 1.2 Schematic illustration of plasma spraying process. Adapted from [28].

Residual stress built up in the thermal spraying process consists of several components [41]. Figure 1.3 [24] shows the stress evolution process during the deposition of a sprayed single splat. At first, quenching stress is developed in the splat associated with its solidification and rapid cooling. This quenching stress is in tensile because the shrinkage of sprayed particles is constrained by the substrate, and always induces vertical cracking. After the spraying, splat and substrate cool down to room temperature. During this process, compressive thermal stress is built up in the splat due to the thermal expansion

mismatch between the splat and substrate. The quenching stress and thermal stress are remained in the coating as two main components of the overall residual stress.

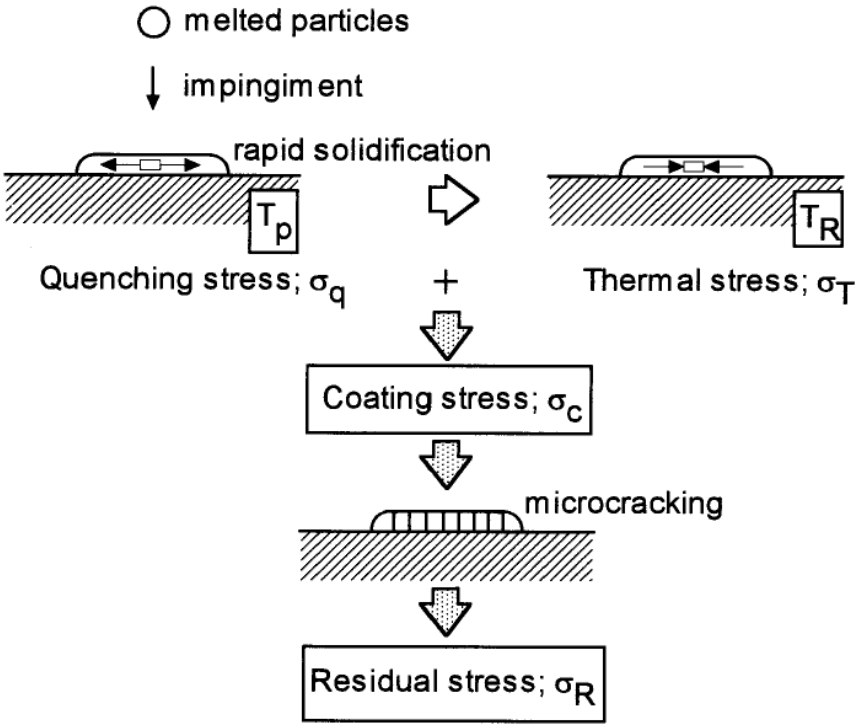

Fig. 1.3 Schematic illustration of impact, deformation, and cooling of a single splat. Adapted from [24].

Many methods have been employed to measure the residual stress in the TBCs system. Kuroda et al. [34, 35] initially captured the development of quenching stress using the Stoney equation [33] according to the measurement of substrate curvature. In the experiment, the substrate curvature was obtained from the displacement at the center of a strip-shaped substrate using a contacting displacement meter. Sampath et al. [36-38] measured the curvature of substrate using an improved method named in-situ coating property (ICP) sensor (as shown in Fig. 1.4 [36]) and successfully extracted the stress development during the actual thermal spraying process. These studies demonstrated that tensile stress during spraying process and compressive stress during cooling process are developed in the coating materials. Here, the tensile stress is attributed to the accumulation of tensile quenching stress induced by rapid shrinkage of the sprayed particles, while the compressive stress is developed due to the thermal expansion

mismatch between the substrate and coating material during the cooling process. X-ray diffraction (XRD) [39] and Digital Image Correlation (DIC) method [27] have also been applied to evaluate the stress distribution in the TBCs system. However, the residual stresses measured by these methods are the final-state values when all the spraying and cooling processes were finished. The stress evolution caused by single splat during its

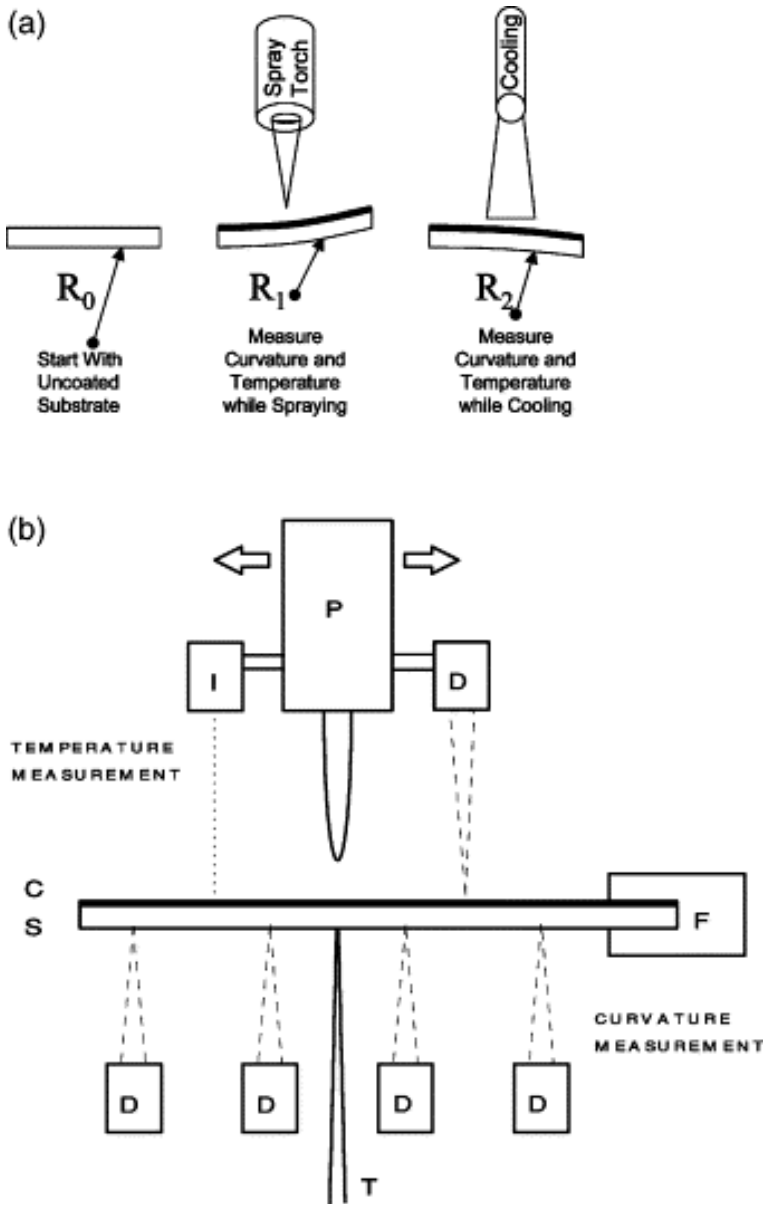

Fig. 1.4 (a) Schematic illustration of the measurement principle and (b) experimental apparatus for simultaneous measurements of deposition temperature and substrate curvature (P, plasma torch; I, infrared thermometer; T, thermocouple; D, distance sensor; F, fixture; C, coating; S, substrate). Adapted from [36].

impact, solidification and cooling process has never been directly measured due to the experimental difficulties associated with too high velocity and too small scale of splat phenomena in the actual thermal spraying.

1.3 Adhesion strength of thermal sprayed coatings

The performance of thermal sprayed coatings can be characterized by many factors, such as density and porosity, thermal conductivity, and adhesion strength. The adhesion between sprayed particles and substrates is mainly attributed to three mechanisms [42]: mechanical interlocking formed due to substrate surface irregularities, physical force from van der Waals interactions, and diffusive-chemical bond caused by diffusion and chemical reactions at the interface. According to Sobolev [43], mechanical interlocking is the major contribution to the interfacial adhesion strength between substrates and thermal sprayed coatings. Debonding, referring to the phenomenon that splats peel off from the substrate, occurs when its driving forces exceed the adhesion strength. Here, the driving forces for debonding are the shear stress along the interface and the peeling stress normal to the interface. Adhesion and debonding of splats influence the coating properties and critically affect the lifetime and performance of the coated components. Therefore, it is of great significance to evaluate and predict the adhesion strength and optimize the thermal spraying processes.

Many studies [44-48] have experimentally investigated the adhesion strength of thermal sprayed coatings, and evaluated the effects of various spraying parameters including substrate surface roughness [44], residual stress [45], heat treatment [46], and particle size [47]. Nevertheless, the reliability of coatings is critically influenced by the characteristics of single splat deposition, and is highly related to the adhesive mechanisms between splats and substrates. Compared with the extensive studies on the adhesion mechanisms of coatings, only a few publications have been reported to measure the adhesion strength of a single splat due to its extremely small size. The widely employed pull-off adhesion tests

recommended in ASTM D4541-17 [49] and ASTM C633-01 [50] are not appropriate for measuring the adhesion strength of single splats, because it is difficult to efficiently and precisely stick a splat with a loading fixture to ensure the splat can be completely detached from the substrate. Instead, an indentation experiment has been introduced by Balic et al. [51] to evaluate the adhesion strength between alumina splats and steel substrates. A strain release rate was calculated according to interfacial crack propagation to evaluate the strength and mechanisms of the adhesion between single splats and the substrates. Scratch test is another widely used technique to evaluate the adhesion strength of single splat [52-56]. For instance, Goldbaum et al. [52] measured the adhesion strength of Ti and Ti-6Al-4V splats which were sprayed onto metal substrates. Shear tests were employed in the measurements where a wedge shaped stylus was equipped to scratch the splats. The results indicated that the adhesion strength increases with the increase of substrate temperatures and impact velocities. Chen [53] evaluated the adhesion strength of plasma sprayed Fe-based splats on polished metal substrates employing a micro scratch test. The adhesion strength was found to become larger on fully pre-heated substrates due to sufficient spreading of splats and well wettability at the interface. These studies used indentation tests or scratch tests and investigated the effects of several parameters such as substrate temperatures and impact velocities. However, the effects of impact conditions on splat geometries, and the resultant measurements of scratching forces were not investigated. The relationship between the measured adhesion strength and the actual debonding behaviors of splats as well as the debonding driving forces were not fully studied.

Scraping methods have also been applied to evaluate the adhesion strength of coatings [57-59]. In this method, a cutting blade was equipped to scrape off the coatings from the substrates. Murakawa et al. [57] have proposed a scraping method based on a knife-edge scratch test to evaluate the adhesion strength of diamond coatings. Comparison of the determined adhesion strength with that measured by shearing tests suggested that the scraping method is applicable for evaluating the adhesion strength of hard coatings. Xie et al. [58] measured the adhesion strength of NiP coatings, which were chemically deposited on steel substrates, using a scraping method. The scraping energy, referring to the ratio of measured scraping forces to scraped coating areas, was proposed as a

parameter to quantify the interfacial adhesion strength. These studies indicated the scraping tests to be an effective method to evaluate the adhesion strength of sprayed coatings. However, the adhesion strength between single splat and substrate has never been studied by a scraping method yet. Effects of droplet impact parameters and residual stress in splats, which might influence the scraping test results and adhesion strength, need further research.

1.4 Drop impact test to simulate thermal spraying process

The impact of a droplet with solid substrate has been initially studied more than a century ago by Worthington [60] because of its relevance to many applications in many different fields, such as the impact of raindrop on soil and building facades [61], pesticide deposition [62], inkjet printing [63-65], and thermal spraying [66, 67]. According to the applied fields, many significant problems related to droplet impact have been studied such as the splash of droplet [68, 69], the impact pressure [70], the maximum spreading ratio [71, 72], and residual stress due to solidification and thermal shrinkage of sprayed splats [39, 73].

The impact and solidification of sprayed particles on metal substrates is also a crucial phenomenon in the APS process. Because the performance of the sprayed coating is partly dominated by the deformation of the sprayed droplets, the cooling rate of the deposited splats, and how the splats bond with each other and with the substrate [74]. These influential factors are dominated by many parameters (those are often interconnected) such as the particle size, temperature, impact velocity, roughness, and pre-heating temperature of substrate et al. as shown in Fig. 1.5 [75]. The numerous parameters make it difficult to investigate the splat behaviors in the actual thermal spraying. Therefore, over the last few decades, many researchers have carried out drop impact tests onto solid substrates to simulate the deposition process of sprayed particles during thermal spraying.

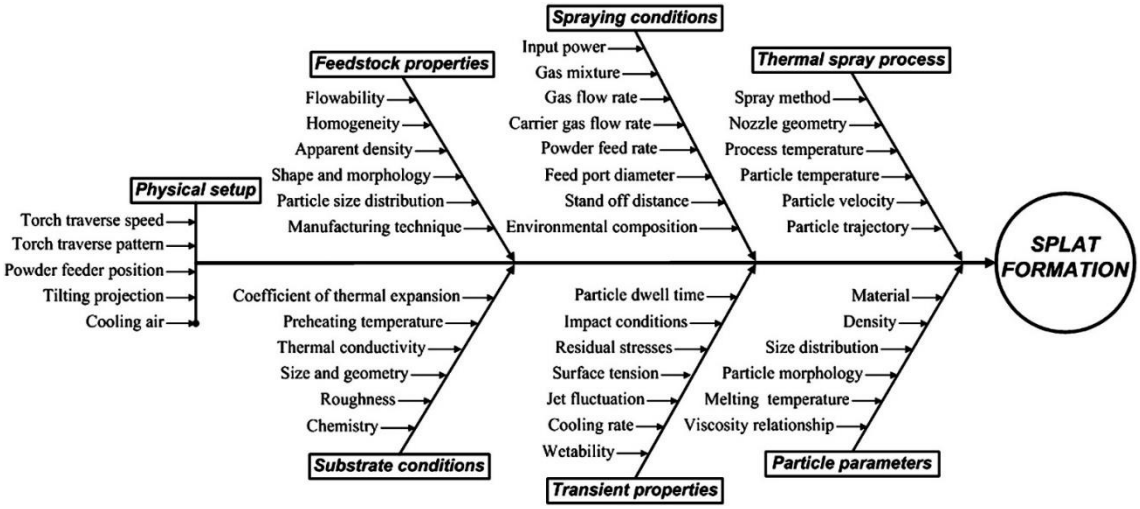

Fig. 1.5 Thermal spray coating parameters involved in splat formation. Adapted from [75]

Ghafouri-Azar et al. [76] conducted a model experiment using molten Sn particles and compared the geometry of solidified Sn splat with that of plasma-spraying Ni particle on a steel substrate. Chandra and Avedisian [77] investigated the spreading and deformation of single n-heptane droplets impacted onto substrates and evaluated the effect of substrate materials. Mostaghimi et al. [78] studied the deformation and solidification of Sn droplets impacted onto a flat stainless plate experimentally and numerically. The schematic diagram of an experimental apparatus developed by their research group is shown in Fig. 1.6 [78]. In the experiments, the impact of droplets was photographed, and the droplet spreading diameter and liquid-solid contact angle are measured from the photographs. In the simulation, the measured liquid-solid contact angle was used as a boundary condition, and the measured substrate temperature evolution was used to estimate droplet/substrate heat transfer coefficient. Deformation of the droplet was accurately modeled during its impact and solidification process by applying a modified SOLA-VOF method. They also investigated the effect of spraying angle on the formation of thermal spraying splats by using a numerical method in which the solidification and splashing of particle were not considered [79]. The results indicated that the elongation factor of splat increased when spray angle decreased, while the splat area varies little with spray angle. Bhola and Chandra [80] conducted a model experiment using a paraffin wax droplet. In this study, the paraffin droplet was dropped and deposited onto an aluminum substrate to investigate

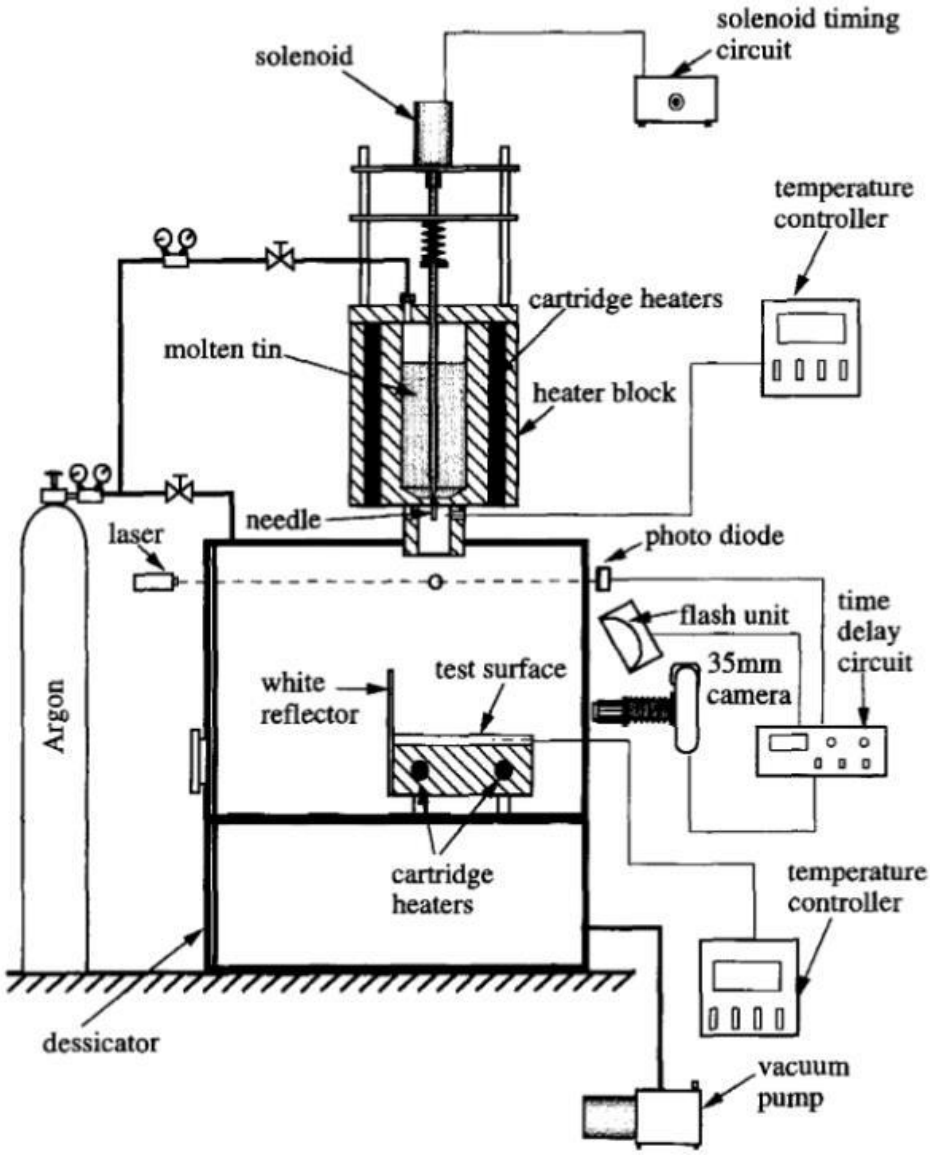

Fig. 1.6 Schematic illustration of impact testing apparatus for molten Sn drop test. Adapted from [78].

the effects of impact velocity and surface temperature on splat diameter and liquid-solid contact angle. They observed that the liquid droplet recoiled in the center of droplet when impacting a cold surface, and revealed that this recoiling phenomenon is influenced by the substrate temperature and impact velocity. Dadvar and Chandra [81] carried out droplet impact tests using paraffin waxes and evaluated the effects of substrate temperature and impact velocity on the deformation and morphology of splats. In their study, the adhesion strength between splat and polymer substrate was measured through

a simple pull test considering several impact parameters. These studies investigated the deformation, heat transfer, and adhesion strength experimentally or numerically with respect to test conditions. However, the stress-strain development during the solidification and cooling process of splat has not been detected. In addition, the mechanisms of fracture phenomenon in a single splat need further research.

1.5 Object and outline of the dissertation

The primary object of this dissertation is to quantify the stress-strain evolution, and clarify the cracking and debonding behaviors of a droplet impacted and solidified on metal substrate considering various drop impact conditions. In this dissertation, a model experiment using paraffin wax is carried out to investigate the thermal spraying process easily and simply. Molten paraffin wax droplet is dropped and impacted onto a 430 stainless steel substrate. Strain evolution at the substrate back surface is measured by a strain gauge to study the effects of substrate pre-set temperature, drop height, droplet temperature, and paraffin wax materials. During the experiment, vertical cracking in splats, debonding at the splat/substrate interface are observed under certain specific drop impact conditions. Towards an in-depth understanding of the effects of impact conditions on debonding behaviors of splats, a scraping method is employed to measure the adhesion strength of splats formed under various impact conditions. The effect of residual stress on the adhesion strength is also investigated.

Driving forces for these fracture behaviors are investigated by elastic FEM according to experimentally measured residual strains considering material properties and geometries of the splats and substrate. Coupled thermo-mechanical analysis is performed to calculate the evolution of the residual strain and substrate temperature during drop experiment. A strain hardening creep model was implemented into the FE model to quantify the creep deformation of the splat. Based on the numerical results, the effect of splat/substrate adhesion on the stress-strain relaxation is discussed with respect to several experimental

variables.

A brief skeletal structure of the dissertation is detailed as below:

- Chapter 2 presents measurements of thermal and mechanical properties of paraffin wax materials.
- Chapter 3 shows measurements of residual strains and observations of fracture phenomena during drop experiments.
- Chapter 4 focuses on the evaluation of adhesion strength between splat/substrate using a scraping method.
- Chapter 5 aims to investigate the stress distribution of splat/substrate structure using an elastic finite element simulation to clarify the criteria of cracking and debonding of splats.
- Chapter 6 concentrates on the calculation of residual strain evolution during drop experiments by using a coupled thermo-mechanical analysis. The effects of creep and interfacial adhesion on residual strain are investigated by comparing the experimental and numerical results.
- Chapter 7 concludes this dissertation and highlights the significant results and possible applications.

Chapter 2

Material properties of paraffin waxes

Thermal spraying process was simplified by conducting a model experiment, in which paraffin wax droplets were impacted and solidified on metal substrate. Two types of paraffin wax materials were employed in the experiments. They are an industrial paraffin wax HNP-9 (Nippon Seiro) and a normal candle wax (Kameyama). Their thermal properties, including melting point, specific heat, latent heat, thermal conductivity coefficient, thermal expansion coefficient, and mechanical properties, including temperature dependent Young's modulus and ultimate tensile strength, temperature dependent creep property are measured and discussed in this chapter.

2.1 Thermal properties

2.1.1 DSC measurements

A heat-flux differential scanning calorimeter (DSC-60, Shimadzu) was employed to measure the melting point, specific heat, and latent heat of paraffin waxes [82]. Measured results are presented in Fig. 2.1 for candle wax and HNP-9 changing the testing temperature from 0 °C to 140 °C. According to the figure, melting point of HNP-9 is about 20 °C higher than candle wax. Here, the melting point was termed as the specific temperature when the measured specific heat reaches the maximum value. The specific heats for two paraffin wax materials are very close under all temperatures except for phase change. It can be speculated from the measurements that HNP-9 is a comparatively pure paraffin wax compared with candle wax, which seems to contain several various components. Melting points, latent heat, liquidus and solidus temperatures, and specific heat at 100 °C were determined from the figure and summarized in Table 2.1 along with

other thermal properties which are determined in Sec. 2.1.2 and 2.1.3.

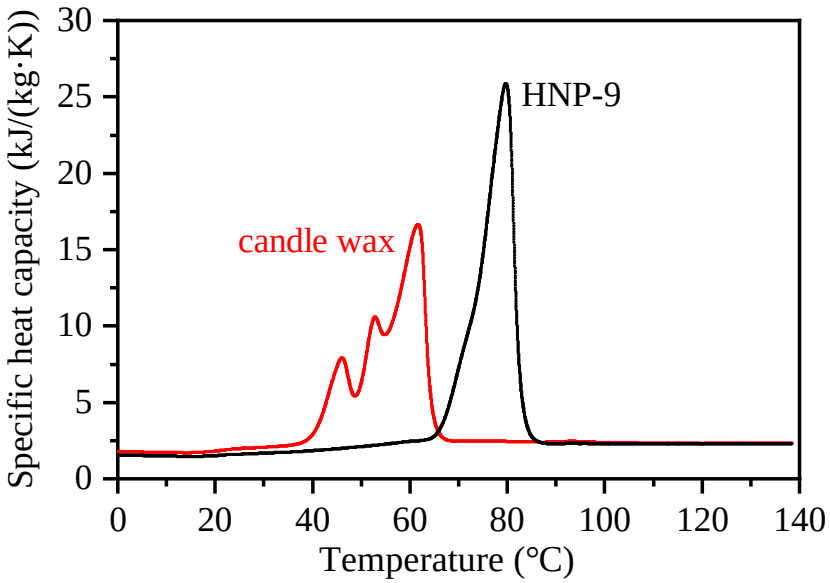

Fig. 2.1 DSC measurements of specific heat of candle wax and HNP-9 as a function of testing temperature.

Table 2.1 Thermal properties of candle wax and HNP-9.

Paraffin wax material	candle wax	HNP-9
Melting point, T_m (°C)	61.7	79.8
Latent heat of solidification, L_s (kJ/kg)	160	190
Solidus temperature, T_s (°C)	50	65
Liquidus temperature, T_l (°C)	70	90
Specific heat at 100°C, C_p (kJ/(kg·K))	2.4	2.3
Thermal conductivity at 25°C, λ_p (W/(m·K))	0.27	0.26
Thermal expansion coefficient, α_p	230×10^{-6}	176×10^{-6}

2.1.2 Thermal conductivity

The flash method [83] is widely employed to measure the thermal diffusivities of solid specimens. In this dissertation, thermal diffusivities of two types of paraffin wax materials were measured referring to the flash method. The thermal conductivity was then calculated by multiplying the measurements of thermal diffusivity, specific heat, and density. During the measurement, one side of the specimen, with 80 mm in length, 80 mm in width, and 3.0 mm in thickness, was heated by a halogen lamp (CTW-500). The resultant temperature change on the other side of the specimen was measured with an infrared camera (PI-450, Optris). The specimen surface was pre-sprayed with matt black paint to avoid reflection. All tests were conducted at room temperature. Measured results are listed in Table 2.1.

2.1.3 Thermal expansion coefficient

Thermal expansion coefficient was measured by a Thermomechanical Analyzer (TMA-8311, Rigaku). During the measurement, the temperature of paraffin wax specimens with 10 mm in length, 5 mm in width, and 6.25 mm in thickness was increased from ambient temperature (approximate 25 ºC) to their melting points with a velocity of 1 ºC/min. The temperature of paraffin specimen and elongation in the length direction was recorded during the heating process as shown in Fig. 2.2 for (a) HNP-9 and (b) candle wax. Thermal expansion coefficients can be calculated through:

$$\alpha_p = \frac{1}{l}\frac{\Delta l}{\Delta T}, \tag{2.1}$$

where l, Δl, and ΔT refer to the length (= 10 mm), elongation, and temperature rising of the specimen, respectively. The calculated thermal expansion coefficients for two types of paraffin wax materials are listed in Table 2.1. It can be seen that candle wax has a larger thermal expansion coefficient than HNP-9.

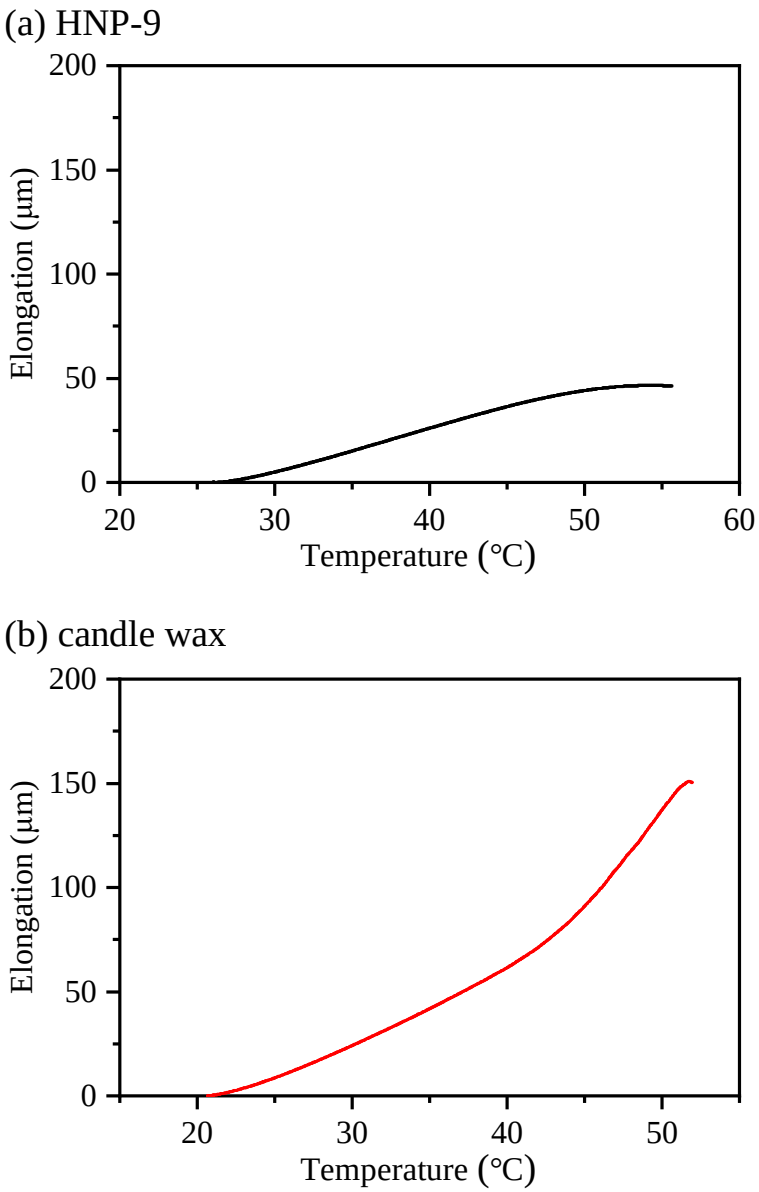

Fig. 2.2 Elongation of the specimen measured by a Thermomechanical Analyzer as a function of testing temperature for (a) HNP-9 and (b) candle wax.

2.2 Young's modulus and ultimate tensile strength

Young's modulus and ultimate tensile strength of paraffin wax materials were measured by using a four-point bending method basically based on the ASTM D6272-17 standard test method for bending properties of plastics and electrical insulating materials [84]. Measurement was carried out using a universal testing instrument (Autograph AGS-H, Shimadzu). The schematic illustration of four point bending test is presented in Fig. 2.3.

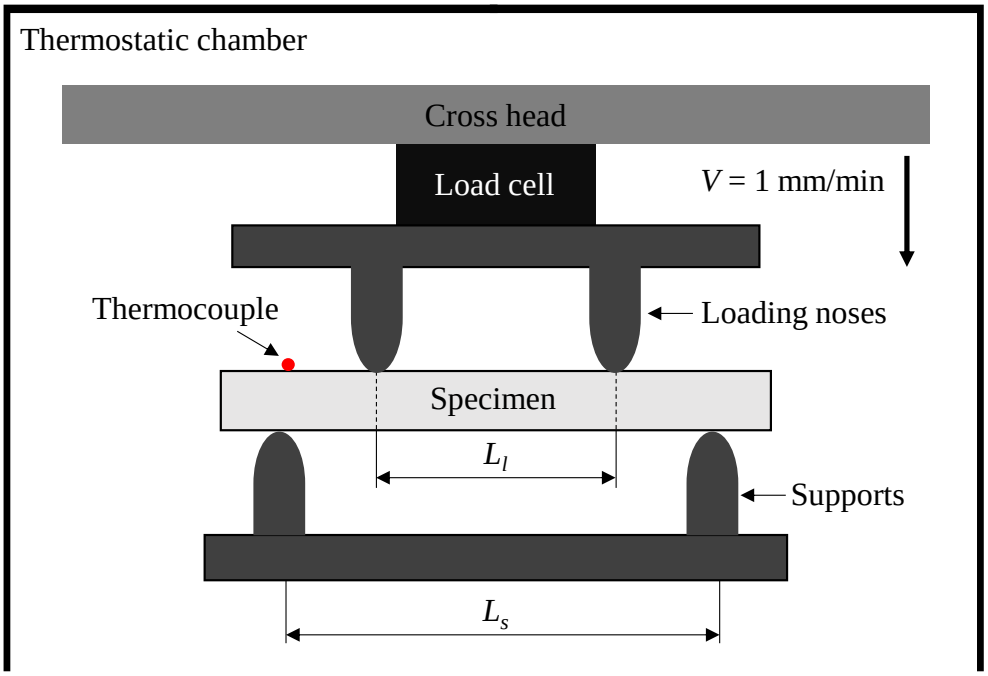

Fig. 2.3 Schematic illustration of four-point bending test.

The distance between the loading noses (the load span) is one half of the support span (see Fig. 2.3):

$$L_l = \frac{1}{2} L_s . \tag{2.2}$$

Two different methods are employed to make paraffin wax specimens (80.0 mm in length,

12.5 mm in breadth, and 6.25 mm in height) for the bending test. For candle wax, a plastic mold was designed because of the low bond strength between solidified paraffin and plastic. The test specimen was made by pouring the molten paraffin inside the mold that is pre-heated to approximate 50 ºC until it was full. The mold was then moved to a thermostatic chamber with a temperature of 50 ºC (a little lower than the melting temperature of paraffin wax materials) until the specimen had completely solidified otherwise holes might be produced inside the specimen due to shrinkage during phase transfer and cooling of paraffin. The specimens of HNP-9 were made by cutting out from a large paraffin block. Considering the temperature dependence of tensile strength and Young's modulus of paraffin waxes, the tests were carried out under testing temperatures from 0 ºC to nearly melting points with an interval of 5 ºC or 10 ºC. The specimen temperature was controlled by a thermostatic chamber (TCE-N300, Shimadzu). To minimize random errors, three specimens were prepared for each testing temperature.

During the test, specimen was bent at a rate of 1 mm/min until it broke. Temperature of the specimen was measured by a K-type thermocouple put on the surface of the specimen as shown in Fig. 2.3, and controlled within an error range of ± 1 ºC. An example of measured displacement-force curve is shown in Fig. 2.4 for HNP-9 at testing temperature of 20 ºC. By obtaining the slope and maximum loading force derived from Fig. 2.4,

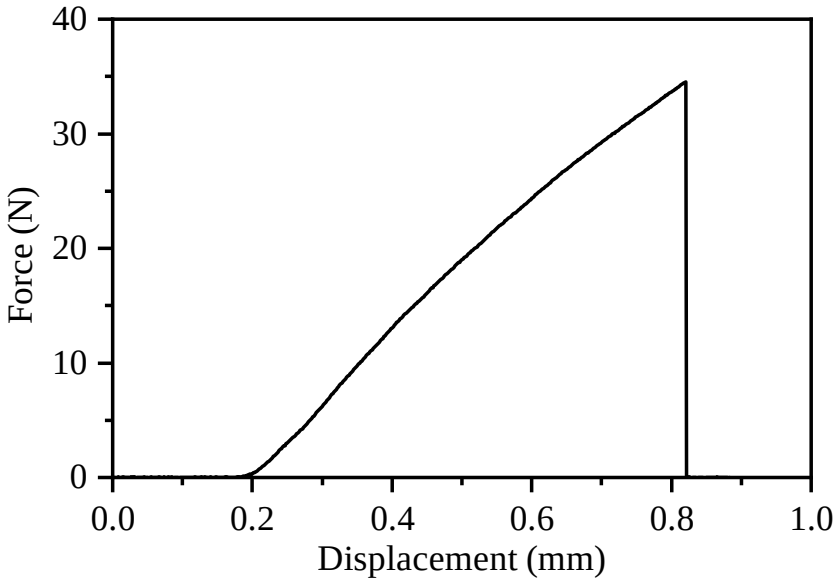

Fig. 2.4 Measured displacement-force curve of HNP-9 at 20 °C.

Young's modulus and tensile strength of paraffin wax materials can be obtained based on the following calculations.

1) The displacement of the loading noses y_l (equals to the displacement of the crosshead) can be given in:

$$y_l = \frac{11}{64}\frac{FL_s^{\,3}}{Ebt^3}, \tag{2.3}$$

where, F, E, b and t refer to the force measured by the load cell, Young's modulus of the specimen, breadth and thickness of the specimen, respectively.

2) The slope of the displacement-force curve, s can be written as:

$$s = \frac{\Delta F}{\Delta y_l}, \tag{2.4}$$

In the actual calculation, s was estimated from the measured curve.

3) Therefore, Young's modulus of paraffin wax can be given in:

$$E = \frac{11}{64}\frac{sL_s^{\,3}}{bt^3}. \tag{2.5}$$

4) The force acting on the specimen when it breaks is termed as the maximum force, $F_{\max}$. The maximum tensile stress in the specimen is located at the middle of the specimen's lower surface, with a coordinate of $y = \frac{t}{2}$, $z = 0$. This maximum stress equaling to the tensile strength can be given in:

$$\sigma_{\max} = \frac{3F_{\max}L_s}{4bt^2}. \tag{2.6}$$

Averaged values of three tests (only 1 or 2 tests were carried out near their melting points) are plotted in Fig. 2.5 for Young's modulus and in Fig. 2.6 for tensile strength. Both values decrease with the increase of the testing temperature and reduce to zero near their melting points. From the figures, candle wax generally has a smaller Young's modulus than HNP-9. While the tensile strength of candle wax is higher when the temperature is below 40 ºC.

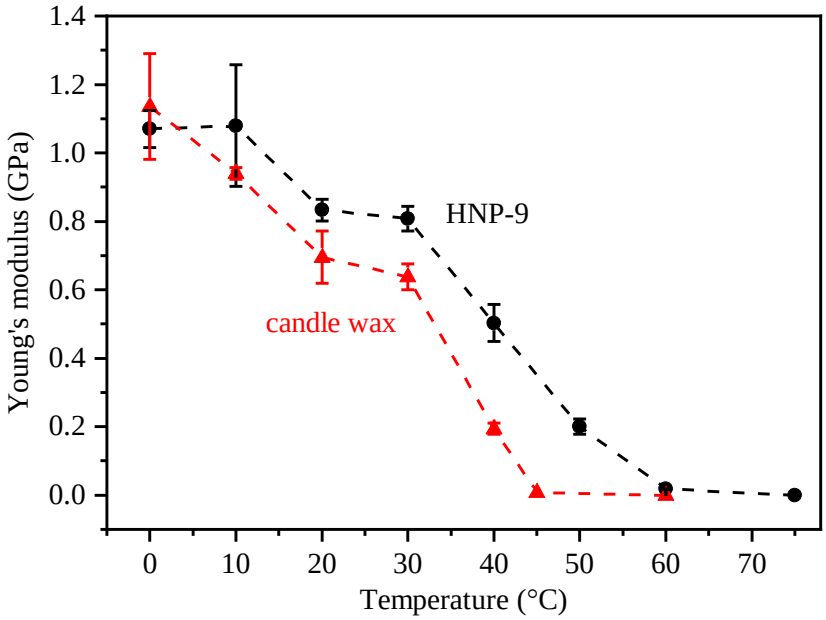

Fig. 2.5 Young's modulus of HNP-9 and candle wax as a function of testing temperature measured by four-point bending test.

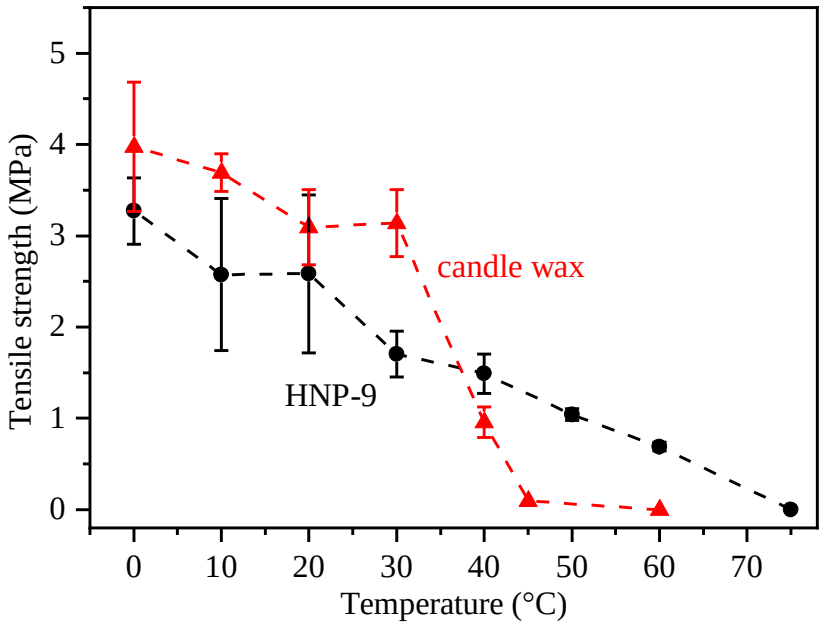

Fig. 2.6 Tensile strength of HNP-9 and candle wax as a function of testing temperature measured by four-point bending test.

2.3 Creep properties

2.3.1 Four point bending creep test

Creep properties of paraffin wax materials were measured for evaluating the creep deformation during the adhesion and cooling process of solidified splat. Due to the low toughness and slippery surfaces of paraffin, a tensile creep test is hard to conduct. Therefore, a four-point bending method was applied in this chapter. The experimental setup is schematically illustrated in Fig. 2.7, which is developed from Fig. 2.3. The load is applied by the jig and the weight, and kept constant during the test. Tests were conducted with five (in some cases only three or four) different loads under constant temperature, which was controlled by a thermostatic chamber (TCE-N300, Shimadzu). Displacement field of specimen's side surface was measured with a digital image correlation (DIC) method. The specimen was prepared in the same manner with Sec. 2.2. Candle wax was specifically tested at the temperature conditions of 10°C, 20°C, 30°C,

40°C, 45°C, and tests for HNP-9 were conducted at 20°C, 30°C, 40°C, 50°C, and 60°C.

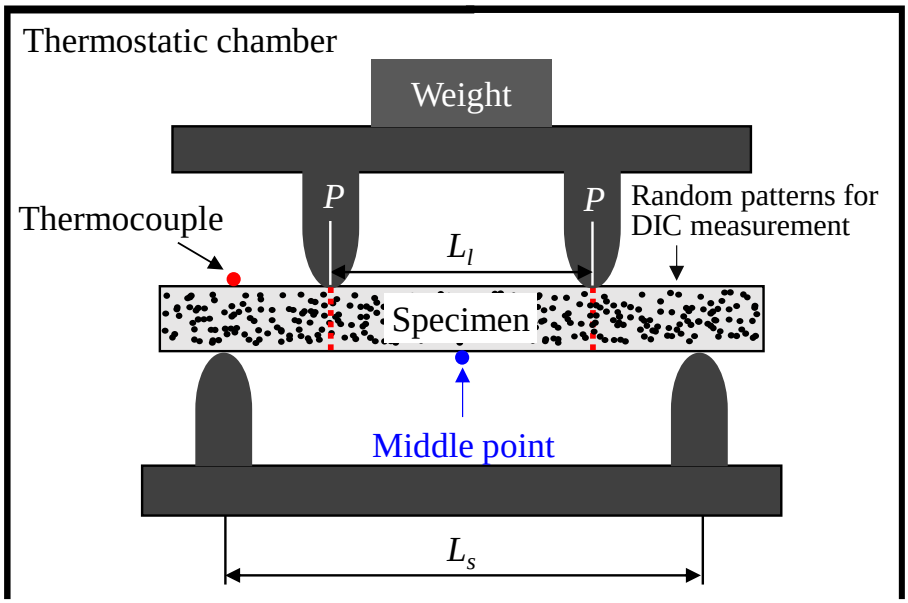

Fig. 2.7 Schematic illustration of the experimental setup for a four point bending creep test.

Typical time-displacement curves during the creep test at 20 °C are shown in Fig. 2.8 for (a) HNP-9 and (b) candle wax. The horizontal axis corresponds to the test time with a period of 5400 s. During the creep test, the displacement was detected with an interval of 1 minute in the first 10 minutes, a 5-minute interval from the 10 to 30 minutes, and a 10-minute interval in the last 60 minutes. The vertical axis shows the creep displacement of the load points measured by DIC. Here, the displacement is determined by the average displacement along the two red dashed lines just below the loading points as shown in Fig. 2.7. Experimental results exhibit similar tendency for each loading condition, namely, the displacement and displacement rate increase with the load. The displacement rate gradually reduces during the first 10 minutes, during which a transition creep is observed. This transition creep is followed by an almost straight curve, which is very likely to be a secondary creep. It is worth noting that the creep deformation in paraffin wax exhibits a high similarity with those in metallic materials.

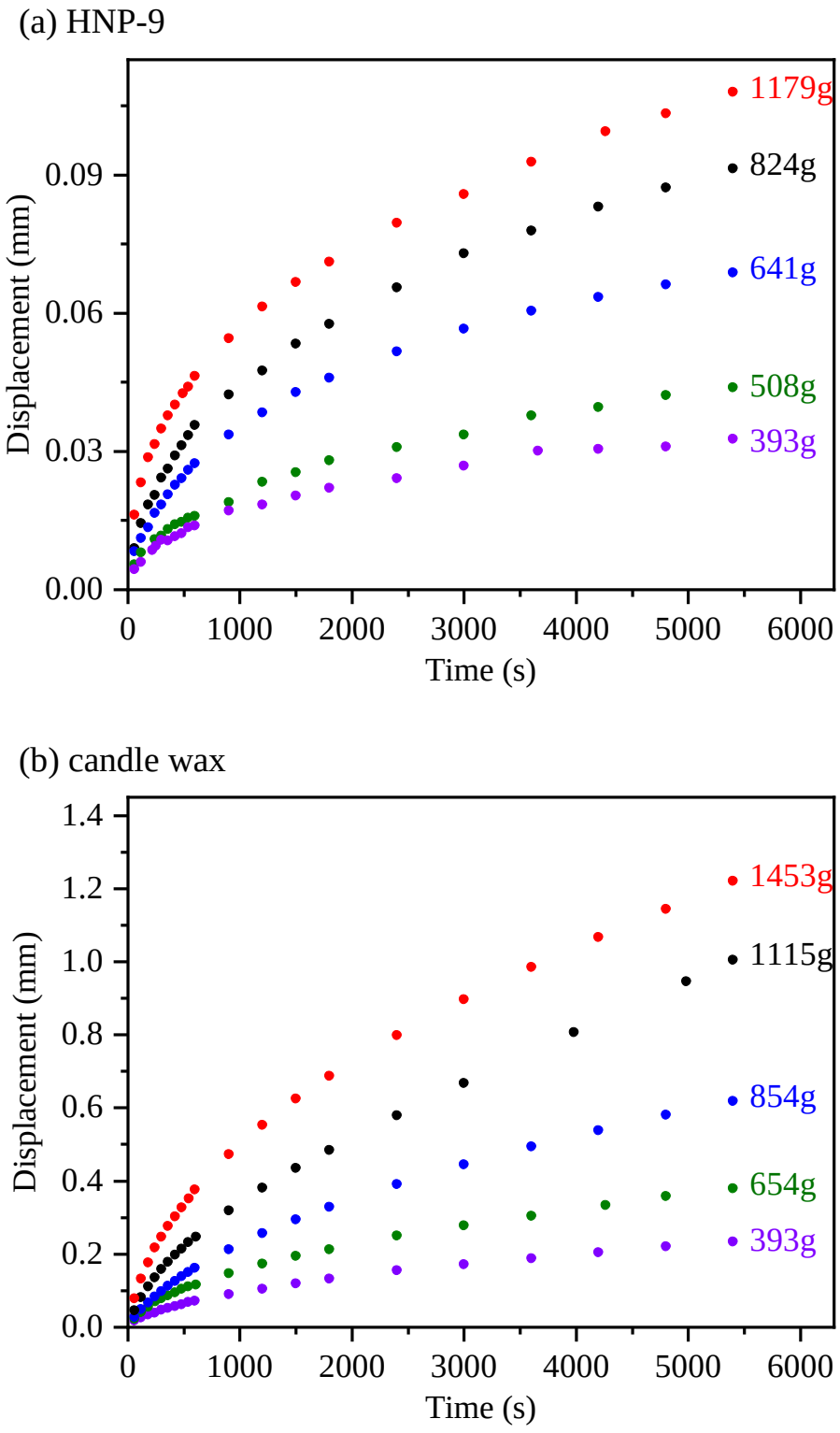

Fig. 2.8 Time-displacement curves for (a) HNP-9 and (b) candle wax at a testing temperature of 20 °C under five different load conditions.

2.3.2 Constitutive equations of power law creep model

The power law creep model has been widely used to describe the transition creep because of its simplicity and versatility [85, 86]:

$$\varepsilon = \frac{A}{m+1}\sigma^n t^{m+1}, \tag{2.7}$$

where ε is creep strain; σ is stress; t is creep time; A, m, and n are temperature dependent constants. Differentiating Eq. 2.7 with respect to time t:

$$\dot{\varepsilon} = A\sigma^n t^m, \tag{2.8}$$

is obtained. On the other hand, extracting (m+1)th root of Eq. 2.7, solving it for time t, and then substituting it into Eq. 2.8,

$$\dot{\varepsilon} = (m+1)\left(\frac{A}{m+1}\sigma^n\right)^{1/(1+m)} \varepsilon^{m/(1+m)}, \tag{2.9}$$

can be obtained. Eq. 2.8 and Eq. 2.9 are so-called time hardening and strain hardening forms of power law creep model, respectively. The time hardening form is appropriate when the stress state keeps constant. On the other hand, the strain hardening form is more appropriate when the stress state changes with time [87].

To obtain the values of A, m, and n from the experimental data of four point bending creep tests, the maximum tensile stress and strain along the horizontal direction at the center of the support points (blue point in Fig. 2.7) are calculated according to the following equations [88]:

$$\sigma_{\max} = \frac{3P(L_s - L_l)}{bt^2}, \tag{2.10}$$

$$\varepsilon_{\max} = \frac{6t}{(L_s - L_l)(L_s + 2L_l)} y_l, \tag{2.11}$$

where P is the applied load, b, t, L_l, L_s, and y_l have the same meaning with those in Sec. 2.2. Here, the stress ($\sigma_{\max}$) and strain ($\varepsilon_{\max}$) are instantaneous magnitudes at the beginning of the tests, and they change slightly during the bending creep test due to the creep deformation. In this study, this change is ignored. Typical time-strain curves are plotted in Fig. 2.9 for (a) HNP-9 and (b) candle wax according to the experimental data shown in Fig. 2.8. It is clearly shown in both Fig. 2.9(a) and (b) that the strain increases with the applied stress.

The creep constants A, m, and n were determined by curve fitting using Eq. 2.7. Five sets of creep constants were obtained for each temperature by using the experimental data of (a) 0-3 min, (b) 0-5 min, (c) 0-10 min, (d) 0-20 min, and (e) 0-90 min. Curve fitting was conducted using the Levenberg-Marquardt nonlinear least squares algorithm in MATLAB (The MathWorks, Inc) without imposing restrictions on the constants. Curve fitting results for all test conditions are summarized in Table 2.2 for HNP-9 and Table 2.3 for candle wax. Figure 2.10 and Fig. 2.11 show the comparison of time-strain curves generated by the model fit and the experimental results when the testing temperature was 20 °C, paraffin wax materials were HNP-9 and candle wax, respectively. In these figures, creep properties of paraffin wax materials are properly described by the hardening form of creep law (Eqs. 2.7-2.9) and the stress-strain estimation (Eqs. 2.10, 2.11).

The experimental data has also been evaluated considering a simple secondary creep law; that is Norton law. However, it failed to describe the rapid stress relaxation at the beginning of the bending creep test, and therefore will not be applied to evaluate the creep deformation of paraffin wax in this dissertation.

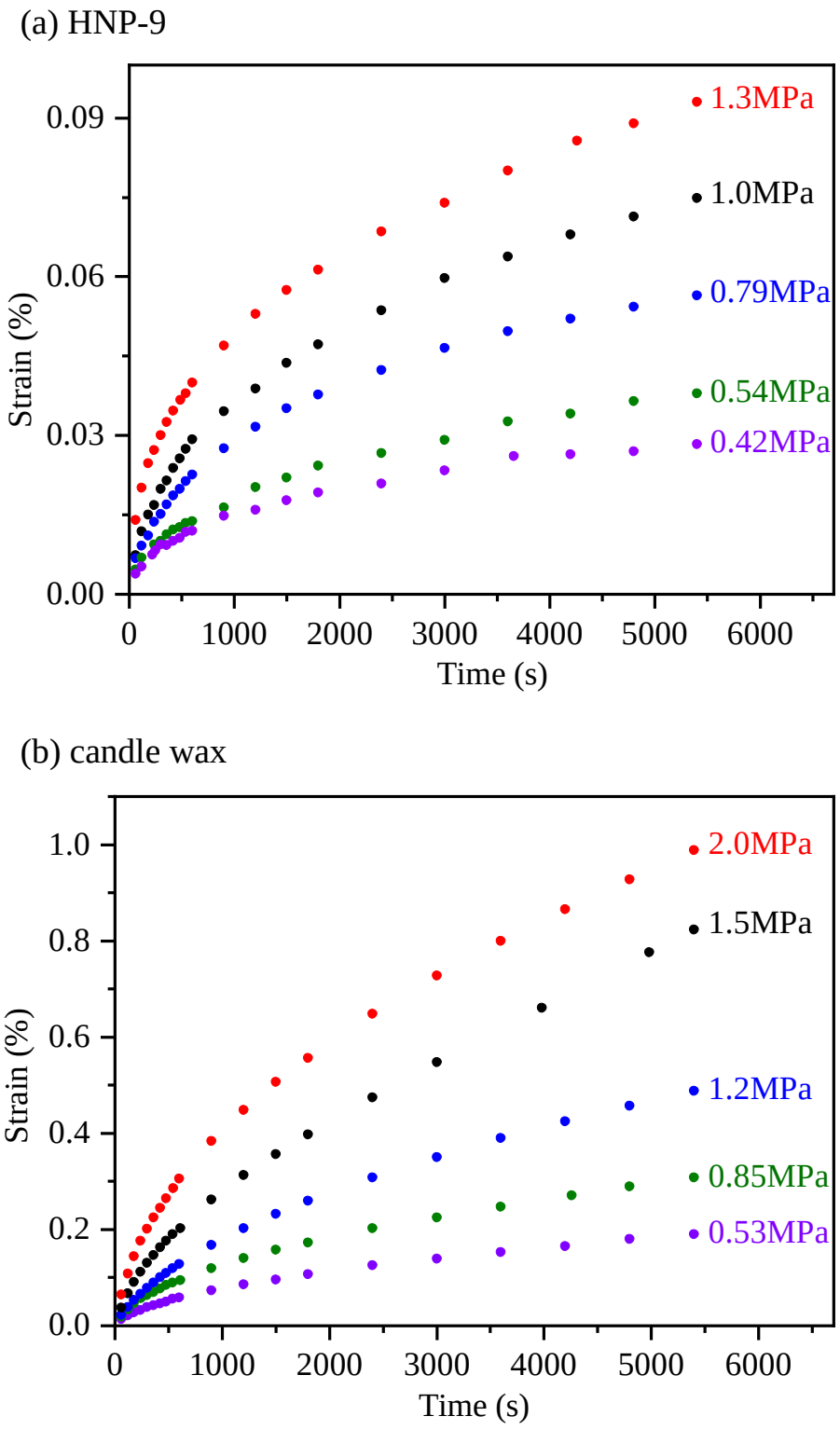

Fig. 2.9 Time-strain curves of (a) HNP-9 and (b) candle wax at a testing temperature of 20 °C under five different stress conditions.

Table 2.2 Data fitting results of creep constants for strain-hardening form of power-law creep model and *R* squared values for paraffin materials of HNP-9. Five sets of constants with various time spans were obtained for each testing temperature.

Paraffin wax	HNP-9				
Temperature (°C)	Time span (min)	A ($Pa^{-n}s^{-m-1}$)	n	m	R^2
20	0-3	8.22×10^{-14}	1.30	-0.452	0.964
	0-5	2.22×10^{-13}	1.24	-0.494	0.972
	0-10	5.91×10^{-13}	1.17	-0.515	0.989
	0-20	1.11×10^{-12}	1.13	-0.536	0.991
	0-90	4.44×10^{-12}	1.04	-0.578	0.995
30	0-3	5.10×10^{-13}	1.21	-0.387	0.986
	0-5	3.41×10^{-13}	1.24	-0.385	0.994
	0-10	2.47×10^{-12}	1.09	-0.396	0.994
	0-20	1.66×10^{-12}	1.13	-0.428	0.996
	0-90	5.51×10^{-12}	1.05	-0.447	0.987
40	0-3	6.73×10^{-10}	0.729	-0.248	0.952
	0-5	4.43×10^{-10}	0.766	-0.269	0.970
	0-10	3.81×10^{-10}	0.790	-0.317	0.970
	0-20	3.07×10^{-10}	0.817	-0.351	0.970
	0-90	1.21×10^{-9}	0.731	-0.395	0.959
50	0-3	5.00×10^{-15}	1.79	-0.346	0.931
	0-5	8.68×10^{-15}	1.75	-0.338	0.933
	0-10	7.85×10^{-15}	1.77	-0.387	0.941
	0-20	2.24×10^{-14}	1.70	-0.420	0.943
	0-90	2.57×10^{-14}	1.69	-0.409	0.942
60	0-3	2.62×10^{-8}	0.661	-0.251	0.962
	0-5	1.88×10^{-8}	0.667	-0.179	0.974
	0-10	1.79×10^{-8}	0.692	-0.240	0.976
	0-20	1.59×10^{-8}	0.709	-0.260	0.979
	0-90	1.23×10^{-8}	0.767	-0.354	0.985

Table 2.3 Data fitting results of creep constants for strain-hardening form of power-law creep model and R squared values for paraffin materials of candle wax. Five sets of constants with various time span were obtained for each testing temperature.

Paraffin wax	candle wax				
Temperature (°C)	Time span (min)	A ($Pa^{-n}\cdot s^{-m-1}$)	n	m	R^2
10	0-3	2.00×10^{-13}	1.05	-0.343	0.958
	0-5	4.79×10^{-13}	0.989	-0.348	0.979
	0-10	6.54×10^{-13}	0.977	-0.384	0.991
	0-20	7.08×10^{-13}	0.990	-0.449	0.989
	0-90	3.51×10^{-13}	1.07	-0.545	0.982
20	0-3	8.29×10^{-15}	1.49	-0.243	0.967
	0-5	1.34×10^{-14}	1.47	-0.282	0.974
	0-10	3.55×10^{-14}	1.42	-0.343	0.982
	0-20	3.64×10^{-14}	1.43	-0.377	0.987
	0-90	1.36×10^{-13}	1.35	-0.413	0.985
30	0-3	7.26×10^{-15}	1.68	-0.320	0.916
	0-5	5.74×10^{-15}	1.72	-0.396	0.930
	0-10	1.94×10^{-14}	1.64	-0.450	0.942
	0-20	1.78×10^{-14}	1.66	-0.484	0.951
	0-90	4.28×10^{-14}	1.59	-0.467	0.977
40	0-3	3.96×10^{-15}	2.03	-0.294	0.959
	0-5	8.64×10^{-15}	2.01	-0.432	0.973
	0-10	1.67×10^{-14}	1.95	-0.448	0.989
	0-20	2.40×10^{-14}	1.92	-0.421	0.993
	0-90	1.00×10^{-12}	1.59	-0.403	0.996
45	0-3	9.67×10^{-12}	1.39	-0.275	0.979
	0-5	3.33×10^{-11}	1.29	-0.305	0.989
	0-10	1.50×10^{-10}	1.16	-0.310	0.985
	0-20	-			
	0-90				

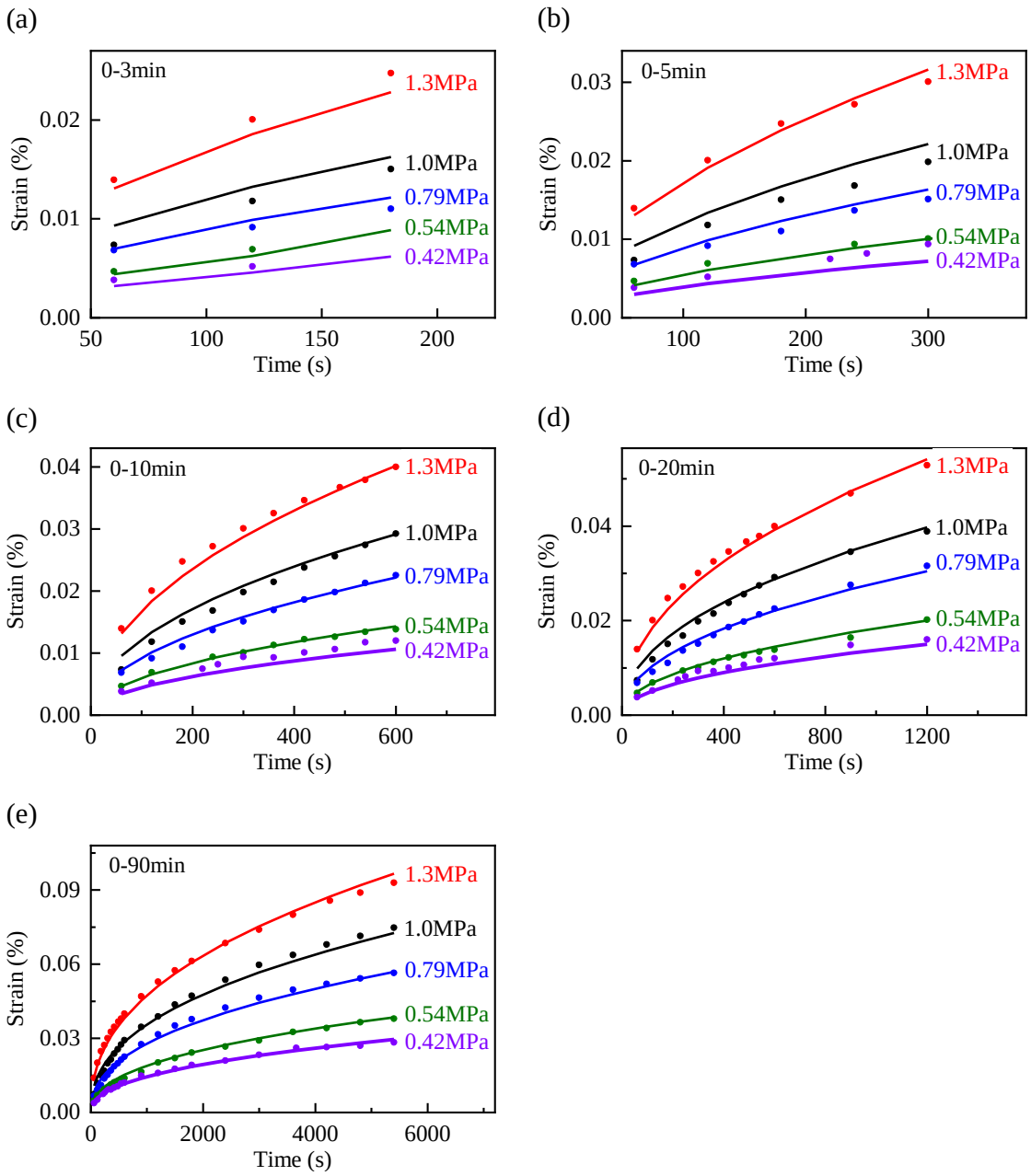

Fig. 2.10 Comparison between the measurements and data fitting results of time-strain curves for paraffin material of HNP-9, testing temperature of 20 °C. (a)~(e) show the results when data fitting was performed by using the test date of (a) 0-3min, (b) 0-5min, (c) 0-10min, (d) 0-20min, and (e) 0-90min, respectively.

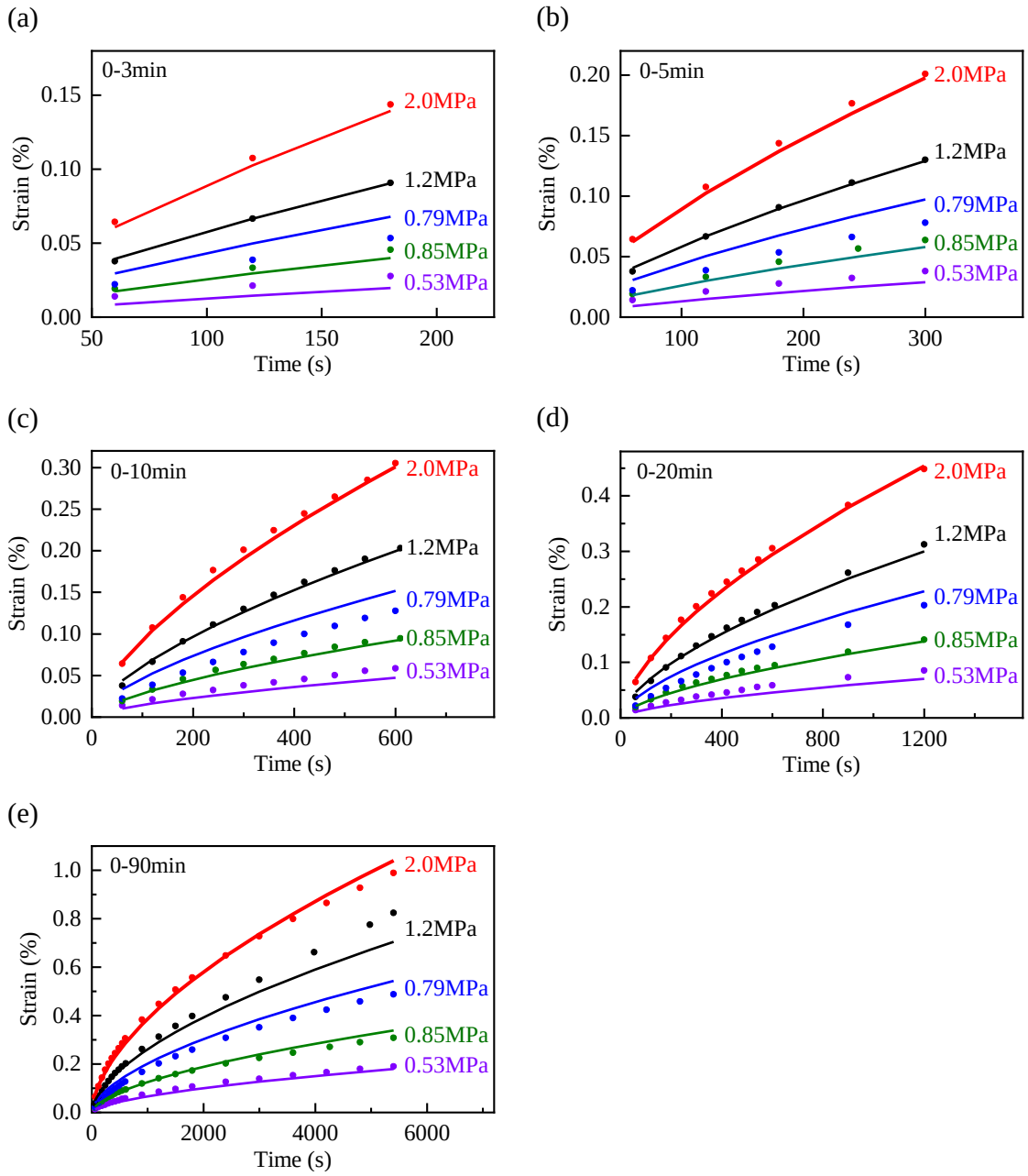

Fig. 2.11. Comparison between the measurements and data fitting results of time-strain curves for paraffin material of candle wax, testing temperature of 20 °C. (a)~(e) show the results when data fitting was performed by using the test date of (a) 0-3min, (b) 0-5min, (c) 0-10min, (d) 0-20min, and (e) 0-90min, respectively.

2.4 Summary

This chapter mainly focuses on the measurements of material properties of paraffin waxes. The measured results will be employed to interpret experimental results and perform numerical simulations in the following chapters. Young's modulus and thermal expansion coefficient will be mainly used to carry out elastic FE analysis for calculating stress distributions in Chapter 5. Other properties including temperature dependent creep will be employed to carry out coupled thermo-mechanical FE analysis for calculating strain evolutions and investigating creep deformation and interfacial adhesion in Chapter 6.

Chapter 3

Drop experiment

The drop experiment was conducted to investigate the effects of impact conditions on the stress evolution and fracture behaviors of single splats. This model experiment partly simulates the thermal spraying, in which molten droplets are impacted, spread, and solidified on the metallic substrate. Growth of oxide or formation of gas layer at the splat/substrate interface are not investigated and rather removed to focus on the stress-strain evolution and fracture behaviors during the solidification and adhesion process of molten droplets.

3.1 Experimental setup

The experimental setup for drop experiments, which was improved from the previous setup [89] is schematically illustrated in Fig. 3.1. Paraffin wax was melted in an aluminum holder which was wrapped by a heater. A needle with an inner diameter of 3.0 mm was inserted in the bottom of the holder so that droplets could be generated and controlled by turning the micrometer head (MHH2-50, Mitutoyo). The droplet was detached from the holder when its weight exceeded the surface tension force. The temperature of droplets was measured and controlled by a thermocouple (Type K, 0.32-mm wire diameter) attached to the bottom of the holder. An HNP-9 droplet and a candle wax droplet had a mass of 18.6 ± 0.6 mg and 17.9 ± 0.7 mg, respectively when the droplet temperature was set to 140 °C. During the drop experiment, the droplet was impacted onto a 430 stainless steel disc substrate with a roughness of Rq = 38 nm, a diameter of 95 mm, and thickness of 0.5 mm. A bi-axial strain gauge (KFG-1-120-D16-11 L3M3S, KYOWA) was attached to the back surface of the substrate to measure the strain evolution due to the droplet. To measure the evolution and distribution of the temperature in the substrate, four K-type

thermocouples were attached to the substrate back surface. Distances from the center of the substrate were 2.6 mm, 15 mm, 30 mm, and 39.7 mm, respectively. The four measured temperatures were identified as T_1, T_2, T_3, and T_4, as shown in Fig. 3.1. The substrate temperature was controlled by a thermostatic chamber with a vacuum thermal insulation jacket (BT-100, Sugiyama-Gen). The above-mentioned T_1 was viewed as the substrate temperature. The evolutions of strain and temperature were measured and recorded by a data logger (Memory HiLogger LR8431, Hioki) with a time interval of 0.01 s. The impact movies were recorded by a digital camera (D3300, Nikon) to observe the cracking and debonding behaviors of solidified splats. This experimental apparatus can easily adjust substrate pre-set temperature, drop height, droplet temperature, and paraffin wax materials.

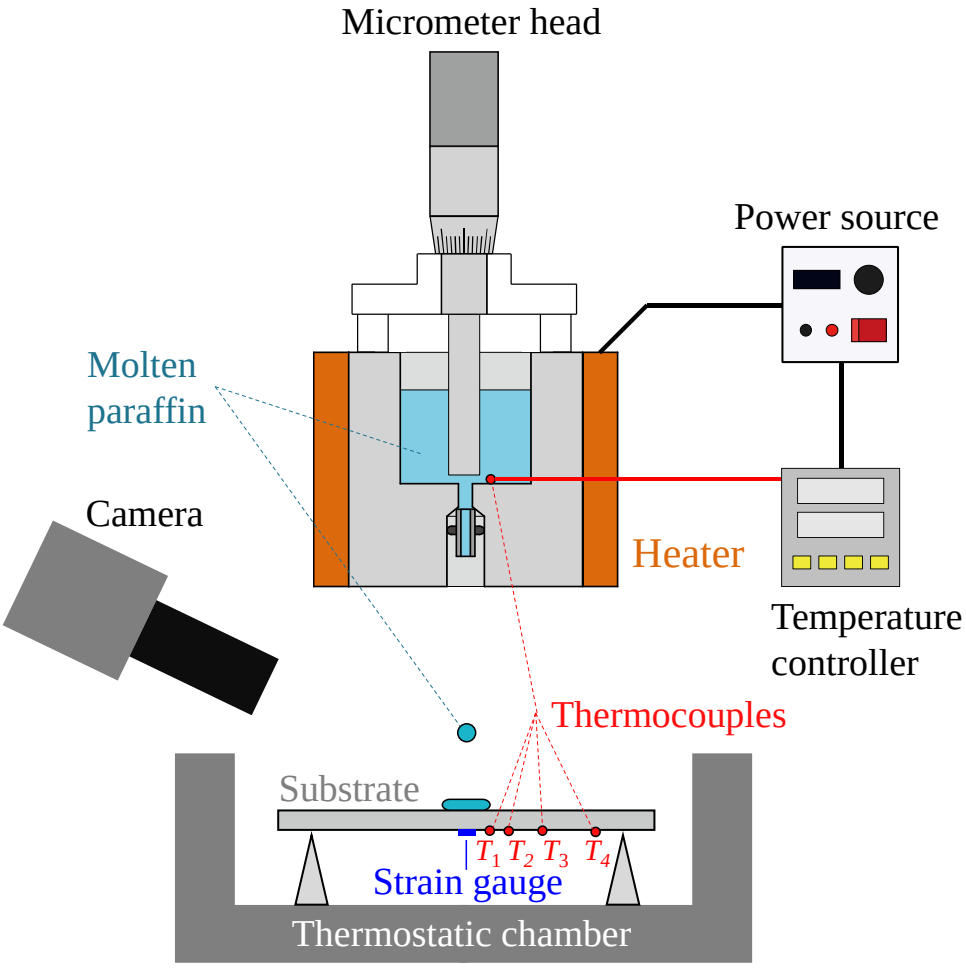

Fig. 3.1 Schematic illustration of the drop experiment setup.

3.2 Experimental condition

Drop experiments were conducted with considering the effects of (A) substrate pre-set temperature, T_{sub}: 0 °C, 5 °C, 10 °C, 15 °C, 20 °C; (B) drop height, H: 20 mm, 50 mm, 100 mm, 200 mm; (C) droplet temperature, T_{drop}: 80 °C, 100 °C, 110 °C, 120 °C, 140 °C; and (D) paraffin wax materials: HNP-9, candle wax. Three to five experiments were conducted for each test condition.

3.3 Geometry of solidified splat

The paraffin droplet was spread and solidified rapidly after being impacted onto the substrate. Figure 3.2(a) shows a picture of an HNP-9 splat when the substrate pre-set temperature was 20 °C, drop height was 50 mm, and droplet temperature was 140 °C.

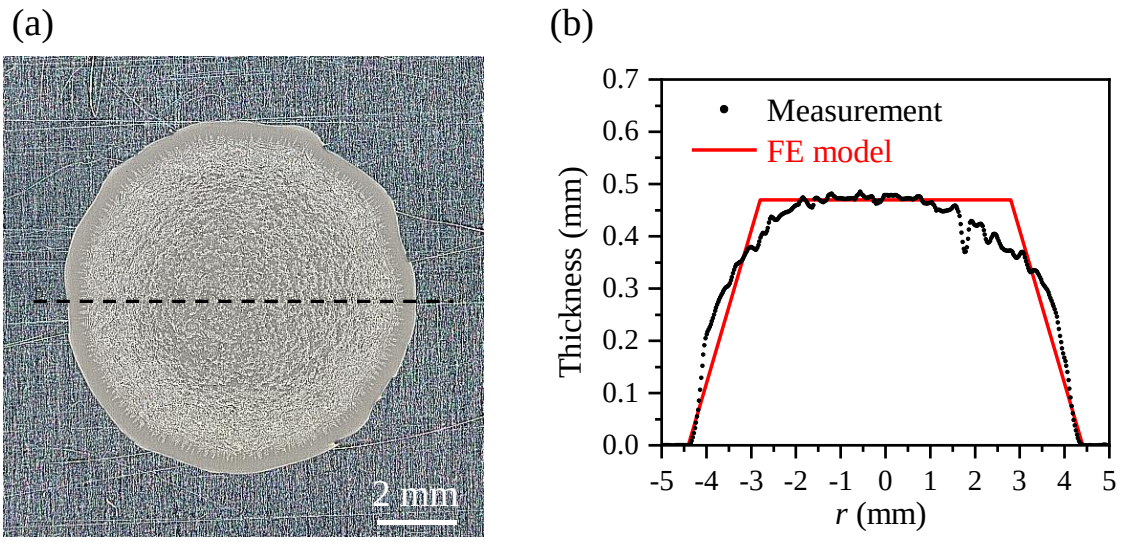

Fig. 3.2 (a) Overview of a solidified splat and (b) measured profile (black plot) along the black line drawn in (a), as well as the simplified trapezoid-shaped curve (red curve). Here, the droplet temperature was 140 °C, drop height was 50 mm, substrate pre-set temperature was 20 °C, and paraffin material was HNP-9.

The shape of the splat was measured by a One-shot 3D Measuring Microscope (VR-3000, Keyence). The measured profile of the solidified splat along its diameter as the black line drawn in Fig. 3.2(a) is plotted in Fig. 3.2(b) in black. Here, the measured splat profile was simplified as a trapezoid-shaped red curve, which is used for FEM analysis in Chapter 5 and Chapter 6.

Measured splat geometries under various drop impact conditions are summarized in Fig. 3.3 with special considerations of the effects of (a) substrate pre-set temperature, (b) drop height, (c) droplet temperature, and (d) paraffin wax materials. These figures reveal that the splat geometry is significantly influenced by the impact conditions; that is thicker splat with a smaller diameter is always formed under lower substrate pre-set temperature, lower drop height, and lower droplet temperature. A Thicker splat was also measured for HNP-9 splat compared with candle wax, which might be caused by the higher melting point and higher viscosity of HNP-9. What should be noted is that the mass of droplet slightly increases with reduction of droplet temperature due to elevated surface tension force. The higher impact velocity also causes a loss of mass due to splashing especially at drop heights above 100 mm [90].

The spreading and solidification process of droplet should be mainly determined by fluid properties such as impact velocity, viscosity, and surface tension force. Several investigations have been carried out focusing on the fluid flow and splat solidification by Mostaghimi et al. [76, 78, 79, 91-94]. Detailed discussion about the fluid issues in molten droplets are out of the scope in this dissertation and will not be furtherly discussed.

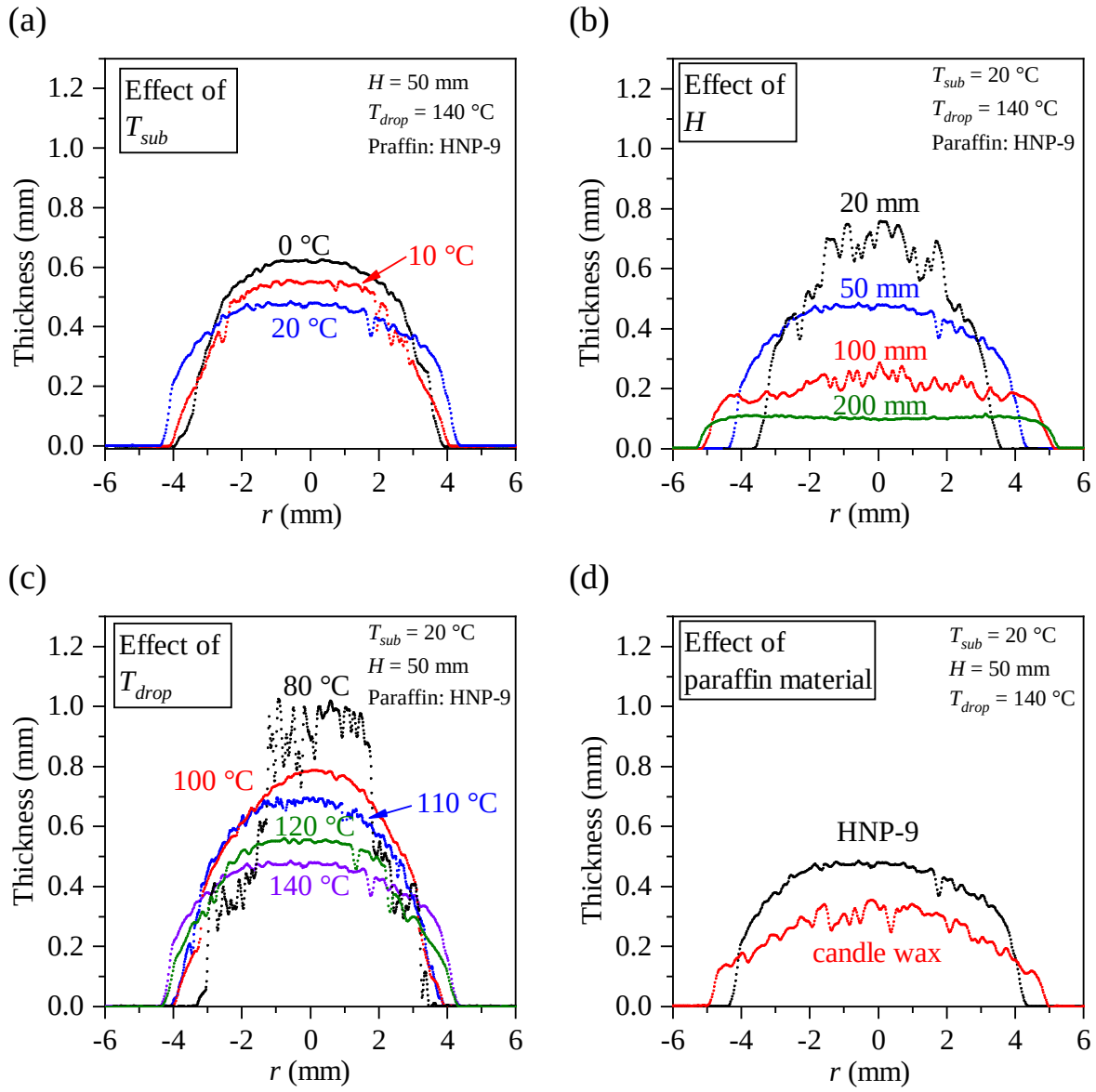

Fig. 3.3 Measured profiles of solidified splats which reveal the effects of (a) substrate pre-set temperature, (b) drop height, (c) droplet temperature, and (d) paraffin wax materials.

3.4 Residual strain

3.4.1 Extraction of residual strain

The primary purpose of this study is to investigate the stress-strain development associated with the adhesion, solidification, and cooling process of the impacted droplet. In this dissertation, the strain component relevant to this process is termed by residual strain (ε_r), which includes the strain due to the solidification process and the thermal strain due to the thermal expansion mismatch between the solidified splat and substrate. In addition to this residual strain, the measured strain ($\varepsilon_{\text{total}}$) at the substrate back surface includes two other components; namely, a thermal strain (ε_{tm}) caused by thermal expansion mismatch between the substrate and the strain gauge, and a thermal strain (ε_{tg}) caused by temperature distribution in the substrate due to transient heat transfer from the droplet. A relation between these strain components is simply given as

$$\varepsilon_{\text{total}} = \varepsilon_r + \varepsilon_{tm} + \varepsilon_{tg} . \tag{3.1}$$

Two kinds of preliminary experiments were conducted to individually identify two thermal strains. To measure ε_{tm}, substrate temperature was changed between -5 ºC and 60 ºC without the paraffin droplet, and the strain change at the substrate back surface was measured. The measured strain is shown in Fig. 3.4 as a function of the substrate temperature T_1. The other thermal strain (ε_{tg}) is generated due to the transient heat transfer, during which the expansion of substrate center is constrained by the surrounding area with relatively lower temperature. To measure this compressive thermal strain, a paraffin droplet was dropped and deposited onto a thin 430 stainless steel plate with the thickness of 0.1 mm which was placed on the middle of the substrate. The 0.1 mm plate and the substrate were separated by a thin oil film (see Fig. 3.5) to remove residual strain (ε_r) from the measured strain. The measured strain here was the summation of ε_{tm} and ε_{tg}. Therefore, ε_{tg} can be obtained by subtracting ε_{tm} from the measured strain in this test. Because ε_{tg} is a function of the temperature distribution in the substrate, which is

influenced by the experimental conditions, a fitting equation was introduced based on the four measured temperatures (T_1, T_2, T_3, and T_4) to evaluate ε_{tg} as in:

$$\varepsilon_{tg} = \alpha_{sub}\left\{-10.4\left(T_1 - T_2\right) + 8.21\left(T_1 - T_3\right) + 3.24\left(T_1 - T_4\right)\right\}. \quad (3.2)$$

Here, α_{sub} is 10.4×10^{-6}/K, the thermal expansion coefficient of 430 stainless steel. In this dissertation, the residual strain ε_r was obtained by subtracting ε_{tg} and ε_{tm} from $\varepsilon_{\text{total}}$.

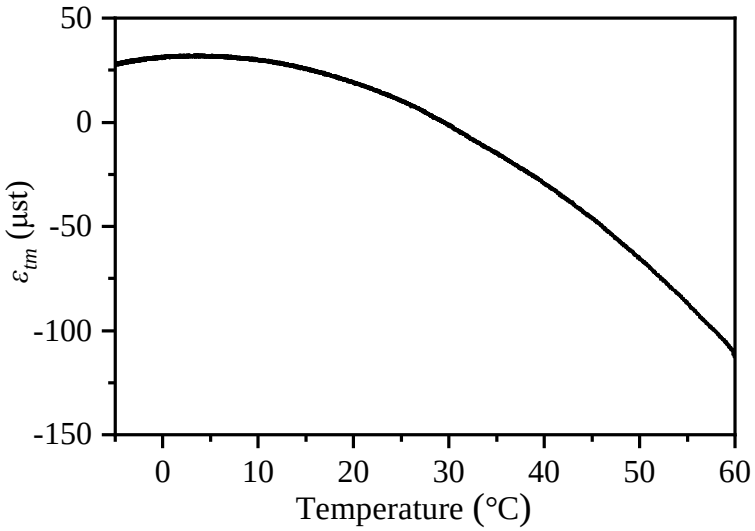

Fig. 3.4 Thermal strain (ε_{tm}) as a function of substrate temperature caused by thermal expansion mismatch between the 430 stainless steel substrate and the strain gauge.

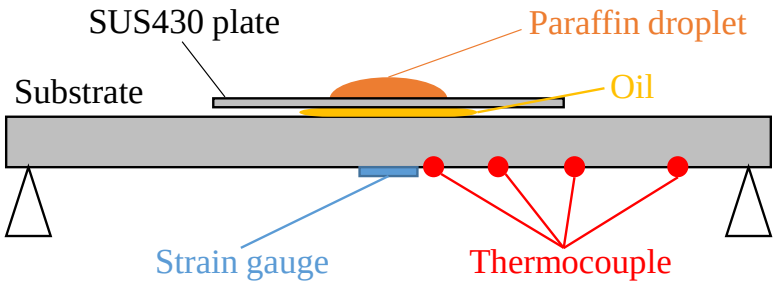

Fig. 3.5 Experimental setup for removing residual strain.

3.4.2 Evolution of residual strain

Specific examples of the evolution of residual strain (ε_r) and substrate temperature (T_1) are drawn in Fig. 3.6 as a function of time for (a) HNP-9 and (b) candle wax, respectively at the droplet temperature of 140 °C, drop height of 100 mm, and substrate pre-set temperature of 10 °C. Here, two residual strains, ε_r (Ch. 1) and ε_r (Ch. 2), measured by the bi-axial strain gauge, show almost comparable values. This proves that in-plane equi-biaxial strains, ε_{rr} and $\varepsilon_{\theta\theta}$, are generated in the circular substrate and splat. In Fig. 3.6, compressive residual strain is measured immediately after the impact of the paraffin droplet. This compressive strain is attributed to the strain constraint induced by the temperature gradient, which could not be fully compensated by Eq. 3.2 due to a rapid transient heat transfer. Nevertheless, this transient compressive strain vanishes several seconds after the impact. Then, the residual strain gradually increases and reaches an equilibrium value when the substrate cools down to the pre-set temperature. As can be seen in Fig. 3.6(b), residual strains rapidly decrease at around 23 seconds. This is caused by the occurrence of cracking in the solidified splats which releases the accumulated residual stress in splats.

The evolution of measured strain in this experiment shows good accordance with that in the actual thermal spraying [35-38]. In the following sections, the residual strain (ε_r), referring to averaged values of Ch. 1 and Ch. 2 when the substrate cools down to the pre-set temperatures, will be mainly focused.

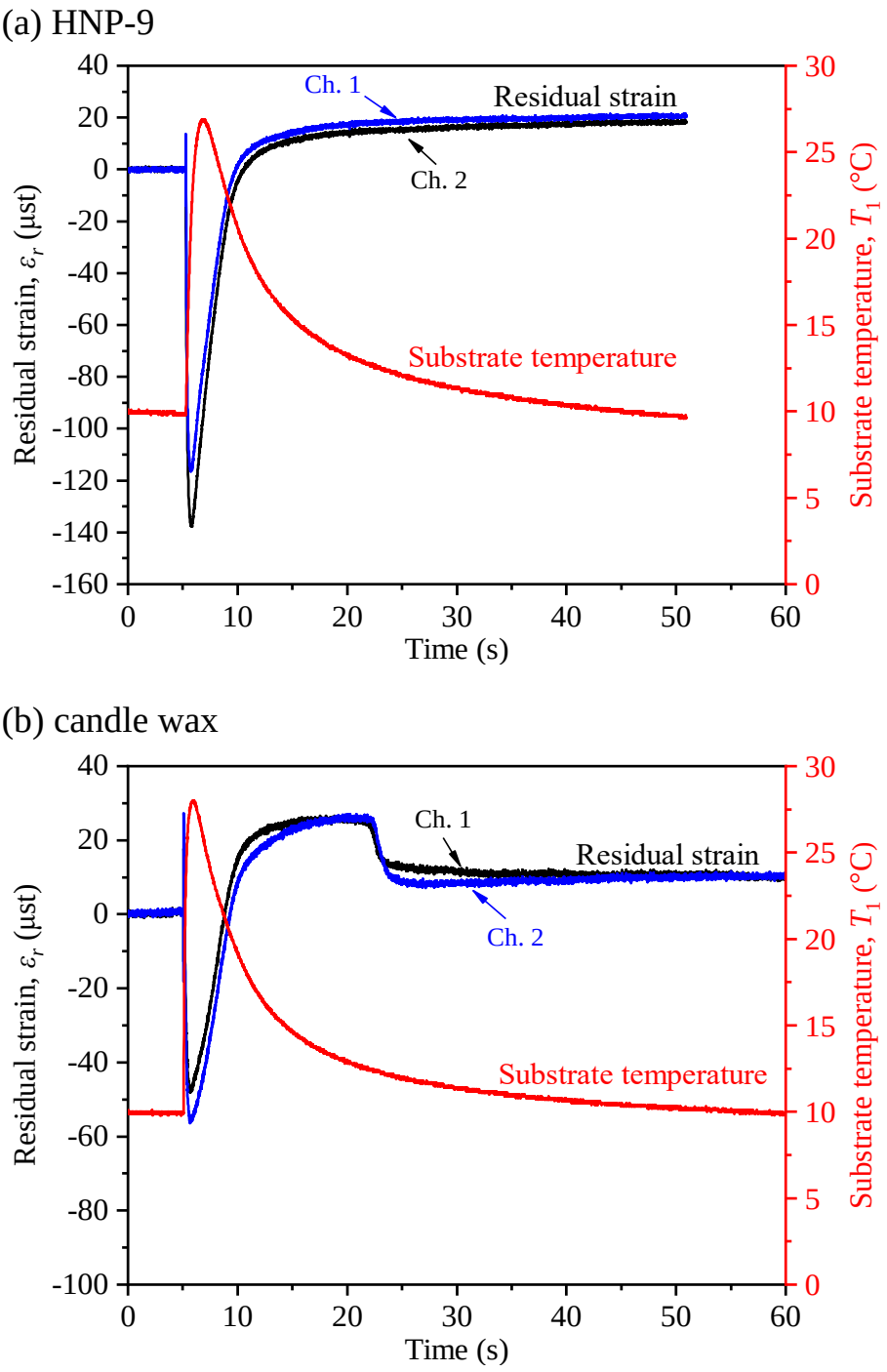

Fig. 3.6 Example of measurements showing the evolutions of residual strains (ε_r) and substrate temperature (T_1) for (a) HNP-9 and (b) candle wax. Substrate pre-set temperature was 10 °C, drop height was 100 mm, and droplet temperature was 140 °C.

3.4.3 Effect of substrate pre-set temperature

Measured residual strains at the steady state are summarized in Fig. 3.7 as a function of substrate pre-set temperature changing from 0 °C to 20 °C with a temperature interval of 5 °C. Averaged values of five experiments are plotted for (a) HNP-9 and (b) candle wax. Results with drop heights of 50 mm and 100 mm are plotted in black and red, respectively. Droplet temperature was fixed at 140 °C for all measurements. In the case of HNP-9 (see Fig. 3.7(a)), the residual strain increases with the reduction of substrate pre-set temperature at both drop heights of 50 mm and 100 mm. This is mainly because the thermal strain in the splat increases with the increase of temperature reduction from the melting point, and thereby results in the larger in-plane normal stress (σ_{rr}) in the splat. The larger splat stress induces the larger bending moment acting on the splat/substrate structure, which increases the substrate curvature and the residual strain measured at the substrate back surface.

As seen from Fig. 3.7(b) residual strains of candle wax have a similar manner with HNP-9. However, the strains slightly decrease at 10 °C for drop height of 100 mm due to the occurrence of vertical cracking in the splats. Figure 3.8 shows photos of solidified candle wax splats under each substrate pre-set temperature at drop heights of (a) 50 mm and (b) 100 mm when droplet temperature was fixed at 140 °C. Cracking is observed when the substrate pre-set temperatures are 5 °C and 10 °C. The cracking would partly release the splat stress, and result in the reduction of the residual strains measured at the substrate back surface. Cracking behaviors will be furtherly discussed in Sec 5.3.

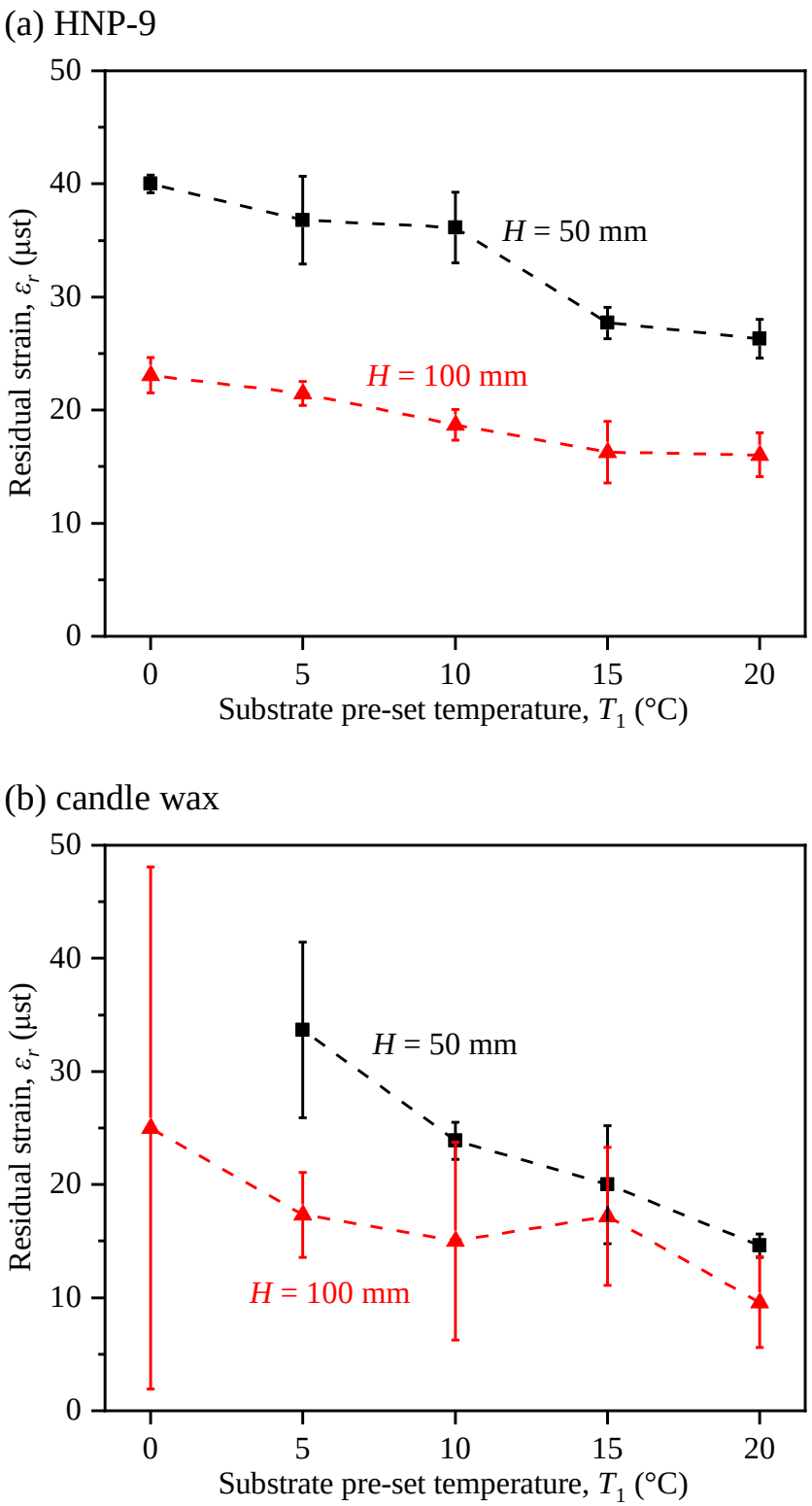

Fig. 3.7 Measured residual strains for (a) HNP-9 and (b) candle wax as a function of substrate pre-set temperature (T_1) at drop heights of 50 mm and 100 mm, and droplet temperature of 140 °C.

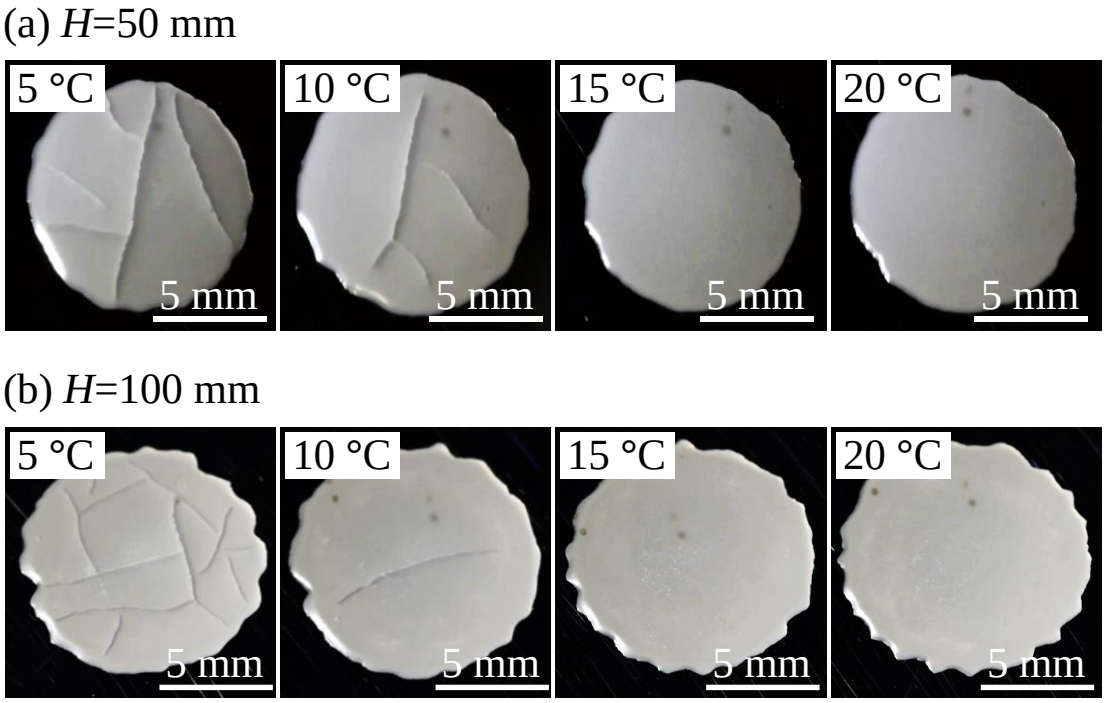

Fig. 3.8 Photos of solidified candle wax splats under each substrate pre-set temperature at drop heights of (a) 50 mm and (b) 100 mm when droplet temperature was fixed at 140 °C. Cracking is observed when the substrate pre-set temperatures are 5 °C and 10 °C.

3.4.4 Effect of drop height

Effect of drop height on residual strains can be also seen in Fig. 3.7. Larger residual strains are always developed at the drop height of 50 mm than that of 100 mm for both paraffin wax materials and all the temperature conditions. This mainly results from the difference in the geometries of splats, as shown in Fig. 3.3(b); namely, a thicker splat is formed by the drop height of 50 mm because of a lower impact velocity. The radial force acting on the splat/substrate interface increases with the increase of splat cross-sectional area. The larger radial force results in a larger bending moment acting on the substrate, and hence leads to a larger curvature in the substrate, as well as larger residual strain at the substrate back surface.

3.4.5 Effect of droplet temperature

Figure 3.9 shows measured residual strains for HNP-9 as a function of droplet temperature at drop height of 50 mm, and substrate pre-set temperature of 20 °C. Same with Fig. 3.7, five experiments were conducted for each temperature condition, and the average values are plotted in this figure. It is found that the residual strain increases as the droplet temperature decreases from 140 °C to 100 °C, and decreases at 80 °C. This temperature dependency is mainly attributed to temperature-dependent splat geometries and debonding behaviors of splats. As shown in Fig. 3.3(c), a lower droplet temperature leads to a thicker splat, which is mainly due to the higher viscosity. And it prevents sufficient flatting of impacted droplet. In other words, higher residual strain is measured when droplet temperature drops from 140 °C to 100 °C due to the thicker splat. However, the residual strain stops to decrease when droplet temperature continues to decrease to 80 °C. This opposite tendency at 80 °C is associated with the occurrence of splat debonding from the substrate. Photos of solidified HNP-9 splats are compared in Fig.

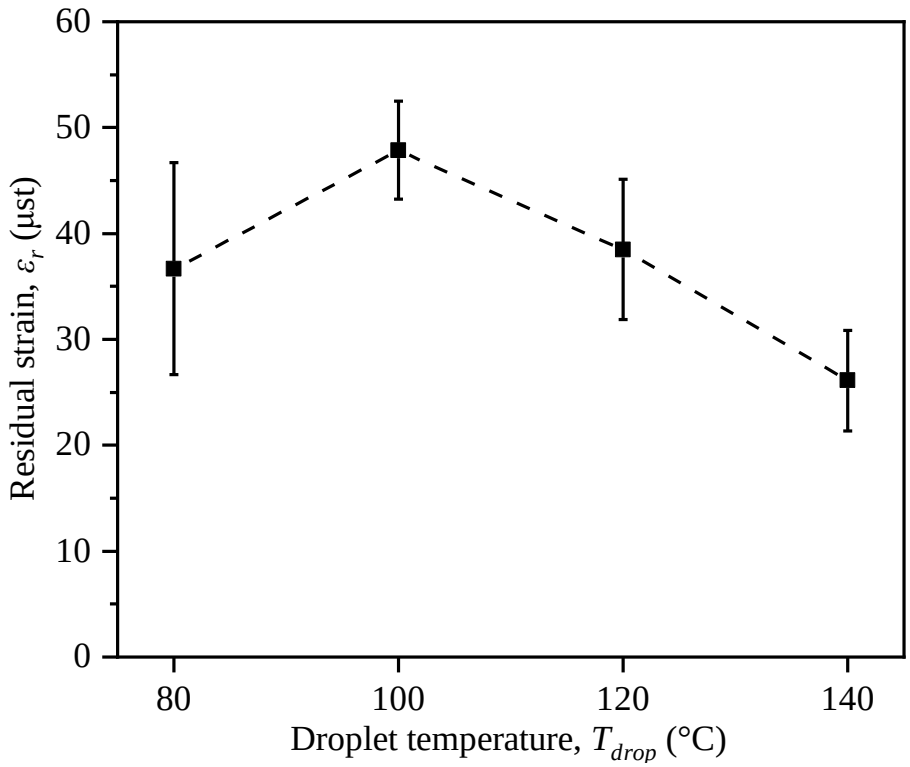

Fig. 3.9 Measured residual strains for HNP-9 as a function of droplet temperature at the substrate pre-set temperature of 20 °C, and drop height of 50 mm.

3.10 for each droplet temperature when the other drop impact conditions are same with Fig. 3.9. As shown in the figure, debonding, which partly releases residual strains is originated at the periphery of the splat at 80 °C.

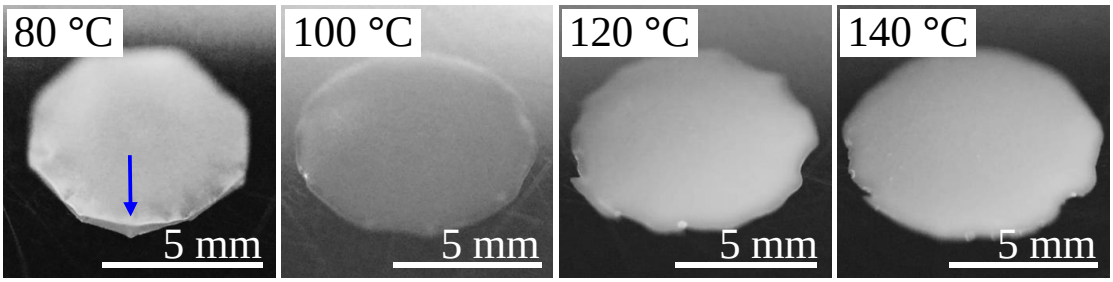

Fig. 3.10 Photos of solidified HNP-9 splats under each droplet temperature. The other experimental conditions are same with Fig. 3.9. A debonding area is indicated by a blue arrow at 80 °C.

3.4.6 Effect of paraffin wax material

Measured residual strains in Fig. 3.7 are replotted in Fig. 3.11 to discuss the effect of paraffin wax materials. It is found that the residual strain of HNP-9 is generally larger than that of candle wax. This difference in residual strain between two types of paraffin wax is attributed to their various characterizations, including Young's modulus, thermal expansion coefficient, melting point, and geometry of solidified splat. Basically, it can be speculated that larger Young's modulus, larger thermal expansion coefficient, higher melting point, and thicker splat lead to larger residual strain. Detailed evaluation of residual strain will be discussed based on FEM analysis in Sec. 6.2.

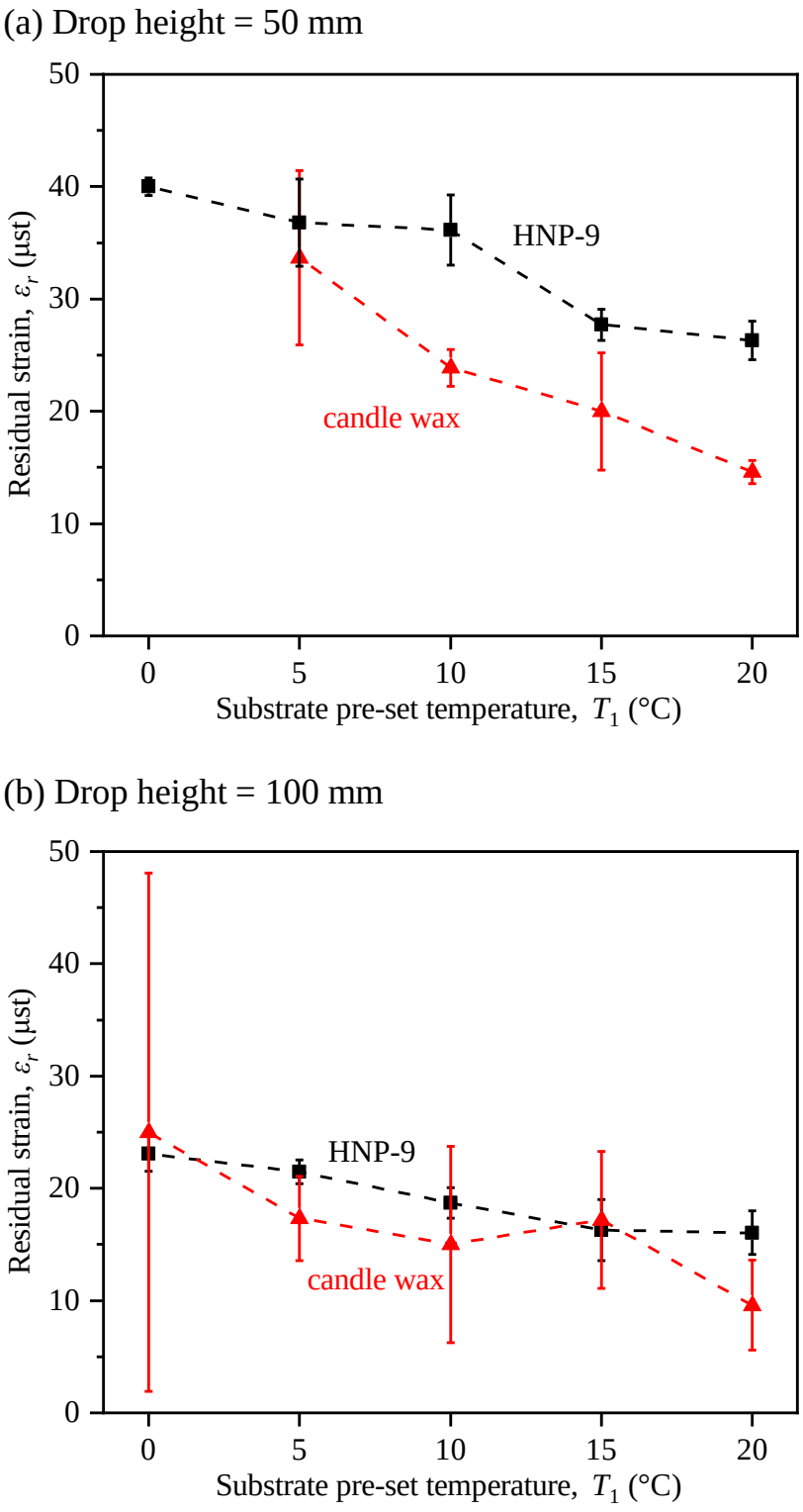

Fig. 3.11 Comparison of residual strains for candle wax and HNP-9 under each substrate pre-set temperature at drop heights of (a) 50 mm and (b) 100 mm when the droplet temperature was fixed at 140 °C.

3.5 Cracking

Cracking was only observed in solidified candle wax splats under certain drop impact conditions. Cracking behaviors of candle wax splats are summarized in Fig. 3.12 under various conditions. Here, cracking was judged according to the photos when the splat temperature was cooled down to the substrate pre-set temperature. Results of three independent tests are presented for each test condition. It can be seen that cracking only occurs at substrate pre-set temperatures of 10 °C and 0 °C, as discussed in Sec. 3.4. This substrate pre-set temperature dependent cracking behaviors will be furtherly discussed in Sec. 5.3. It can also be found that only a few splats crack at drop height of 20 mm even though when the substrate pre-set temperature is as low as 0 °C. This is because splat debonding usually occurred before splat cracked at the drop height of 20 mm, which partly released residual stress in splats and prevented the occurrence of cracking. The debonding behavior will be furtherly discussed in Sec. 3.6.

Cracking of candle wax splat　　– No cracking　　× Splat cracking

		T_{sub} : 0 °C			T_{sub} : 10 °C			T_{sub} : 20 °C		
Height	T_{drop}	1st	2nd	3rd	1st	2nd	3rd	1st	2nd	3rd
20 mm	80°C	–	–	–	–	–	–	–	–	–
	100°C	–	–	–	–	–	–	–	–	–
	110°C	–	–	–	–	×	–	–	–	–
	120°C	×	–	–	–	–	–	–	–	–
	140°C	×	×	×	–	–	–	–	–	–
50 mm	80°C	–	–	–	–	×	×	–	–	–
	100°C	×	×	×	×	–	–	–	–	–
	110°C	×	×	×	–	–	×	–	–	–
	120°C	×	×	×	×	×	×	–	–	–
	140°C	×	×	×	×	×	×	–	–	–
100 mm	80°C	×	–	–	×	×	×	–	–	–
	100°C	×	×	×	×	×	×	–	–	–
	110°C	×	×	×	×	×	×	–	–	–
	120°C	×	×	×	×	×	×	–	–	–
	140°C	×	×	×	×	×	×	–	–	–
200 mm	80°C	×	×	×	×	×	×	–	–	–
	100°C	×	×	×	×	×	×	–	–	–
	110°C	×	×	×	×	×	×	–	–	–
	120°C	×	×	×	×	×	×	–	–	–
	140°C	×	×	×	×	×	×	–	–	–

Fig. 3.12 Summary of cracking behaviors of solidified candle wax splats. Cross means cracking occurred, while short line means cracking did not occur.

3.6 Debonding

Fig. 3.13 summarizes the observed debonding behaviors of (a) HNP-9 and (b) candle wax, in which results of three independent tests are presented for each test condition. Solid circle (●) and triangle (▲) mean debonding and minor debonding, respectively. While hollow circle (○) means no debonding. Debonding was judged according to the photos when the splat temperature was cooled down to the substrate pre-set temperature. The minor debonding was defined as the behavior that debonding area was less than 5% of the interface area. Fig. 3.14 presents typical photos of solidified splats with (a) debonding, (b) minor debonding, and (c) no debonding. The test condition for each splat is indicated as Fig. 3.14(a)-(c) in Fig. 3.13. To clarify the relationship between test conditions and splat debonding, the results in Fig. 3.13 are replotted in Fig. 3.15. The symbols in Fig. 3.15 have the same meaning as those in Fig. 3.13. In Fig. 3.15, a "debonding area" is highlighted in each graph. The inserts (1)-(9) indicate the nine conditions of scraping tests that are conducted to evaluate the adhesion strength and will be discussed in Chapter 4.

It is found in Fig. 3.13 and Fig. 3.15 that the test conditions significantly affect the debonding behaviors. It can be summarized that the debonding is more likely to occur at lower substrate pre-set temperatures, lower drop heights, and lower droplet temperatures. In addition, HNP-9 splats are found to debond more easily than candle wax splats.

It is generally accepted that interfacial debonding occurs when the peeling stress and interfacial shear stress exceed the adhesion strength. In thermal spraying, the bonding between coating and substrate is mainly associated with the mechanical interlocking, which is highly related to the roughness of substrate surface and the characteristics of impacting droplets [95-98]. In some cases, inter-diffusion and chemical reactions may take place near the interface and contribute to the bonding when the substrate is partly melted by the high-temperature droplet [96, 98]. In this experiment, because the droplet temperature is low enough compared with the melting point of substrate, the dominant bonding mechanism is expected to be the mechanical interlocking generated when liquid

droplets fill and solidify in the cavities of substrate surface. The adhesion strength, therefore, varies with impact conditions which affect the amount of liquid penetration into substrate surface cavities. On the other hand, driving forces for debonding, which are the peeling stress and the shear stress, are influenced by many factors such as splat geometry, the residual radial stress in splat (σ_{rr}), and interfacial adhesion. In this section, effects of droplet impact conditions on debonding driving forces are discussed by focusing on splat stress (σ_{rr}) and splat thickness (t_{sp}).

Considering an equi-biaxial plane stress state ($\sigma_{rr} = \sigma_{\theta\theta}$ and $\sigma_{zz} = 0$), and ignoring the creep deformation and stress relaxation at the interface, the splat stress (σ_{rr}) can be described by

$$\sigma_{rr} = \frac{1}{1-\nu} \cdot E_{sp}\left(T_{sub}\right) \cdot \alpha_{sp} \cdot \left(T_{sf} - T_{sub}\right), \tag{3.3}$$

where v, α_{sp}, and T_{sf} refer to Poisson's ratio, thermal expansion coefficient, and stress free temperature of splat, respectively. T_{sub} refers to substrate pre-set temperature, and E_{sp} (T_{sub}) means Young's modulus of the splat at the temperature of T_{sub}.

(a) HNP-9 ● Debonding ▲ Minor debonding ○ No debonding

		T_{sub} : 0 °C			T_{sub} : 10 °C			T_{sub} : 20 °C		
Height	T_{drop}	1st	2nd	3rd	1st	2nd	3rd	1st	2nd	3rd
20 mm	80°C	●	●	●	●	●	●	●	●	●
	100°C	●	●	●	●	●	●	○	○	○
	110°C	●	●	●	●	●	●	○	○	○
	120°C	●	●	●	○	○	●	○	○	○
	140°C	●	●	▲	○	○	○	○	○	○
50 mm	80°C	●	●	●	Fig. 3.14(a) ●	●	●	●	●	●
	100°C	●	●	●	●	●	●	○	○	○
	110°C	●	●	●	Fig. 3.14(b) ▲	▲	▲	○	○	○
	120°C	●	●	●	○	○	○	○	○	○
	140°C	▲	▲	▲	Fig. 3.14(c) ○	○	○	○	○	○
100 mm	80°C	●	●	●	●	●	●	●	●	●
	100°C	●	●	●	○	○	○	○	○	○
	110°C	●	●	●	○	○	○	○	○	○
	120°C	●	●	●	○	○	○	○	○	○
	140°C	○	▲	●	○	○	○	○	○	○
200 mm	80°C	●	●	●	●	●	●	●	●	●
	100°C	●	●	●	○	○	○	○	○	○
	110°C	●	●	●	○	○	○	○	○	○
	120°C	●	●	●	○	○	○	○	○	○
	140°C	○	○	○	○	○	○	○	○	○

(b) candle wax

		T_{sub} : 0 °C			T_{sub} : 10 °C			T_{sub} : 20 °C		
Height	T_{drop}	1st	2nd	3rd	1st	2nd	3rd	1st	2nd	3rd
20 mm	80°C	●	●	●	●	●	●	●	○	●
	100°C	●	●	●	●	●	●	○	○	○
	110°C	●	●	●	▲	●	○	○	○	○
	120°C	●	●	●	○	●	●	○	○	○
	140°C	●	●	●	○	○	○	○	○	○
50 mm	80°C	●	●	●	○	○	○	○	○	○
	100°C	●	●	●	○	○	○	○	○	○
	110°C	●	●	▲	○	○	○	○	○	○
	120°C	▲	●	●	○	○	○	○	○	○
	140°C	○	○	○	○	○	○	○	○	○
100 mm	80°C	▲	●	●	○	○	●	○	○	○
	100°C	▲	▲	▲	○	○	○	○	○	○
	110°C	○	○	○	○	○	○	○	○	○
	120°C	○	○	○	○	○	○	○	○	○
	140°C	○	○	○	○	○	○	○	○	○
200 mm	80°C	●	●	●	○	○	○	○	○	○
	100°C	○	○	▲	○	○	○	○	○	○
	110°C	○	○	○	○	○	○	○	○	○
	120°C	○	○	○	○	○	○	○	○	○
	140°C	○	○	○	○	○	○	○	○	○

Fig. 3.13 Summary of debonding behaviors of solidified (a) HNP-9 and (b) candle wax splats. Solid circle means debonding; triangle means minor debonding, in which the debonding area was less than 5% of the interface area; hollow circle means no debonding. Results of three independent tests are presented for each test condition. The inserts of Fig. 3.14(a)-(c) in (a) indicate test conditions of Fig. 3.14.

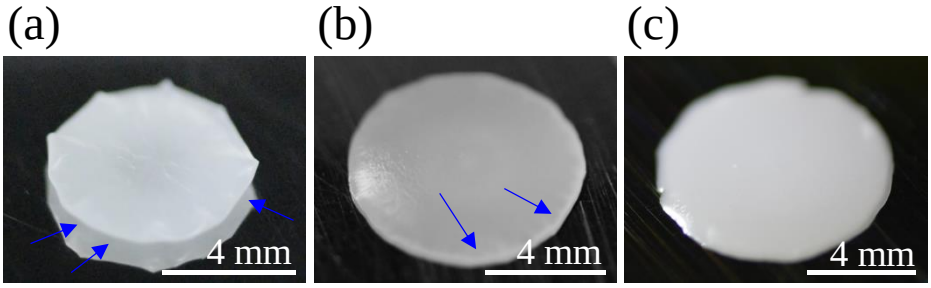

Fig. 3.14 Typical photos of solidified splats with (a) debonding, (b) minor debonding, and (c) no debonding. Debonding is indicated by blue arrows. The test condition for each splat is indicated as Fig. 3.14(a)-(c) in Fig. 3.13.

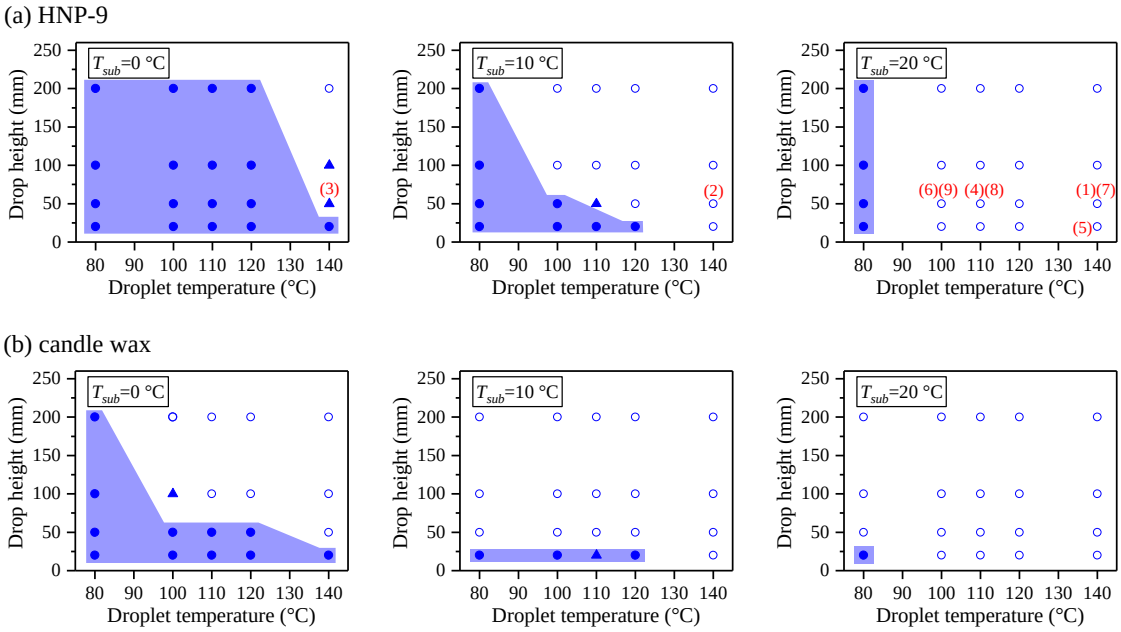

Fig. 3.15 Drop test results of debonding behaviors for (a) HNP-9 and (b) candle wax when the substrate pre-set temperatures were 0 °C, 10 °C, and 20 °C. The symbols have the same meaning as those in Fig. 3.13. A "debonding area" is highlighted in each graph. The inserts (1)-(9) indicate the nine scraping test conditions which will be discussed in Chapter 4.

3.6.1 Effect of substrate pre-set temperature

As can be seen in Fig. 3.13 and Fig. 3.15, the splats tend to debond during drop experiments associated with the reduction of substrate pre-set temperatures. This is caused by both the lower interfacial adhesion strength and larger debonding driving forces

generated at lower substrate pre-set temperatures. First, the lower substrate pre-set temperatures accelerate the solidification of paraffin wax droplets, and thereby reduce the amount of liquids that penetrate into the surface cavities of substrates. As a result, the strength of the interfacial mechanical interlocking, which dominates the adhesion strength becomes lower as substrate temperature decreases. On the other hand, driving forces for debonding increase with the reduction of substrate pre-set temperature due to the larger radial thermal stresses (σ_{rr}) in splats (see Eq. 3.3). The larger radial stress generates larger bending moment in substrates, hence inducing larger driving forces at the interface. Additionally, as drawn in Fig. 3.3(a), the splat thickness (t_{sp}) becomes larger at lower substrate pre-set temperatures, which can also increase the magnitude of debonding driving forces. The relationship between splat geometries and magnitude of driving forces will be quantified in Chapter 6 using FE analysis.

3.6.2 Effect of drop height

As can be seen in Fig. 3.13 and Fig. 3.15, debonding is prone to appear at a lower drop height. Similar to the case of substrate pre-set temperature, the effect of drop height on debonding behaviors can be explained by adhesion strength and debonding driving forces. Distribution of the maximum impact pressure of a liquid droplet impacting a solid surface can be described by [99]

$$p(r)=\frac{1}{2}\rho_{sp}V_{sp}{}^{2}\cdot e^{-\frac{r^2}{A_2}}, \tag{3.4}$$

where ρ_{sp} and V_{sp} are the density and velocity of the splat; r refers to the radial coordinate. A_2 can be written as

$$A_2=-4R_{sp}{}^{2}\left[\ln\frac{10^{-10}}{\frac{1}{2}\rho_{sp}V_{sp}{}^{2}}\right]^{-1}, \tag{3.5}$$

where R_{sp} is the splat radius. It is found in Eq. 3.4 and Eq. 3.5 that pressure, p, becomes larger at a higher drop height which induces higher impact velocity, V_{sp}. It suggests that larger amount of liquids can be pressed into surface cavities to form a stronger bonding at a higher drop height. On the other hand, driving forces for debonding increase with the reduction of drop height due to the thicker splat (see Fig. 3.3(b)) associated with the lower impact velocity. Consequently, the larger driving forces coupled with the weaker interfacial adhesion strength caused the splat to debond at a lower drop height.

3.6.3 Effect of droplet temperature

Droplet temperature is another important factor that influences the debonding behaviors. Lower droplet temperatures facilitate the occurrence of debonding as seen in Fig. 3.13 and Fig. 3.15. This can be explained by the weaker interfacial adhesion and larger debonding driving forces generated at lower droplet temperatures. Firstly, owing to low droplet temperatures, the adhesion strength becomes weak due to the quick solidification process and also due to the larger viscosities which prevent the liquid from flowing into substrate cavities. Secondly, the splats formed under lower droplet temperatures are thicker (see Fig. 3.3(c)) due to larger viscosities which restrict the droplets to sufficiently spread. As discussed above, the thicker splats always generate larger driving forces for debonding.

3.6.4 Effect of droplet materials

Comparing the debonding behaviors of candle wax and HNP-9 as shown in Fig. 3.13 and Fig. 3.15, candle wax splats are found more difficult to debond, particularly at lower droplet temperatures and higher drop heights. Three possible reasons might contribute to this result. The first one is attributed to the different melting points. As summarized in Table 2.1, HNP-9 has a melting point about 20 °C higher than candle wax. This leads to quicker solidification and shorter flowing processes of HNP-9 droplets, particularly when droplet temperatures are comparable to their melting points. The interfacial bonding is therefore weakened due to weaker mechanical interlocking. As a result, HNP-9 splats

debonded for all drop heights and substrate pre-set temperatures at a droplet temperature of 80 °C, which is just above its melting point. Second, as shown in Fig. 3.3(d), the HNP-9 splat is thicker than candle wax under identical experimental conditions. As has been discussed above, the thicker splat generated larger interfacial driving forces, and thereby facilitated the occurrence of debonding. The third possible reason refers to that the candle wax splats cracked at substrate pre-set temperatures of 10 °C and 0 °C (see Fig. 3.12). The vertical cracking released radial stresses in splats and debonding driving forces at the interface, and hence prevented the splat from debonding. In fact, as shown in Fig. 3.12 and Fig. 3.13, debonding occurs similarly for candle wax and HNP-9 when cracking does not occur.

3.7 Stress relaxation test

Due to the low melting points of paraffin wax materials, creep can occur in HNP-9 and candle wax splats at the ambient temperature of 20 °C. To quantitatively evaluate the creep in solidified paraffin splat, stress relaxation tests were carried out using a drop impact setup [89] similar to Fig. 3.1. Paraffin droplet with a temperature of 140 °C was dropped from a height of 100 mm onto a stainless steel substrate with a pre-set temperature of 20 °C. After the impact, temperature of the splat and substrate cooled down and became stable in around 60 s, which is similar to the drop experiment. In the stress relaxation test, substrate temperature was then maintained at 20 °C for several hours. The evolution of strains at the substrate back surface was measured during the cooling and temperature-holding process.

The measured strains are plotted in Fig. 3.16 for (a) HNP-9 and (b) candle wax as a function of time. In the figures, the strains reach the largest values in about 60 s and then decrease with the subsequent holding process due to creep. The reduction rates of strains decrease with time. This is because the stress in the splat has been partly released due to the creep, resulting in the reduction of creep rate. These results reveal that creep of

paraffin splat shows a critical influence on strain evolution and therefore is necessary to be considered when predicting the evolution of residual strains.

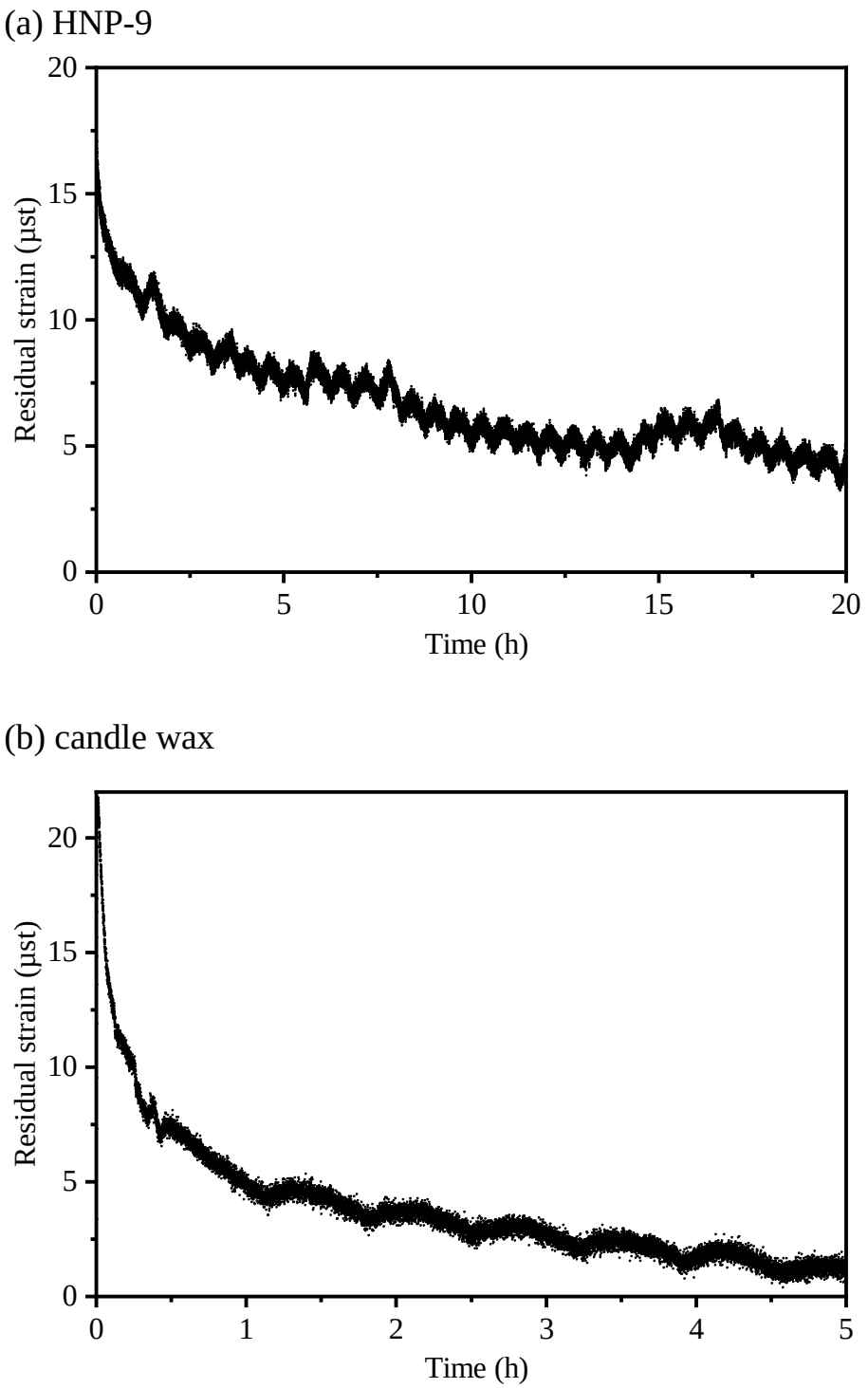

Fig. 3.16 Evolutions of residual strains during the stress relaxation tests with (a) HNP-9 and (b) candle wax.

3.8 Summary

This chapter focuses on paraffin drop impact experiments. Drop experiments were conducted to measure the residual strain evolution and observe cracking and debonding behaviors under various conditions. A stress relaxation test was conducted to quantify creep deformation in a solidified splat. The main results are as follows.

- Evolution of strain at substrate back surface was measured during the solidification and cooling of impacted paraffin droplet. The strain at steady-state when substrate temperature drops down to the pre-set temperature was termed as residual strain.
- Larger residual strain was measured under lower substrate pre-set temperature, lower drop height, and lower droplet temperature. Larger residual strain was measured for HNP-9 compared with candle wax. Residual strain was partly released when either cracking or debonding occurred.
- Cracking was observed in candle wax splat, especially under low substrate pre-set temperature and high drop height. Debonding was observed in both candle wax and HNP-9. It was more likely to occur at lower substrate pre-set temperature, lower drop height, and lower droplet temperature. This is governed by both the interfacial adhesion strength and the values of driving forces.
- Results of stress relaxation test revealed that residual strain was significantly released due to creep after being placed at 20 °C for several hours.

Chapter 4

Scraping test to measure adhesion strength

The scraping test was conducted aiming at evaluating the adhesion strength of solidified splats after the drop experiment.

4.1 Test setup

An experimental setup for scraping test is schematically shown in Fig. 4.1. The stainless steel substrate with a solidified paraffin splat was vertically placed on a steel block. The

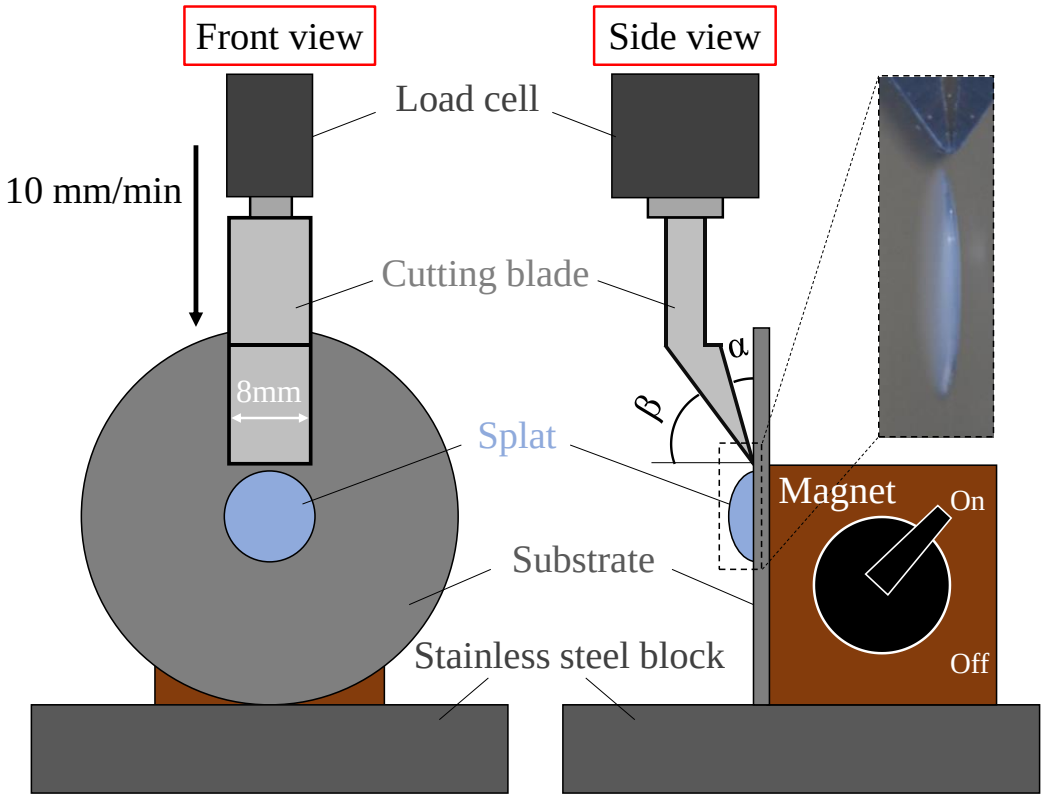

Fig. 4.1 Schematic illustration of the scraping test setup.

substrate was completely supported and restricted by a magnet. The width of the cutting blade is 8 mm which is comparable to the splat diameters. The relief angle (α) and rake angle (β) were 6.1° and 54°, respectively. Here, the rake angle is specifically adjusted so that the solidified splat can be perfectly scraped off with a relatively large scraping force. A load cell (DBS-200N, San-ei Instruments) was installed between the cutting blade and the crosshead of a universal testing machine (LSC-02/30-2, Tokyo Koki Testing Machine). During the scraping tests, the cutting blade was moved vertically downward with a velocity of 10 mm/min until the splat was scraped off completely. The forces in the vertical direction were measured by the load cell during the scraping processes. The blade was slightly pressed onto the substrate so that the splat could be scraped off along the interface. Therefore, a small friction force less than 0.3 N was included in the measured force throughout the scraping processes. The scraping force was obtained by subtracting this small friction force from the measured force. The magnet was confirmed not to affect the scraping force.

4.2 Test condition

Scraping tests were conducted under nine test conditions, which are indicated as (1) to (9) in Table. 4.1. Paraffin wax material was HNP-9. The effects of (A) substrate pre-set temperature, (B) drop height (impact velocity), (C) droplet temperature, and (E) residual stress level in splats were examined by six groups of tests as summarized in the table. Groups (E1), (E2) and (E3) were conducted to examine the effect of (E) residual stress for droplet temperatures of 100 °C, 110 °C and 140 °C, respectively. Three independent tests were conducted for each test condition. All scraping tests were done at room temperature.

During the drop experiments, residual stresses are generated in splats due to thermal contraction of splats and thermal mismatch between splats and substrates. In the scraping tests, the level of residual stress was changed as a test variable, which was controlled by

creep-induced residual stress relaxation as discussed in Sec. 3.7. In Table 4.1, the "Low" residual stress level means that the scraping tests were done when residual stresses in splats were released, which was achieved by placing the substrate with splats for 20 hours at ambient temperatures. On the other hand, the "High" residual stress level was achieved by conducting scraping tests immediately after the impact and solidification of droplets. Here, the time interval between the droplet impacts and starting points of scraping tests was unified at 5 minutes. According to Fig. 3.16, about 70% of the residual stresses in HNP-9 splats are released after being placed at 20 °C for 20 hours, while less than 5% of the stresses are released in the first 5 minutes. In the drop test, the debonding of splats is influenced by both the adhesion strength and residual stress in splats. To eliminate the effect of the residual stress on scraping test results, as in Table 4.1, residual stress levels

Table 4.1 Conditions of scraping tests. Paraffin wax material was HNP-9.

Conditions of scraping tests	**(1)**	**(2)**	**(3)**	**(4)**	**(5)**	**(6)**	**(7)**	**(8)**	**(9)**
Substrate pre-set temperature, T_{sub} (°C)	20	10	0	20	20	20	20	20	20
Drop height, H (mm)	50	50	50	50	20	50	50	50	50
Droplet temperature, T_{drop} (°C)	140	140	140	110	140	100	140	110	100
Residual stress level in splats	Low	Low	Low	Low	Low	Low	High	High	High
Groups to examine the effect of each condition									
A: effect of T_{sub}	●	●	●						
B: effect of H	●				●				
C: effect of T_{drop}	●			●		●			
E1: effect of residual stress at T_{drop} = 100 °C						●			●
E2: effect of residual stress at T_{drop} = 110 °C				●				●	
E3: effect of residual stress at T_{drop} = 140 °C	●						●		

in splats of Groups (A), (B), and (C) were all set to “Low”. Scraping tests (7)-(9) were specifically conducted using the splats with high residual stress to examine the effect of (E) residual stress.

4.3 Displacement-force curve

Generally, two types of test phenomena were observed during the scraping processes. One refers to symmetrical increasing and decreasing of scraping force. The other type of test phenomenon indicates that the splat was completely removed from the substrate associated with the abrupt reduction of scraping force. Typical results for two types of test phenomena are plotted in Fig. 4.2 with schematic illustration of the relevant mechanisms of scraping processes. It is found that three independent tests for each condition show almost comparable displacement-force curves, which confirms that the scraping test in this study reveals well reproducibility. In Fig. 4.2(a), symmetrical curves are measured due to the symmetrical geometry of the splats. Here, scraping force firstly increases from the point ① to ③ as the cutting blade moves from the periphery to the center of the splat, where the scraping breadth and splat thickness reach the largest value. The scraping force then decreases with the reduction of scraping breadth and splat thickness until the splat is totally scraped off. Here, the scraping breadth refers to the contacting length between the blade tip and the splat. In Fig. 4.2(b), the splat is completely removed from the substrate at point ③ associated with rapid reduction of the scraping force. It can be speculated that the removal of splat occurs when the scraping force reaches a critical value inducing rapid crack propagation along the interface.

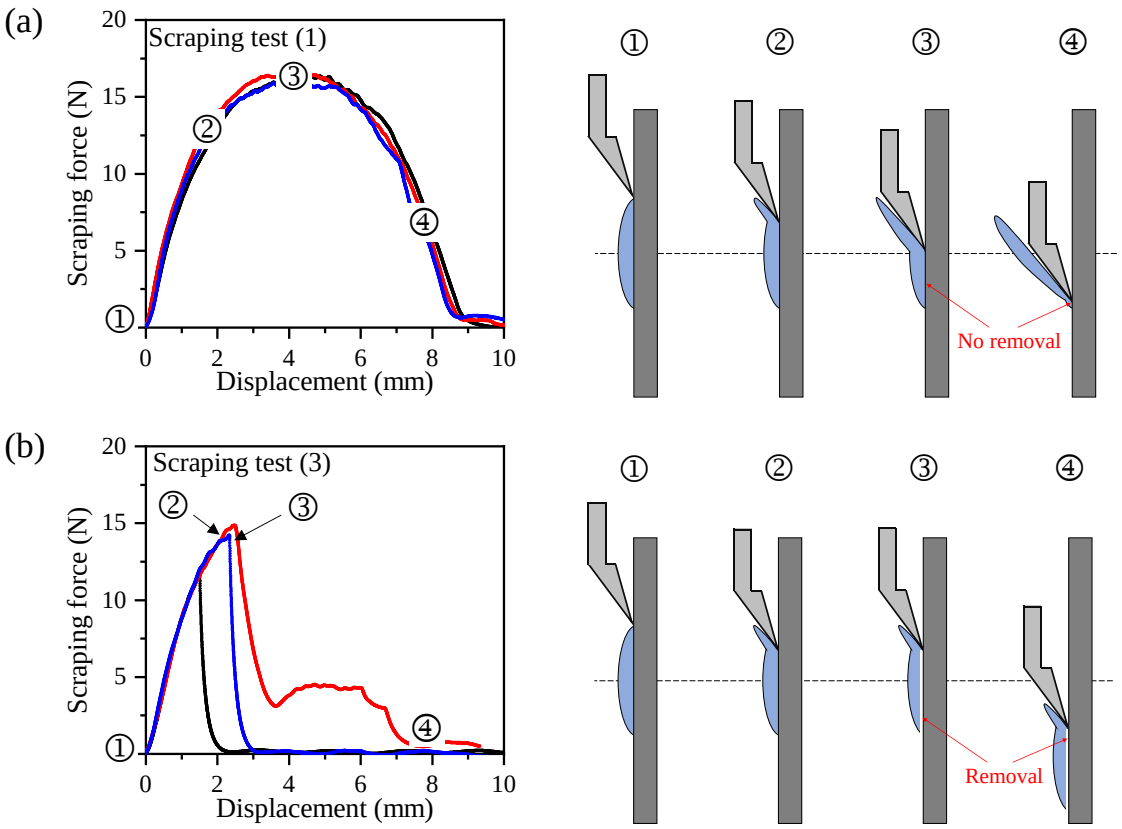

Fig. 4.2 Typical measurements for two types of test phenomena as well as the schematic illustration of the relevant mechanisms of scraping processes. Three independent tests are conducted for each condition. (a) Scraping test (1), symmetrical increasing and decreasing of scraping force without removal of the splat all through the scraping process. (b) Scraping test (3), abrupt reduction of scraping force when the splat is completely removed.

Measured displacement-force curves under all the nine drop test conditions are presented in Fig. 4.3 to investigate the effects of (a) substrate pre-set temperature (T_{sub}), (b) drop height (H), (c) droplet temperature (T_{drop}) under low residual stress, and (d) droplet temperature (T_{drop}) under high residual stress. In Fig. 4.3, only a representative curve is plotted for each test condition. The droplet impact conditions for each scraping test are indicated in Fig. 3.15 as (1)-(9).

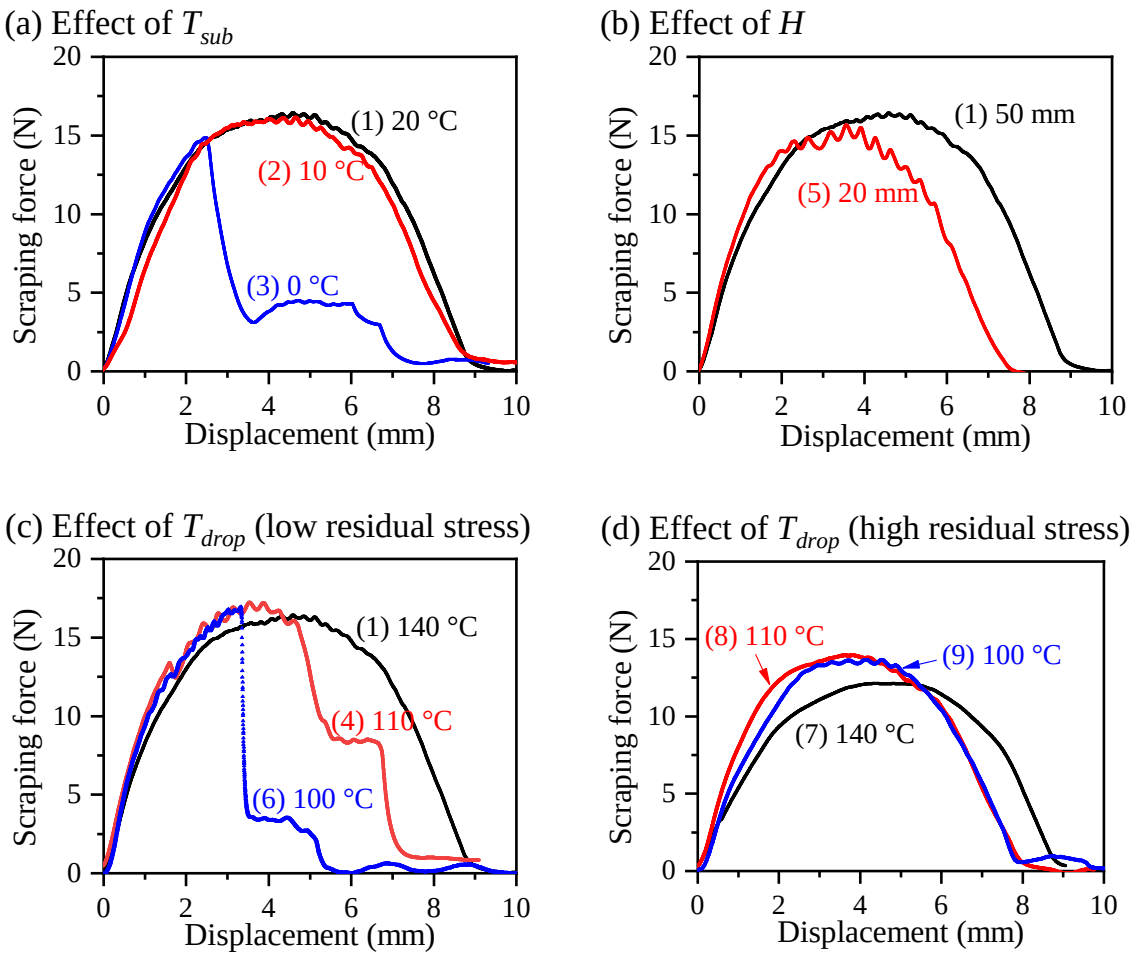

Fig. 4.3 Measured scraping forces as a function of scraping displacement to investigate the effects of (a) substrate pre-set temperature (T_{sub}), (b) drop height (H), (c) droplet temperature (T_{drop}) under low residual stress, and (d) droplet temperature (T_{drop}) under high residual stress. The droplet impact conditions for each scraping test are indicated in Fig. 3.15 as (1)-(9).

4.4 Effect of impact conditions and residual stress

The present scraping test provides an interfacial adhesion strength between solidified paraffin splats and metal substrates. It is expected that the measured scraping forces are related to the interfacial adhesion strength, and can be employed to examine the influences of various impact conditions. However, as shown in Fig. 3.3 the splat geometry

changes with droplet impact conditions. It indicates that the measured scraping forces under various conditions cannot be compared directly since the splat geometry intrinsically affects the scraping forces.

To eliminate the effect of splat geometry, Merchant's model of orthogonal cutting is considered [100, 101]. In the model, the tangential cutting force can be written as follow:

$$F_c = K_c wh\,, \tag{4.1}$$

where w is the width of cut and h is the depth of cut. K_c is the tangential cutting force coefficient. Even though K_c might be affected by many factors including depth of cut, a lot of experimental and theoretical studies [99, 102-104] have suggested that the measured cutting force (F_c) presents an almost linear relationship with depth of cut in orthogonal cutting. Murakawa et al. [57] have examined the effect of coating thickness when evaluating the interfacial adhesion strength using a scraping method. It was found that the measured forces increase almost linearly with the coating thickness even though the adhesion strength is kept constant.

Because the splat geometry (see Fig. 3.3) and scraping behaviors (see Fig. 4.2) are affected by the impact conditions, to eliminate these effects, a parameter $K(d)$ is defined to evaluate the adhesion strength as

$$K(d) = \frac{F(d)}{b(d)\cdot t(d)} = \frac{\text{Scraping force}}{\text{Scraping breadth} \times \text{Splat thickness}}\,. \tag{4.2}$$

Here, $K(d)$ is calculated from the real-time scraping force, $F(d)$, splat thickness, $t(d)$, and scraping breadth, $b(d)$ as a function of scraping displacement, d. The scraping breadth $b(d)$ and splat thickness $t(d)$ are determined by splat profiles and displacement-force curves shown in Fig. 3.3 and Fig. 4.3, respectively. To confirm the reliability of Eq. 4.2, the calculated $K(d)$ and the measured scraping forces are plotted as a function of scraping

displacement in Fig. 4.4 for scraping tests (1) and (7), which indicate low residual stress

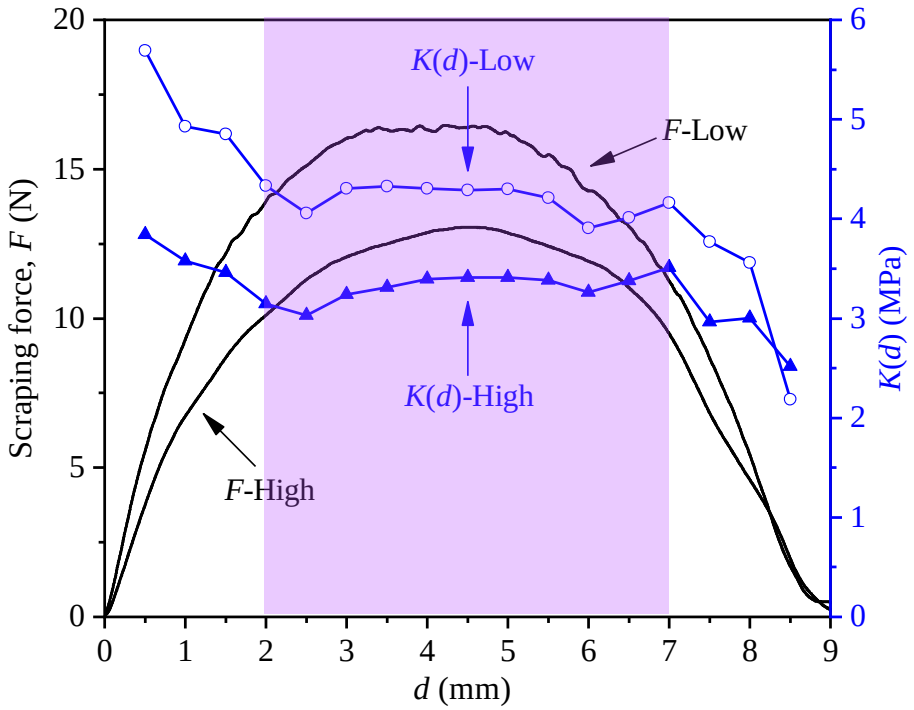

Fig. 4.4 Calculated $K(d)$ as well as measured scraping forces as a function of scraping displacement under low residual stress condition and high residual stress condition for scraping tests (1) and (7), respectively.

condition and high residual stress condition, respectively. In Fig. 4.4, $K(d)$ for low residual stress condition is always higher than that of high residual stress condition. The values of $K(d)$ are almost constant in the highlighted area when the scraping displacements are between 2 mm and 7 mm. It becomes unstable at the splat peripheries due to the rapid changes in splat thickness, scraping breadth, and scraping force. In this study, the value of $K(d)$ at the maximum scraping force, which is always achieved at a scraping displacement between 2 mm and 7 mm, was defined as K_0 to evaluate the interfacial adhesion strength:

$$K_0 = \frac{F_{\max}}{b \cdot t} = \frac{\text{Maximum scraping force}}{\text{Scraping breadth} \times \text{Splat thickness}}. \tag{4.3}$$

The measured maximum scraping forces ($F_{\max}$) and calculated K_0 are summarized in Fig.

4.5 to consider the effects of (a) substrate pre-set temperature, (b) drop height, and (c) droplet temperature, where the drop test conditions are identical with those in Fig. 4.3(a)-(c). It can be seen from Fig. 4.5(a)-(c) that the maximum scraping forces F_{max} seem not influenced by test conditions. Nevertheless, values of K_0, which eliminates the effect of splat geometry, become larger at a higher substrate pre-set temperature, a higher drop height, and a higher droplet temperature. Since larger K_0 corresponds to higher adhesion strength, the scraping test results of K_0 agree well with the debonding behaviors as revealed in Fig. 3.13 and Fig. 3.15, where the debonding is prone to occur under those conditions with smaller K_0. The effect of residual stress on K_0 is shown in Fig. 4.5(d), where the K_0 values for low residual stress and high residual stress conditions are compared. Smaller K_0 values are obtained for high residual stress splats because the high

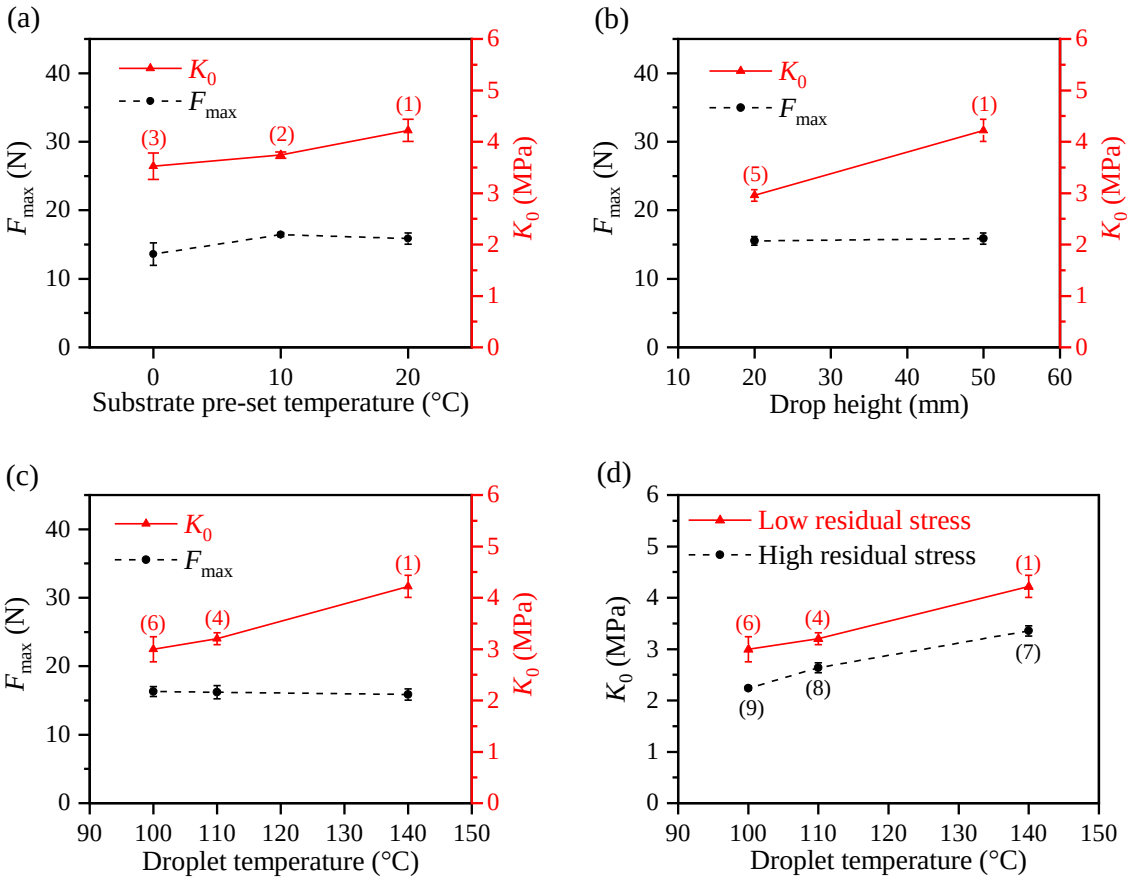

Fig. 4.5 Summary of the maximum scraping forces (F_{max}) and calculated K_0 with considerations of the effects of (a) substrate pre-set temperature, (b) drop height, and (c) droplet temperature, where the drop test conditions are identical with those in Fig. 4.3(a)-(c). (d) Effect of residual stress on K_0.

residual tensile stress facilitated the cracking to propagate along the interface and reduced the forces required to scrap off the splats.

4.4.1 Effect of substrate pre-set temperature

Scraping test results of maximum scraping forces and magnitudes of K_0 under various substrate pre-set temperatures are plotted in Fig. 4.5(a) when the drop height was 50 mm and droplet temperature was 140 °C. It can be seen that the K_0 values monotonically increase with the substrate pre-set temperatures. It explains the phenomenon that splats are more likely to debond at lower substrate pre-set temperatures during the drop tests as discussed in the previous paragraph. At a substrate pre-set temperature of 0 °C, the abrupt reduction of scraping forces is observed as shown in Fig. 4.3(a). This is caused by a weak interfacial adhesion strength which is overcome by the scraping forces during the scraping processes.

4.4.2 Effect of drop height

Maximum scraping forces and values of K_0 are plotted in Fig. 4.5(b), where the drop heights were 20 mm and 50 mm fixing the substrate pre-set temperature at 20 °C and droplet temperature at 140 °C. The values of K_0 are larger for drop height of 50 mm owing to the higher impact velocity to form stronger interfacial adhesion, which is in good accordance with the results of drop experiment.

4.4.3 Effect of droplet temperature

Fig. 4.5(c) presents the effect of droplet temperature on the maximum scraping forces and K_0 values when substrate pre-set temperature was 20 °C and drop height was 50 mm. The K_0 values increase with droplet temperatures. It can be found in Fig. 4.3(c) that the removal of splats occurs earlier as the droplet temperature decreases. It agrees well with drop experiment results, where the lower droplet temperatures facilitated debonding of splats.

In summary, by investigating the K_0 values under various drop experiment conditions, the results of scraping tests showed good agreement with debonding behaviors observed in the drop experiments. That is, the smaller K_0 values were obtained for the conditions when debonding occurred more easily.

4.4.4 Effect of residual stress

Accurate investigation for the effect of residual stress on interfacial adhesion strength of thermal sprayed coatings has been a tough work because the change of residual stress always is associated with the simultaneous changes in many other factors such as coating thickness, Young's modulus, and porosity. In this scraping test, the residual stress in splats can be independently controlled by the stress relaxation of splats without any changes in other factors. The residual stress, therefore, is the only variable to affect the interfacial adhesion strength.

The measured scraping forces under low and high residual stresses are plotted in Fig. 4.3(c) and (d), respectively for various droplet temperatures, fixing the substrate pre-set temperature at 20 °C and drop height at 50 mm. At droplet temperature of 140 °C, the removal of splats does not occur in either high residual stress or low residual stress condition. The maximum value and increasing rate of scraping forces for low residual stress conditions are higher than those for high residual stress conditions. This is because the high residual tensile stress facilitates the cracking along the interface. Test results for 110 °C show that the removal of splat occurs in the low residual stress condition. The removal, however, does not appear for high residual stress conditions because the higher residual tensile stress reduces the magnitude of scraping forces so that it does not reach the critical values to remove the splats from the substrate. As shown in Fig. 4.3(c), when droplet temperature reduces from 110 °C to 100 °C, the removal of splats occurs at smaller displacements. This is caused by the weaker interfacial adhesion at lower droplet temperature.

Fig. 4.5(d) compares the calculated K_0 for high and low residual stress conditions under

various droplet temperatures. The K_0 values for low residual stress condition are always larger than high residual stress condition. As has been discussed above, this result is caused by the residual tensile stress which slows down the increasing rate of scraping forces. Quantification for the effect of residual stress on interfacial adhesion strength is a rather difficult task because of the complex mechanisms of fracture behaviors and stress generation/relaxation processes during the scraping tests. Further study is required towards a better and in-depth understanding of the relationship between residual stress level and interfacial adhesion strength.

4.5 Summary

The adhesion strength of solidified splat was evaluated by conducting a scraping test under various drop impact conditions. The measured maximum scraping force was divided by the produce of blade breadth and splat thickness to quantify the adhesion strength. The main results are summarized as follows.

- A parameter, K_0 which eliminates the effect of splat geometry was defined and measured by a scraping method to evaluate the adhesion strength of solidified splat under various conditions.
- Smaller K_0 values were measured at lower substrate pre-set temperatures, lower drop heights, and lower droplet temperatures. These tendencies successfully explained the debonding behaviors during drop experiment.
- The level of residual tensile stresses in splats was controlled by stress relaxation treatment to examine its effect on the adhesion strength. The scraping test results suggested that the residual stresses facilitated the cracking to propagate along the interface, thereby reducing the measured scraping forces.

Chapter 5
Elastic FEM simulation to evaluate cracking and debonding

5.1 Model description for elastic FEM simulation

The residual strains measured by the strain gauge at the substrate back surface were influenced by the substrate pre-set temperature, drop height, droplet temperature, and paraffin wax materials. In this chapter, the stress distribution in splat/substrate structure is numerically analyzed based on the experimentally measured residual strains. And the cracking and debonding behaviors are evaluated considering the effects of several experimental conditions.

The stress distribution in a splat should be mainly determined by (a) Young's modulus of the splat and substrate, (b) thermal expansion coefficient of the splat, (c) temperature reduction of the splat from the stress-free temperature, T_{sf} (the specific temperature below the melting point) to the equilibrium temperature (substrate pre-set temperature), and (d) the geometries of the splat and substrate. To consider these four factors, the FEM analysis was performed using the commercial finite element code Abaqus/standard 2017.

Elastic analyses were conducted using axisymmetric models designed according to the measured splat geometries (see Fig. 3.3). Figure 5.1 shows an example of FEM model when the substrate pre-set temperature was 20 °C, drop height was 50 mm, droplet temperature was 140 °C, and paraffin material was HNP-9. Here, the measured splat profile was simplified as a trapezoid as shown in Fig. 3.2(b). In the model, the splat touches the center of substrate surface and they share nodes along the interface. The origin of the model is located at the center of the substrate back surface. The *r*- and *z*-axes are

along the radial and thickness directions, respectively. A refined mesh with a minimum size of 10 μm was applied along the interface, especially near the free edge, which is enlarged in Fig. 5.1. A mesh sensitivity study has been performed to confirm that the FEA results are independent of mesh size as long as the mesh is finer than those in Fig. 5.1.

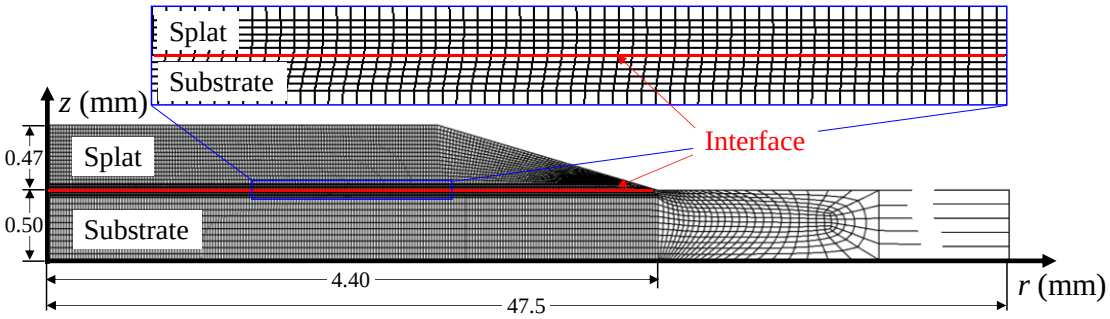

Fig. 5.1 An example of the axisymmetric finite element model when the paraffin material was HNP-9; substrate pre-set temperature was 20 °C; drop height was 50 mm; and droplet temperature was 140 °C. Fine mesh with the smallest size of 10 μm is distributed near the interface.

Material properties used in the FEM analysis were shown in Table 2.1 and Fig. 2.5. Young's modulus E and Poisson's ratio ν of 430 stainless steel substrate were set as E = 200 GPa and ν = 0.3, respectively [105]. As for the paraffin splats, Young's moduli were determined by the experimental results measured by the four-point bending test as a function of testing temperature (see Fig. 2.5). Thermal expansion coefficients were the measured values listed in Table 2.1.

5.2 Simplification of actual stress development process

The main purpose of this FEM analysis is to acquire the actual stress distribution in the splat using the measured splat geometries, and thereby evaluate the cracking and debonding behaviors. However, there are some analytical hurdles to accurately obtain the stress state in the splat by FEM analysis due to complicated mechanisms of stress development during the impact, adhesion, solidification, and cooling processes.

Especially, determination of the stress-free temperature (T_{sf}), and evaluation of the stress relaxation due to creep deformation and imperfect interfacial bonding is difficult. To simplify these problems, several assumptions are given in this chapter as follows:

1) Substrate temperature is kept constant at the substrate pre-set temperature (T_{sub}) during the analysis. Temperature evolution of the substrate due to the thermal conduction from the splat is neglected because the effect of temperature distribution in substrate on the residual strain is appropriately compensated and the transient evolution rapidly settles in the experiment.

2) The splat stress starts to accumulate at the stress-free temperature T_{sf} ($< T_m$). Although T_{sf} cannot be measured experimentally, it can be determined using assumption 4) and the measured residual strain (ε_r).

3) Elastic deformation occurs in the splat/substrate bi-layer structure due to thermal shrinkage of the splat. The magnitudes of stress and strain are proportional to the temperature reduction of splat from T_{sf} to T_{sub} ($\Delta T = T_{sf} - T_{sub}$). Thus, the residual strain (ε_r) at the substrate back surface is proportional to the temperature reduction, as

$$\varepsilon_r(T) = k \cdot \Delta T = k \cdot \left(T_{sf} - T_{sub}\right), \tag{5.1}$$

where constant k is a function of the material properties and geometries of the splats. Plastic and creep deformation are not considered.

4) Deformation of the bi-layer structure reaches equilibrium when the splat temperature decreases to T_{sub}. Numerical residual strain at this time should be identical to the residual strain measured in the experiments (ε_r). In other words, the stress-free temperature T_{sf} is determined so that the computed residual strain is identical to the measured value.

For an accurate simulation to reproduce the actual phenomena, including solidification and cooling, detailed information of the stress-free temperature T_{sf} in assumption 2) and the creep deformation neglected in assumption 3) are required. However, there is a linear relationship between the splat stress and the residual strain at the substrate back surface, even though the stress development during the actual process includes several complicated and unknown parameters. The splat stress can be evaluated based on the measured value of residual strain at the substrate back surface as far as the equilibrium condition is considered.

To determine the values of k in assumption 3), the residual strain was calculated considering the case where the temperature of the splat is cooled down from (T_{sub} + 1 °C) to T_{sub}. In this chapter, several analyses are performed for simulating the experimental conditions as summarized in Table 5.1. A total of 11 simulation results are employed to

Table 5.1 Simulated experimental conditions by elastic finite element analysis.

Drop impact conditions											
Paraffin wax material	candle wax					HNP-9					
Substrate pre-set temperature, T_{sub} (°C)	20	15	10	5	0	20	15	10	5	0	0
Drop height, H (mm)	100	100	100	100	100	100	100	100	100	100	200
Droplet temperature T_{drop} (°C)	140	140	140	140	140	140	140	140	140	140	140
Simulations used to evaluate:											
Radial stress of candle wax (Fig. 5.2(a))	×	×	×	×	×						
Radial stress of HNP-9 (Fig. 5.2(b))						×	×	×	×	×	
Interfacial stresses: effect of T_{sub} (Fig. 5.6)						●		●		●	
Interfacial stresses: effect of H (Fig. 5.8)										●	●

evaluate specific stress components as shown in the table.

5.3 Radial stress in splat as a driving force for cracking behavior

Figure 5.2 shows the normal stress along the radial direction (σ_{rr}) at the center of the splat (r=0) calculated for (a) candle wax and (b) HNP-9. Here, the substrate pre-set temperatures are changed from 0 °C to 20 °C at the drop height of 100 mm. As mentioned in Sec. 5.2, the FEM models were individually designed according to the measured splat geometry for each experimental condition. For comparison, the measured tensile strength of candle wax and HNP-9 are plotted with respect to the testing temperature. For candle wax (Fig. 5.2(a)), the splat stress increases with the reduction of substrate pre-set temperature and decreases with the appearance of cracking at substrate temperatures lower than 10 °C. Comparing the calculated splat stresses with the tensile strength, the splat stress increases close to the tensile strength at 15 ºC and might exceed it at a temperature between 10 °C and 15 °C. These results agree well with the experimental results, in which cracking was observed below 10 °C. In HNP-9 (Fig. 5.2(b)), the splat

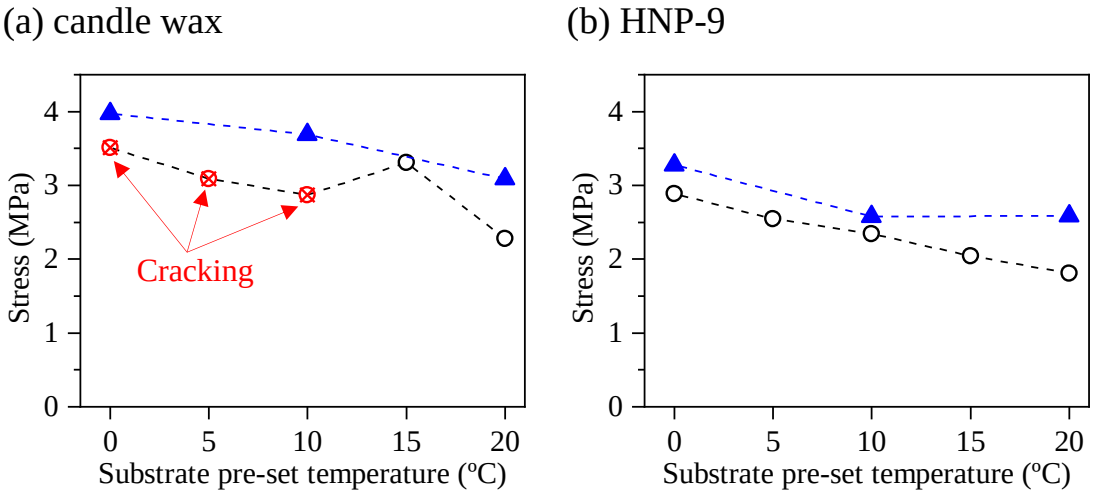

Fig. 5.2 Splat stress (σ_{rr}) and tensile strength for (a) candle wax and (b) HNP-9 with changing substrate pre-set temperatures, from 0 °C to 20 °C, at drop height of 100 mm, droplet temperature of 140 °C.

stress increases with the reduction of substrate pre-set temperature. However, the stress never exceeds the tensile strength at any substrate temperatures. Actually, as discussed in Sec. 3.5, no cracking was observed in the experiments for HNP-9. Therefore, it can be concluded that the FEM analysis provides reasonable explanations for the cracking behavior for both the candle wax and HNP-9, even though it includes several significant approximations relying on the measured residual strains at the equilibrium condition.

5.4 Interfacial stresses as driving forces in the debonding behavior

Interfacial stresses including peeling stress and shear stress are main driving forces for debonding behaviors. In order to clarify the mechanisms of fractures in layered structures, many efforts have been made to calculate the distribution of interfacial stresses. On the basis of Timoshenko's theory [88], Suhir [106] obtained a solution to interfacial stresses due to thermal mismatch in a tri-layer structure with same length of each layer. Based on the analytical solution, calculation results of shearing stress and peeling stress by using a numerical example are shown in Fig. 5.3 and Fig. 5.4, in which, $\tau_1(x)$, $p_1(x)$, and $\tau_2(x)$, $p_2(x)$ are stress distribution along upper and lower interface, respectively. Calculated results demonstrated that both peeling stress and shearing stress reach the largest value at the free edge and decrease rapidly away from the free edge.

Some efforts have been made to obtain the interfacial stresses when the layers have different lengths. Yin et al. [107] have tried to solve interfacial stresses in a layered structure with a stepped edge in which both plane-stress and plane-strain conditions were considered. On the basis of Yin's method, Feng et al. [108] introduced a solution to the interfacial stress of a chip-substrate system in which the model and boundary condition are highly similar to the droplet/substrate structure in this dissertation. In this structure, interfacial thermal stresses were generated by thermal expansion mismatch during the heat transfer from chip into substrate. The comparison of analytical (PM) and FEM results of interfacial stresses are shown in Fig. 5.5. In the FEM calculation, due to stress

singularity, stress reached a rather large value near the 90 ° free edge. Yet, in the case of analytical solution, stress at the edge of the chip was assumed to be zero as a boundary condition, and a largest value was located at the position near the free edge.

To evaluate the debonding behavior in the experiments for the HNP-9, σ_{zz} and τ_{rz} along the splat/substrate interface are calculated. Here, σ_{zz} and τ_{rz} refer to peeling stress and

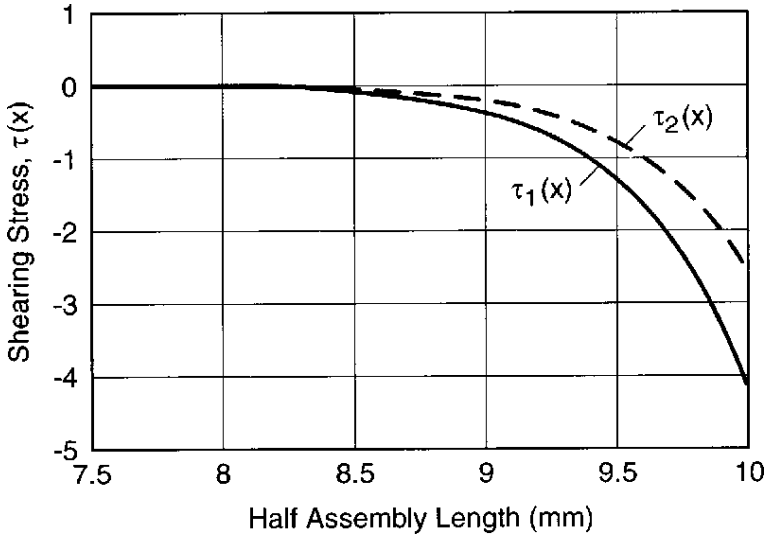

Fig. 5.3 Interfacial shearing stresses (kgf/mm^2) as a function of the distance from the middle of the layered structures. Adapted from [106].

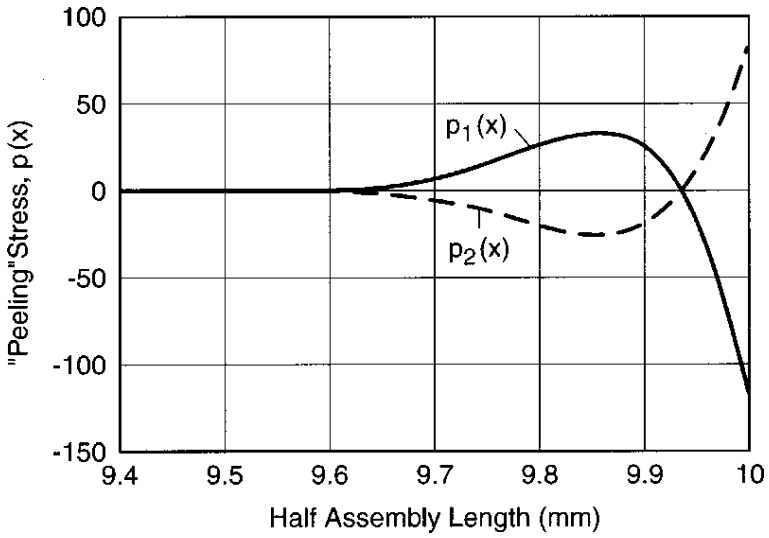

Fig. 5.4 Interfacial peeling stresses (kgf/mm^2) as a function of the distance from the middle of the layered structures. Adapted from [106].

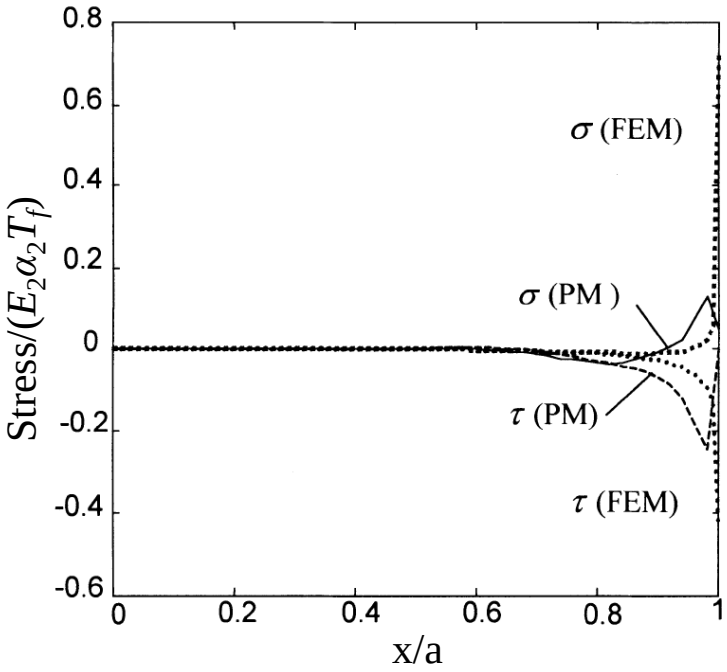

Fig. 5.5 Comparison of peeling stress and shear stresses between analytical and FEM solutions as a function of the distance away from origin of the coordinate system. Adapted from [108].

shear stress, respectively, which are the main driving forces for debonding at the splat/substrate interface.

5.4.1 Effect of substrate pre-set temperature

To consider the effect of substrate pre-set temperature, interfacial stresses are calculated for HNP-9 splats with different pre-set temperatures of 0 °C, 10 °C, and 20 °C when the drop height was 100 mm and droplet temperature was 140 °C. Calculated distributions of σ_{zz} and τ_{rz} along the interface are shown in Fig. 5.6(a) and (b), respectively. As the debonding always initiates from the free edge of the splat and propagates into the interior along the interface, stress distribution near the free edge should be mainly noticed. In this figure, the peeling stress σ_{zz} is tensile near the free edge and changes to compressive at $r \approx 4.5$ mm. This compressive stress, which becomes maximum at $r \approx 4$ mm, is due to the bending moment induced by the thermal shrinkage of the splat. Similarly, the shear stress along the interface τ_{rz} shows the maximum value at the free edge and decreases towards

the center of the model. These stress distributions along the interface are very similar to the numerical investigations for layered structures [108, 109], except that there is no stress singularity in the computed σ_{zz} and τ_{rz} in Fig. 5.6. This is because the contact angle of the present FEM model is much smaller than 90 °. It is also found in Fig. 5.6 that both σ_{zz} and τ_{rz} at the free edge become larger with the reduction of temperature. The magnitudes of

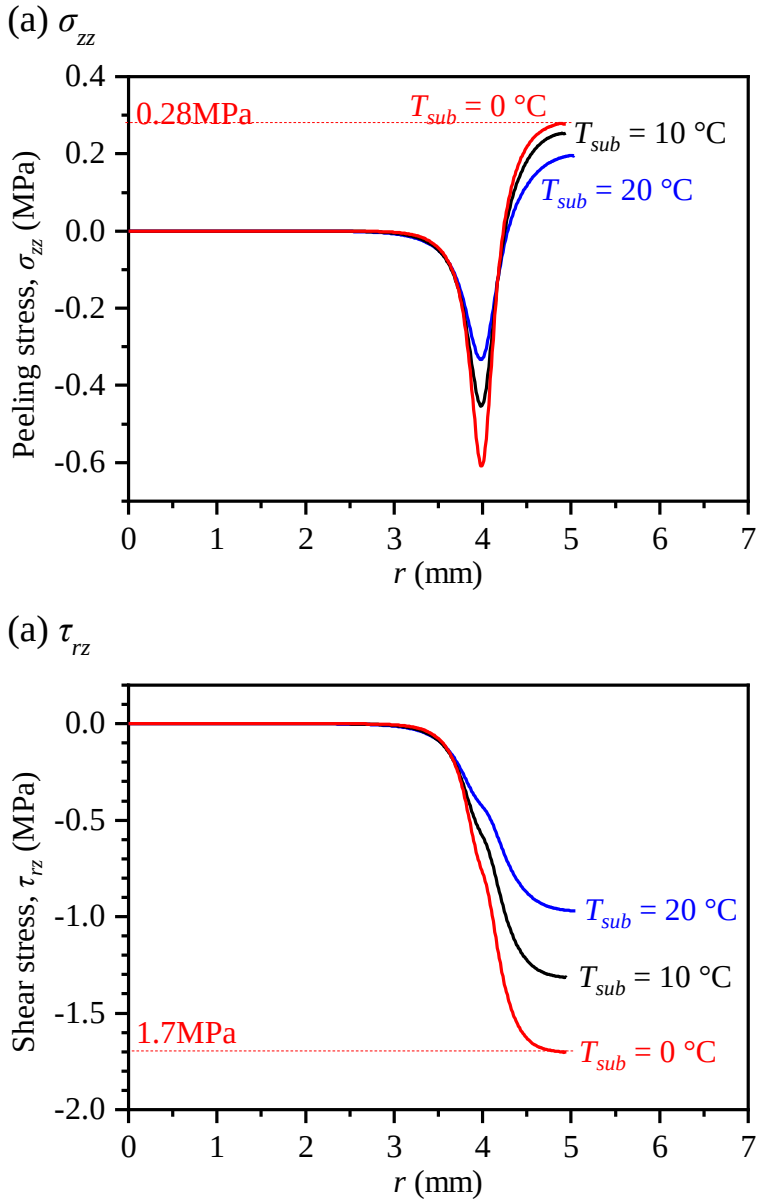

Fig. 5.6 FEM results for (a) peeling stress (σ_{zz}) and (b) shear stress (τ_{rz}) distribution along the interface at the substrate pre-set temperatures of 0 °C, 10 °C, and 20 °C, droplet temperature of 140 °C, drop height of 100 mm, and paraffin of HNP-9.

σ_{zz} and τ_{rz} at the substrate temperature of 0 °C are σ_{zz} = 0.28 MPa and τ_{rz} = 1.7 MPa, respectively. These values might be critical stress conditions that induce debonding between HNP-9 splat and stainless substrate, because no debonding was observed when the substrate temperature was higher than 0 °C as shown in Fig. 5.7.

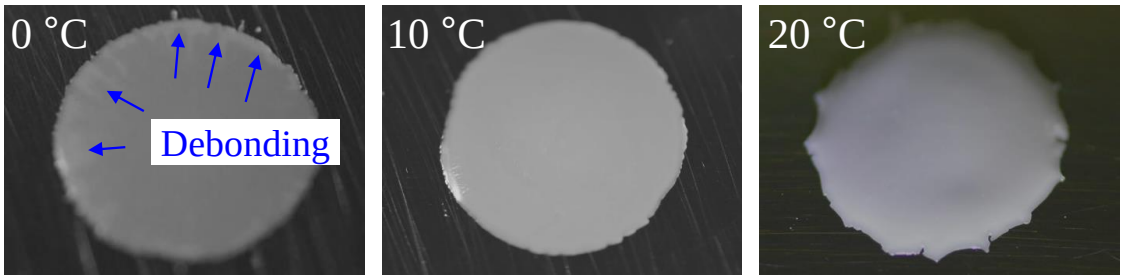

Fig. 5.7 Photos of solidified HNP-9 splats under each substrate pre-set temperature. The other experimental conditions are same with Fig. 5.6. Debonding is indicated by a blue arrow at 0 °C.

5.4.2 Effect of drop height

Effect of drop height on the debonding of HNP-9 splat is investigated by calculating the interfacial stresses at drop heights of 100 mm and 200 mm when the substrate pre-set temperature was 0 °C, and droplet temperature was 140 °C. Calculated distributions of σ_{zz} and τ_{rz} along the interface are shown in Fig. 5.8(a) and (b), respectively. Distributions of σ_{zz} and τ_{rz} have a same manner with those shown in Fig. 5.6. The magnitudes of both peeling and shear stresses at the splat edges are larger in the drop height of 100 mm. It is owing to the thicker splat (see Fig. 3.3(b)) formed at the lower drop height, which induces larger bending moment and larger stresses at the interface as discussed in Sec. 3.4. The calculation results show good agreement with the results of drop experiments in which the debonding is more likely to occur at lower drop heights as shown in Fig. 3.15.

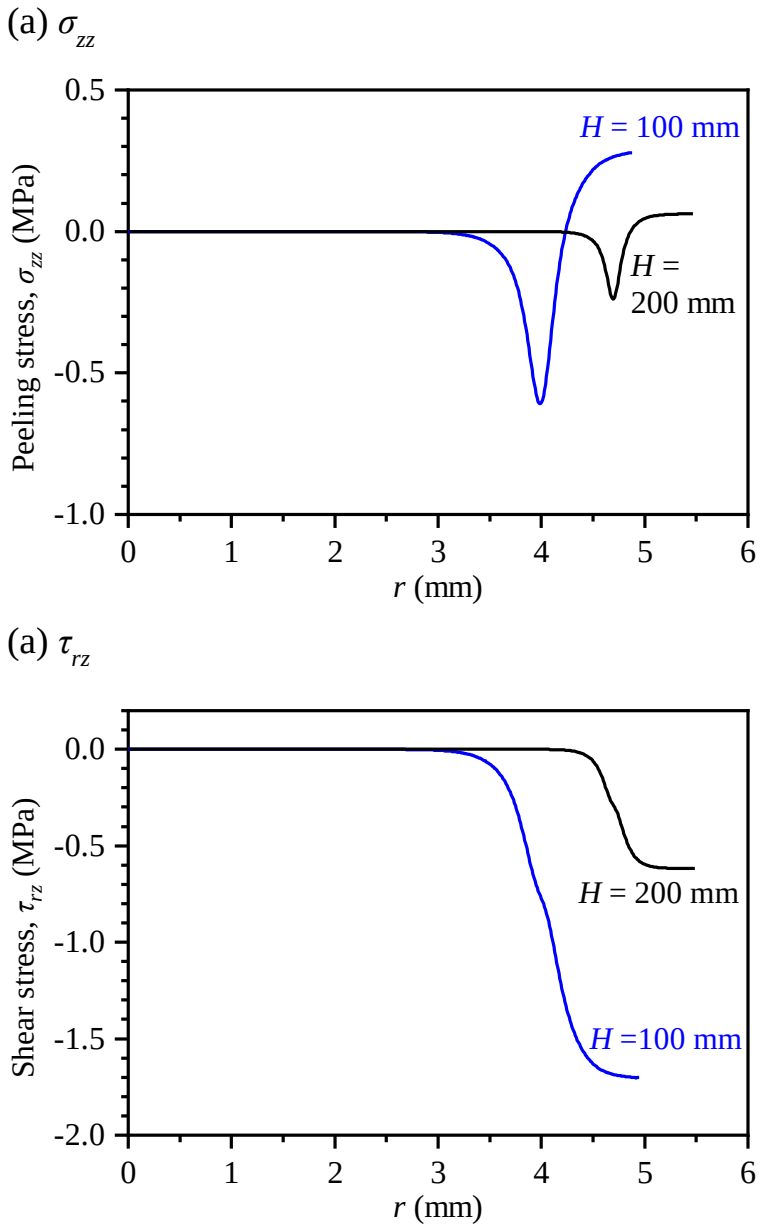

Fig. 5.8 FEM results for (a) peeling stress (σ_{zz}) and (b) shear stress (τ_{rz}) distribution along the interface at drop heights of 100 mm and 200 mm, droplet temperature of 140 °C, and substrate pre-set temperatures of 0 °C.

5.5 Summary

Elastic finite element analysis was performed to calculate the stress distributions in splat/substrate structure; they are splat stress in radial direction and interfacial stresses along the interface. Cracking and debonding, and the effects of several experimental conditions were fully discussed according to simulation results. Conclusions are summarized as follows.

- Splat stress increased with the reduction of substrate pre-set temperature. Cracking occurred in the candle wax splat when the substrate pre-set temperature was below 10 °C due to increased splat stress that might exceed the tensile strength of paraffin wax. While cracking was never observed in HNP-9 splats since the residual stress never exceeded its tensile strength.
- Simulation results indicated that larger peeling stresses and shear stresses are generated at lower droplet temperature and lower drop height. It explains the debonding behaviors observed in the drop experiment well.

Chapter 6
Coupled thermo-mechanical simulation to evaluate residual strain

6.1 Finite element model

Coupled thermo-mechanical analysis is performed to calculate the evolution of residual strain in association with the thermal conduction between splat/substrate during the drop experiment. The applied mesh is the same as that used in the elastic analysis in Fig. 5.1, and the eight nodes axisymmetric thermally coupled quadrilateral elements (CAX8T) are used. The analysis is focused on the thermal conduction between splat and substrate, as well as the resultant residual strain evolution. In the analysis, the temperatures of substrate and splat before calculation are set as substrate pre-set temperature and droplet initial temperature, respectively. Thermal conduction between substrate and splat is calculated by using the thermal properties as summarized in Table 2.1. What should be noted is that the thermal expansion coefficient of the substrate was set as zero to avoid a computational difficulty related to a steep temperature gradient across the interface; that is, although the thermal expansion of the substrate could not be reproduced during the calculation, the stress distribution in the splat could still be correctly obtained. This is because the substrate temperature was kept constant during the experiments except during the transient heat transfer just after the impact. Heat transfer between splat/substrate structure and surrounding atmosphere is also considered. The heat transfer coefficient is assumed as 5 $W/(m^2 \cdot K)$ as the atmosphere is the static air in the experiment [110].

The material properties applied in this analysis are basically same with those in Chapter 5. Several additional parameters are used because thermal conduction is considered in the coupled thermo-mechanical analysis. In particular, temperature dependent Young's

modulus (see Fig. 2.5) of paraffin wax materials are used. It should be noted that 60 °C and 45 °C are assumed to be the stress-free temperature, T_{sf} (Young's modulus is nearly zero) of HNP-9 and candle wax, respectively. During the cooling process of splat, stress starts to generate at these temperatures. To ensure a stress-free state at the temperature above the stress-free temperature, a reference temperature of thermal expansion coefficient is set identical to the stress-free temperature of each paraffin [87]. To ensure convergence, Young's modulus at the melting point was set as a very small value of 0.1 MPa. Specific heat and thermal conductivity coefficient of SUS430 stainless steel substrate are set at 460 J/(kg·K) and 26.4 W/(m·K), respectively [105].

Drop impact conditions to be performed in this Chapter are summarized in Table 6.1. A total of four conditions are performed to calculate the evolution of residual strain and substrate temperature, and effect of experimental conditions on interfacial adhesion which will be discussed later.

Table 6.1 Simulated experimental conditions by coupled thermo-mechanical analysis.

Drop impact conditions				
Paraffin material	candle wax	HNP-9		
Substrate pre-set temperature (°C)	20	20	20	20
Drop height (mm)	50	50	50	100
Droplet initial temperature (°C)	140	140	80	140
Simulations used to evaluate:				
Substrate temperature (Fig. 6.1, Fig. 6.2)		○		
Residual strain evolution (Fig. 6.3, Fig. 6.5)	○	○		
Effect of paraffin material on *E*/*N* (Fig. 6.6)	○	○		
Effect of T_{drop} on *E*/*N* (Fig. 6.7)		○	○	
Effect of *H* on *E*/*N* (Fig. 6.8)		○		○

6.2 Evolution of substrate temperature

Figure 6.1 presents a comparison of the temperature evolution of substrate for the experiment and calculation. Here, the experimental substrate temperature was measured by the thermocouple T_1 as shown in Fig. 3.1. Numerical result presents the temperature evolution at the same position. The numerical result for both the heating and cooling rates of the substrate are higher than the experimental result. The highest numerical temperature was also higher than the highest experimental temperature. This result should be attributed to the interfacial thermal resistance at the splat/substrate interface, which was ignored in the analysis. In the actual phenomenon, the effective thermal conductivity of the coating always decreases because of the interfacial thermal resistance [111]. In a TBCs system, temperature reduction always occurs across the interface and is dependent on the degree of imperfection at the interface [112]. However, it can be speculated that this difference in thermal conduction has very limited effect on the stress and strain evolution, because it vanishes in just a few seconds. Figure 6.2 compares numerical

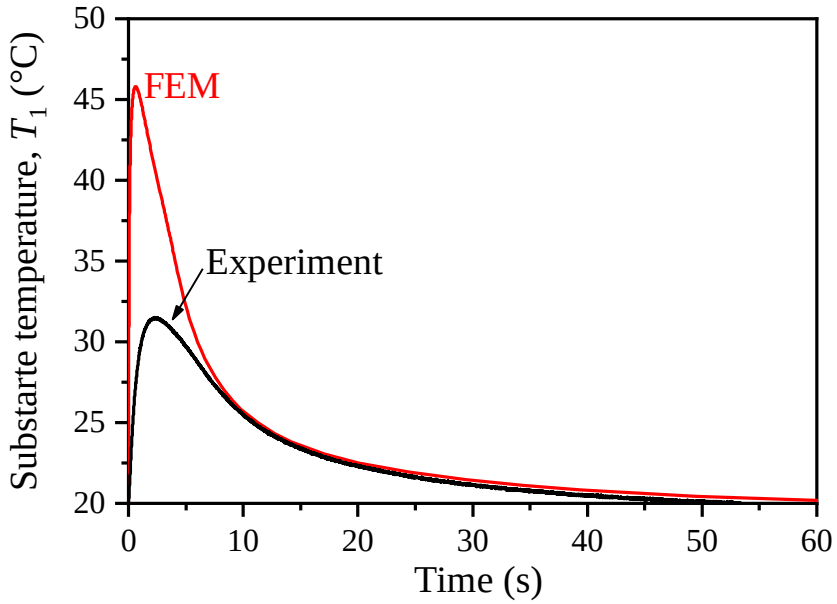

Fig. 6.1 Comparison of experimental and numerical results of substrate temperature variation for HNP-9, with a substrate pre-set temperature of 20 °C, drop height of 50 mm, and droplet temperature of 140 °C.

results of substrate temperature variation at top and bottom surface under same drop impact conditions with Fig. 6.1. Here, the temperature of bottom surface is same with that in Fig. 6.1, while the temperature of top surface refers to the temperature of substrate top surface just above thermocouple T_1. It is found the temperature gap between top and bottom surface only exists during the beginning 0.1 second. More detailed discussion of the thermal conduction issues is beyond the scope of this dissertation.

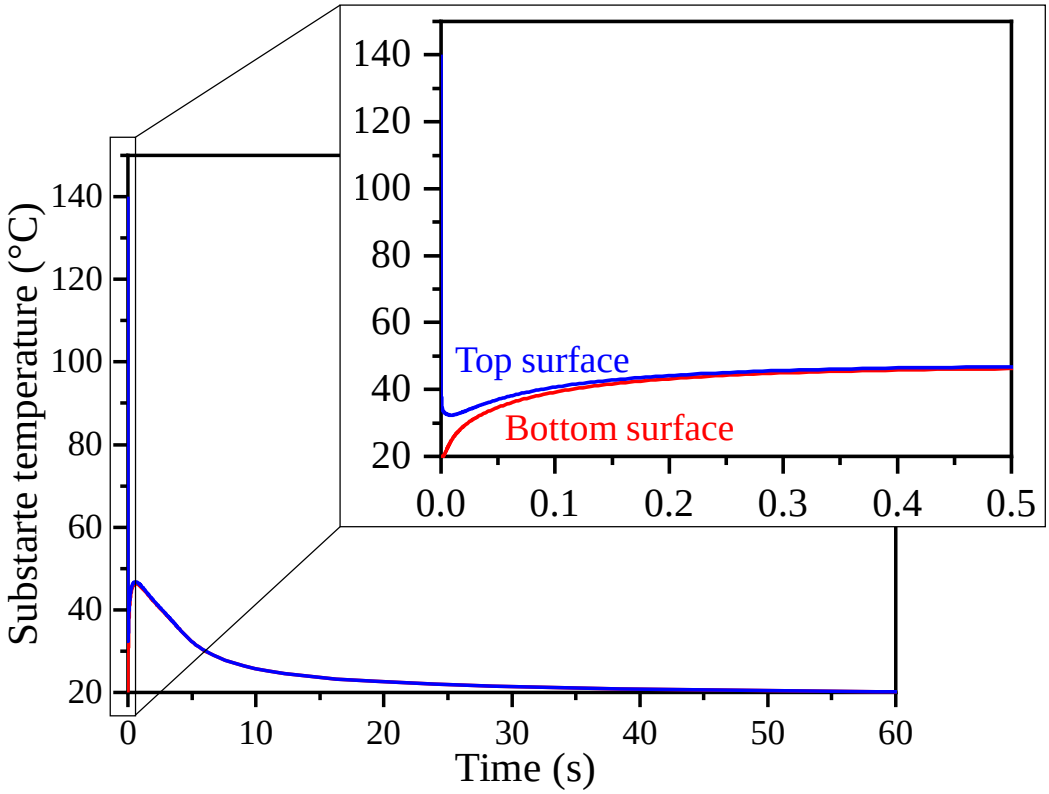

Fig. 6.2 Numerical results of substrate temperature variation at top and bottom surface. Drop impact condition is same with Fig. 6.1.

6.3 Evolution of residual strain ignoring creep

Evolution of residual strain during drop experiment was calculated for candle wax and HNP-9 when substrate pre-set temperature was 20 °C, drop height was 50 mm, and droplet temperature was 140 °C, as shown in Table 6.1. Calculation results are compared

with experimental measurements in Fig. 6.3 for (a) HNP-9 and (b) candle wax. The black plots show the experimentally measured results, in which a compressive residual strain is measured immediately after the impact. This negative value is caused by the thermal gradient in substrate due to the transient heat conduction from the splat. However, the substrate temperature reduces to pre-set temperature quickly after the impact, and the thermal strain, therefore, vanished in several seconds.

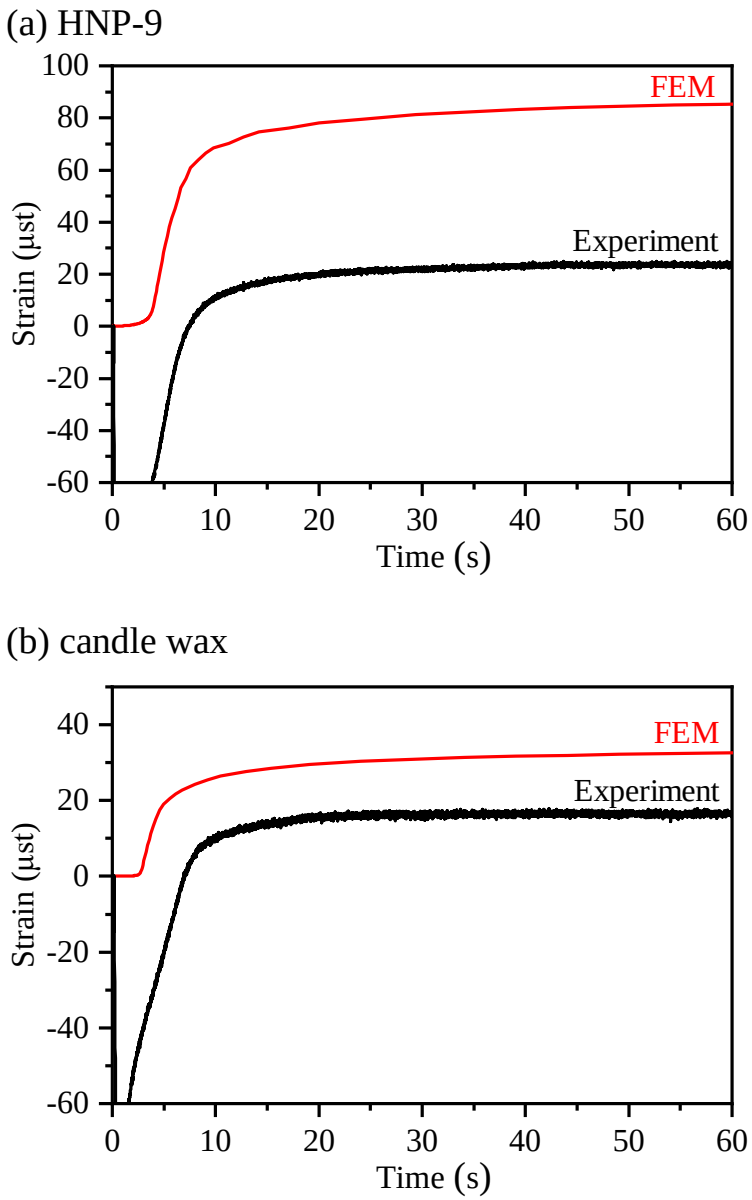

Fig. 6.3 Comparison of experimental results and numerical results of residual strain evolution when substrate pre-set temperature was 20 °C, drop height was 50 mm, and paraffin wax materials were (a) HNP-9 and (b) candle wax.

For both paraffin wax materials, calculated residual strains at steady state are larger than the experimental results. This great difference should be attributed to the creep of splats and imperfect interfacial bonding, which are not considered in the present calculations and will be evaluated in Sec. 6.4 and Sec. 6.5, respectively.

6.4 Effect of creep

The effect of creep of paraffin splat on the evolution of residual strain is evaluated by using a strain-hardening creep model, in which the constants were determined by four-point bending creep tests as described in Sec. 2.3.

6.4.1 Elastic-creep simulation to validate hardening creep model

An elastic-creep analysis is firstly performed to evaluate the validity of the measured creep properties in Sec. 2.3, and to determine an appropriate creep model according to the stress relaxation test in Sec. 3.7. In the analysis, a FE model similar with Fig. 5.1 was employed.

The evolution of residual strain during the stress relaxation test is calculated using a FE model discretized by eight-node axisymmetric elements (CAX8). The analysis is performed in two steps corresponding to two sequential processes during the stress relaxation test: (i) an elastic analysis to reproduce the stress-strain state in splat/substrate structure when the temperature reduces to the substrate pre-set temperature (stable state); and (ii) a creep analysis to compute the residual strain evolution during the constant-temperature holding process using a hardening creep law.

In step (i), an elastic analysis is performed to generate a residual strain that is identical to the measured value at the stable state, namely, to generate an initial condition for the following creep analysis. Here, if actual temperature reduction is applied to the splat,

however, results for residual strain at the stable state should become much larger than the actual experimental results, simply because this analysis ignores creep and other factors. In order to eliminate this discrepancy, a temperature reduction smaller than the actual value is applied to the splat so that a residual strain identical to the experimental result is generated in the model. Detailed procedures of step (i) are same with those in Sec. 5.2.

Evolution of the residual strain during the holding process is computed by a creep analysis in step (ii), during which the splat and substrate temperatures are kept constant at 20 °C. The validity of creep model can be evaluated quantitatively through this analysis, in which creep is the only factor influencing the residual strain. A strain hardening creep law is considered where five sets of creep constants (see Table 2.2, and Table 2.3) at the substrate pre-set temperature (20 °C) are used. The most appropriate creep models are determined by comparing the experimental results with numerical results of residual strain evolutions.

Computed results are compared with experimental results in Fig. 6.4. Here, five kinds of colored curves show calculated results using the strain hardening law, changing fitting conditions as shown in Table 2.2, and Table 2.3. The measured results in the stress relaxation test are represented as the black curve. Table 6.2 summarizes the coefficient of determination (R^2) in five creep models. It can be found in Fig. 6.4 and Table 6.2 that among the five curves of strain hardening law, a creep model determined by the data of 0-10 min shows the best fit to the experimental result for both HNP-9 and candle wax. Therefore, in the following coupled thermo-mechanical analysis, the strain hardening form of power creep law determined by the test data of 0-10 min will be used.

(a) HNP-9

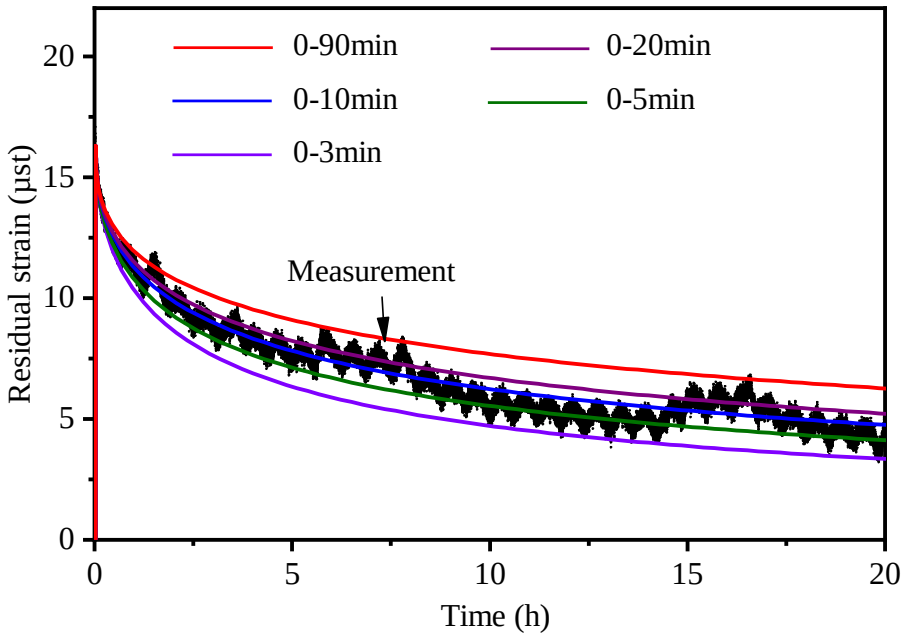

(b) candle wax

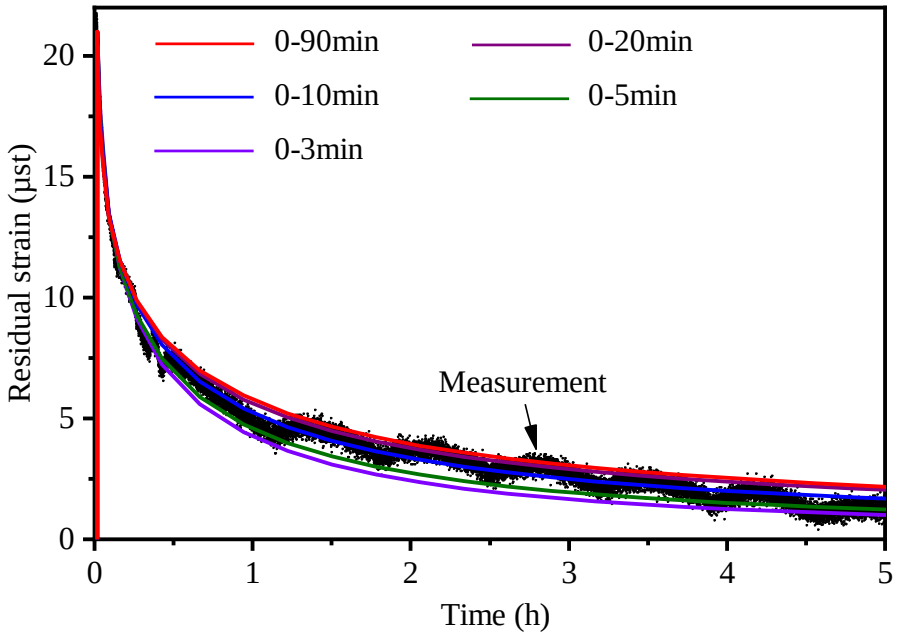

Fig. 6.4 Comparison of experimental and numerical results of residual strain evolutions at a drop height of 100 mm, and substrate pre-set temperature of 20 °C for (a) HNP-9 and (b) candle wax. Five analyses with different creep constants were performed for each material.

Table 6.2 Coefficient of determination (R^2) for the numerical results of residual strain evolution during the stress relaxation test, where the numerical results were viewed as the predicted value and the experimental results were viewed as the modeled value.

	0-3 min	0-5 min	0-10 min	0-20 min	0-90 min
HNP-9	0.872	0.966	0.986	0.966	0.835
candle wax	0.993	0.996	0.997	0.994	0.992

6.4.2 Evolution of residual strain considering creep

The most appropriate creep model for paraffin wax materials, which have been determined in Sec. 6.4.1 is employed in the coupled thermo-mechanical analysis. Considering that the stress in splat changes in association with the cooling process, temperature dependent constants for strain hardening creep model (see Table 2.2, and Table 2.3) are used to consider the temperature dependent creep properties of the splat.

Calculated results are added to Fig. 6.3 and replotted in Fig. 6.5. In Fig. 6.5, when the creep is not considered, numerical results of residual strains at stable state are 3.3 and 2.2 times larger than the experimental results for HNP-9 and candle wax, respectively. When the creep is considered, numerical results decrease to 2.2 and 1.5 times larger than those of experiments with HNP-9 and candle wax, respectively. These results suggested that creep is certainly a critical factor causing the reduction of residual strain. However, there is still a significant gap between experimental results and numerical results with creep for both paraffin waxes, and it must be attributed to other reasons.

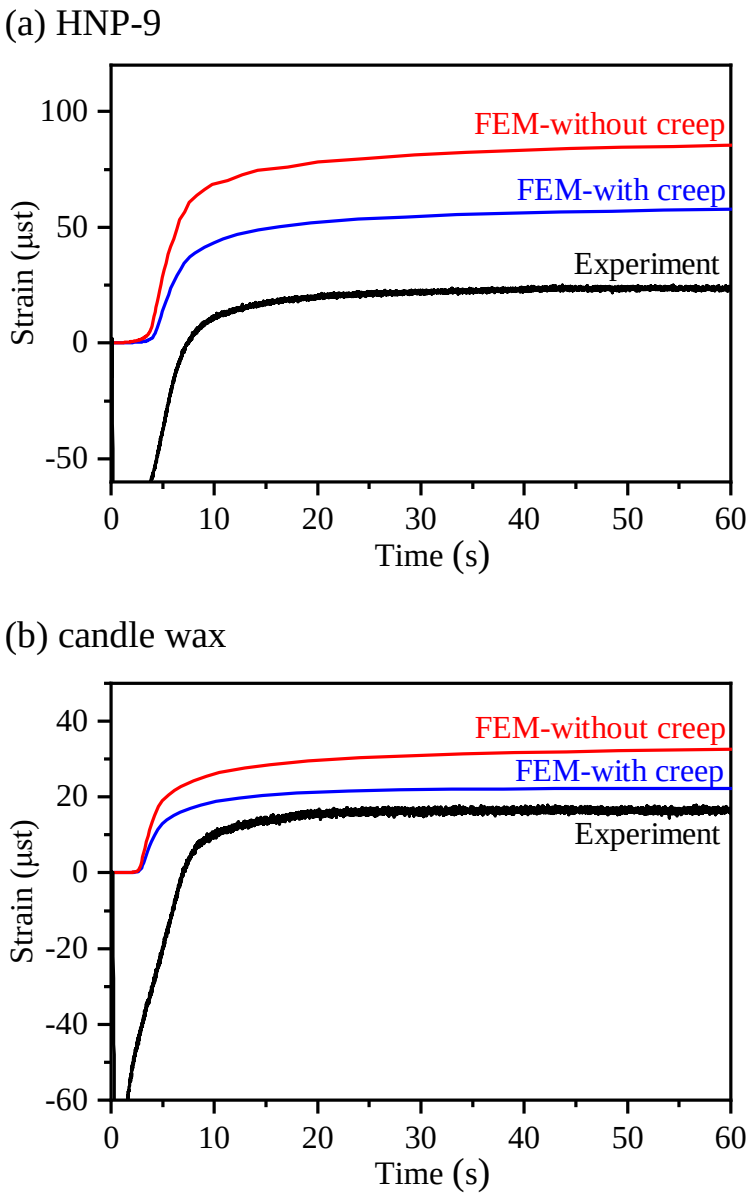

Fig. 6.5 Comparison of experimental results and numerical results of residual strain evolution when substrate pre-set temperature was 20 °C, drop height was 50 mm, droplet temperature was 140 °C, and paraffin materials were (a) HNP-9 and (b) candle wax.

6.5 Effect of interfacial adhesion

Normally, residual stress generated in solidified splat could be partly released by vertical cracking, debonding, creep, and stress relaxation at the interface [37, 113-114]. In this chapter, vertical cracking and debonding did not occur in any experimental condition. Therefore, the only reason for the aforementioned gap of residual strains in Fig. 6.5 should be the stress relaxation at the splat/substrate interface induced by imperfect interfacial bonding. Direct quantitative evaluation of this phenomenon is very hard due to its complicated mechanisms. However, this factor now can be estimated based on the numerical results considering creep.

The coating/substrate interfacial adhesion is affected by a lot of experimental conditions. For example, the temperature and impact velocity of droplet, substrate pre-set temperature, and substrate surface roughness all influence the formation of the coating and hence the interfacial adhesion [115-117]. It is generally accepted that the stress level in the coating decreases when the effective contact area on the coating/substrate interface decreases or the interfacial adhesion becomes weaker. In this section, the effects of three experimental variables: melting point of paraffin wax materials, droplet temperature, and drop height on the splat/substrate interfacial adhesion and residual strains are evaluated by the coupled thermo-mechanical analysis.

A simple and dimensionless parameter (E/N) is introduced to evaluate the effect of interfacial adhesion on residual strain:

$$E/N = \frac{\text{Experimental residual strain}}{\text{Numerical residual strain}}. \tag{6.1}$$

A larger E/N means a better interfacial adhesion and less relaxation of stress-strain at the interface. The effects of aforementioned three experimental variables on interfacial adhesion and residual strains can be evaluated through the magnitudes of parameter E/N.

Many literatures have reported the effects of drop impact conditions on coating stress. For example, experimental results of Zhang et al. [118] suggested that stress in the coating increases with the increase of spraying temperature. Nevertheless, most of the studies have focused on the mechanisms of the whole coating containing numerous splats, and have not distinguished the individual effects of spraying parameters on the single particle behavior. In this chapter, stress-strain evolution of a single splat impacted onto a metal substrate is calculated considering creep. Although further investigation is required to observe the interfacial morphology and clarify the mechanisms of the interfacial adhesion, the effect of splat/substrate interfacial adhesion on residual strain can be evaluated according to the numerical results.

6.5.1 Effect of paraffin's melting point

The melting point of candle wax is about 20°C lower than that of HNP-9 (see Table 2.1). Therefore, the viscosity of candle wax droplet should be lower than that of HNP-9 droplet during their spreading process. Additionally, the candle wax droplet experiences a longer spreading and cooling period until the end of solidification due to a lower melting point. As a result, in the drop experiment with candle wax, the molten droplet spreads and flows more sufficiently on the substrate surface, and therefore inducing a larger effective contact area and higher adhesion strength at the interface. Values of E/N for HNP-9 and candle wax are compared in Fig. 6.6 at the substrate pre-set temperature of 20 °C, drop height of 50 mm, and droplet temperature of 140 °C. The magnitude of E/N for candle wax is 0.21 larger than that of HNP-9. In other words, more stress was relaxed at the interface in HNP-9 due to a poorer interfacial adhesion.

6.5.2 Effect of droplet temperature

Figure 6.7 compares the values of E/N for droplet temperatures of 80 °C and 140 °C at the drop height of 50 mm, substrate pre-set temperature of 20 °C, and paraffin wax material of HNP-9. It is found that E/N becomes larger at elevated droplet temperature which means the degree of stress relaxation at the interface becomes smaller at a higher

droplet temperature. This is because the increase of droplet temperature associated with lower viscosity and longer solidification process, results in easier spread and sink of molten droplet into surface cavities of substrate to form a better bonding at the interface.

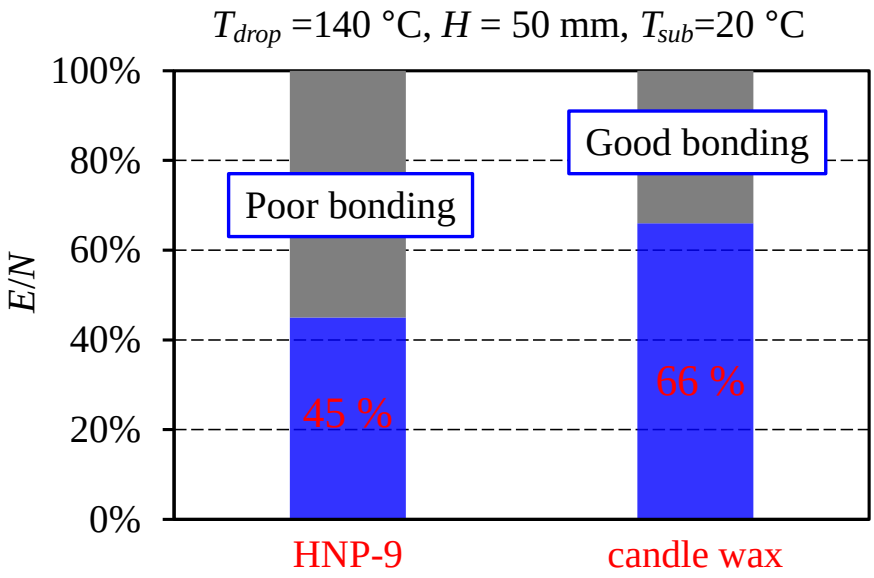

Fig. 6.6 Comparison of values of *E*/*N* for HNP-9 and candle wax at the droplet temperature of 140 °C, drop height of 50 mm, and substrate pre-set temperature of 20 °C.

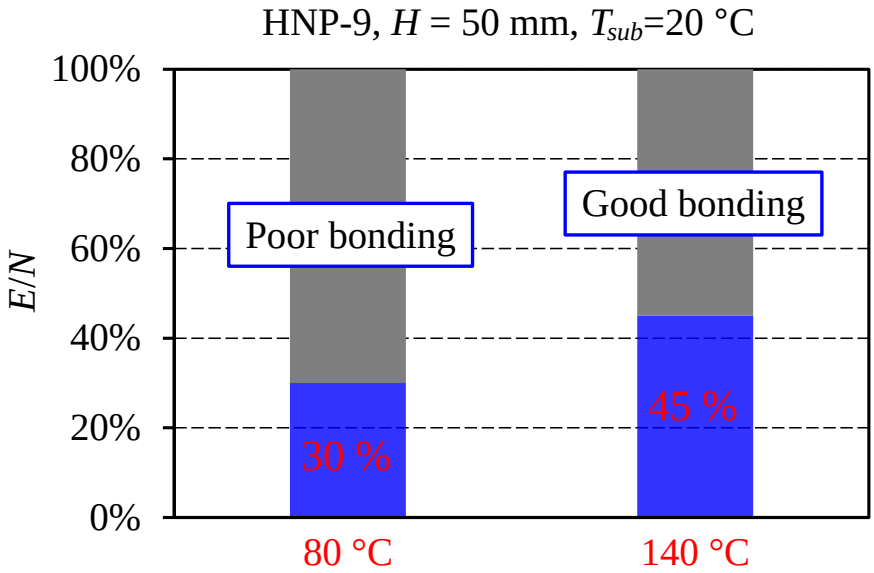

Fig. 6.7 Comparison of values of *E*/*N* for droplet temperatures of 80 °C and 140 °C at the drop height of 50 mm, substrate pre-set temperature of 20 °C, and paraffin wax material of HNP-9.

6.5.3 Effect of drop height

The effect of drop height on *E*/*N* was investigated by performing simulation for drop heights of 50 mm and 100 mm at the droplet temperature of 140 °C, substrate pre-set temperature of 20 °C, and paraffin wax material of HNP-9. Calculation result is presented in Fig. 6.8, in which the values of *E*/*N* for the drop height of 100 mm is 0.33 larger than that of 50 mm. It suggests that the increase of drop height (impact velocity) reduces the degree of stress relaxation at the interface. This is because the higher impact velocity leads to larger amount of liquid penetrating into surface cavities of substrate, and results in the larger contact area and the higher adhesion strength at the interface. This result is also in good agreement with actual thermal spraying [119].

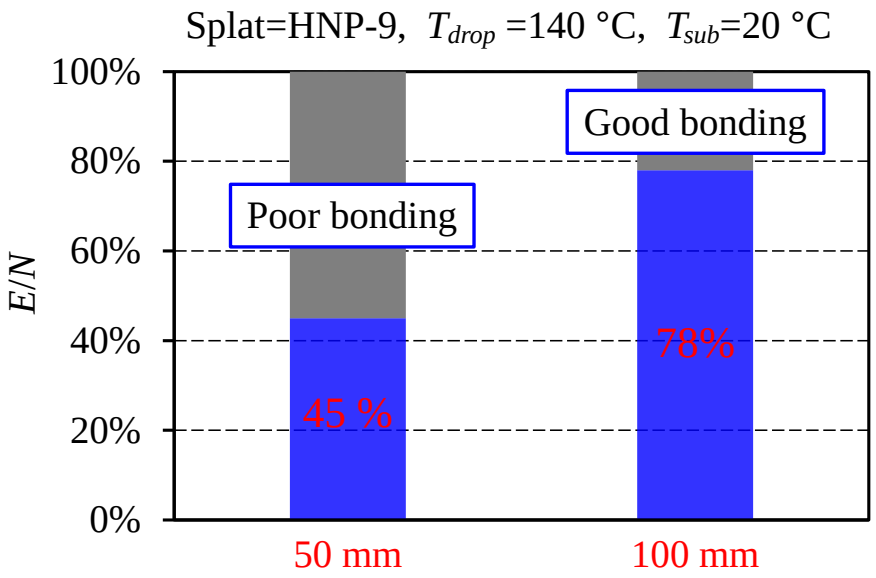

Fig. 6.8 Comparison of values of *E*/*N* for drop heights of 50 mm and 100 mm at the droplet temperature of 140 °C, substrate pre-set temperature of 20 °C, and paraffin wax material of HNP-9.

6.6 Guidance for optimizing thermal spraying process

During the actual thermal spraying process for TBCs, vertical cracking and debonding are the two main fracture phenomena dominating their failure. The vertical cracking often takes place in the coating due to the in-plane normal stress, while interfacial debonding often initiates from the thermally grown oxide as a stress raiser [120]. Generally, the vertical cracking occurs more easily at a lower substrate pre-heating temperature due to larger radial stress in the coating [121]. The tensile axial stress (peeling stress) at the interface, which may cause a progressive delamination, also becomes larger at a lower substrate pre-heating temperature [122]. In the model experiments of this dissertation, the observed splat phenomena showed good agreement with fracture phenomena in actual thermal spraying. For instance, the cracking took place in a candle wax splat at a relatively lower substrate pre-set temperature due to larger splat stress (see Fig. 3.8). Interfacial debonding was observed in both paraffin wax materials (see Fig. 3.13), and initiated at the interface near the free edge of the splat (see Fig. 3.10, Fig. 3.14, Fig. 5.7). These fracture behaviors are very similar to those in actual thermal spraying.

To improve the service life of TBCs, one of the most preliminary and critical issues is to reduce the residual normal stress in the coating material, and thereby control the initiation of vertical cracking and interfacial debonding in TBC system. According to the experiments and discussions, residual stress is significantly influenced by the material properties of the coating and drop impact conditions. First of all, the residual stress level in a coating decreases with the reduction of Young's modulus and reduction of the melting point of the coating. Lower residual stress is also achieved under a lower substrate pre-set temperature, a lower drop height, a lower droplet temperature, and a higher melting point of droplet, which always induce weaker interfacial bonding. To understand more in-depth and detailed information for optimizing thermal spraying process, further experiments are required to consider additional parameters, such as material and surface morphology of substrate, interaction within impacted splats, and re-melting/re-solidification of impacted splats. Also, FEM calculations are necessary to accurately

evaluate the stress-strain evolution during the cooling process by considering thermal resistance at the splat/substrate interface and actual interfacial bonding mechanisms.

6.7 Summary

In this Chapter, coupled thermo-mechanical analysis was performed to calculate the evolution of residual strain and substrate temperature during drop experiment. Creep of paraffin splat was considered by using a strain hardening form of creep law. Effect of interfacial adhesion was then investigated by comparing the simulation results and experimental results of residual strains. The main conclusions are as follows.

- Numerical result of temperature rise of substrate was higher than experimental result. It is because thermal resistance at splat/substrate interface slows down the thermal conduction through the interface, and was not considered in the simulation.
- When the creep was not considered, calculated residual strains were 2.2 to 3.2 times larger than experimental measurements for candle wax and HNP-9, respectively. While the calculation results changed to 1.5 to 2.2 times over the experimental results when the creep of splat was considered.
- Comparison between experimental and numerical results of residual strains suggested that lower melting point, higher droplet initial temperature, and higher drop height result in better splat/substrate interfacial adhesion, and hence less stress relaxation at the interface.

Chapter 7
Conclusions

A model experiment using paraffin wax was carried out to evaluate stress-strain evolution and fracture behaviors during thermal spraying. Experimental variables were (A) substrate pre-set temperature, (B) drop height, (C) Droplet temperature, and (D) paraffin wax material. Evolutions of residual strain and substrate temperature were measured during the drop experiments under various experimental conditions. Cracking and debonding behaviors of solidified splats were also observed, considering the effects of four drop impact conditions. The adhesion strength of solidified splat was then measured by using a scraping method with consideration of the effects of drop impact conditions and residual stress.

The driving forces for cracking and debonding during the drop experiments were evaluated through an elastic FE analysis. Calculation results of radial stress in splat and interfacial stresses provided reasonable explanations for the cracking and debonding behaviors observed during the drop experiments. The evolution of residual strain during the drop experiment was then calculated with a coupled thermo-mechanical analysis. The effect of creep was considered using a strain hardening creep model in which the creep properties were measured by a four-point bending creep method. On the basis of the coupled thermo-mechanical analysis results, the effect of creep and splat/substrate interfacial adhesion on residual strain was evaluated with the respect to the influences of several experimental conditions. The conclusions derived from the experimental and numerical investigations are summarized as follows:

- Tensile residual strain was generated at the substrate back surface due to shrinkage of the splat during its solidification and cooling process. Larger residual strains were measured at the lower substrate pre-set temperatures, lower drop height, and lower droplet temperature when neither cracking nor debonding occurred. Larger residual

strains were measured in the drop experiments for HNP-9 compared with candle wax which was mainly attributed to the difference in material properties and splat geometries.

- Splat stress increased with the reduction of substrate pre-set temperature. Cracking occurred in the candle wax splat when the substrate pre-set temperature was below 10 °C due to increased splat stress that might exceed the tensile strength of paraffin wax. While, cracking was never observed in HNP-9 splats since the residual stress never exceeded its tensile strength.

- Debonding was observed in both candle wax and HNP-9, and was more likely to occur at lower substrate pre-set temperature, lower drop height, and lower droplet temperature. This is governed by both the interfacial adhesion strength and the values of driving forces. A parameter, K_0 which eliminates the effect of splat geometry was defined and measured by a scraping method to evaluate the adhesion strength of solidified splat. Smaller K_0 values were measured at lower substrate pre-set temperature, lower drop height, and lower droplet temperature. These tendencies successfully explained the debonding behaviors during drop experiments. The level of residual tensile stresses in splats was controlled by stress relaxation treatment in order to examine its effect on the interfacial adhesion strength. The scraping test results suggested that the residual stresses facilitate the cracking to propagate along the interface, thereby reducing the measured scraping forces.

- Results of elastic finite element analysis indicated that larger peeling stresses and shear stresses are generated at lower droplet temperature and lower drop height. It explains the debonding behaviors observed in the drop impact test well.

- Evolutions of residual strain and substrate temperature during the drop experiment were calculated by a coupled thermo-mechanical analysis. Calculated residual strains were 2.2 to 3.2 times larger than experimental measurements for candle wax and HNP-9, respectively when the creep was ignored. The calculation results became 1.5 to 2.2 times over the experimental results when the creep was considered by employing a strain hardening form of creep law.

- Comparison between experimental results and coupled thermo-mechanical analysis results suggested that lower melting point, higher droplet temperature, and higher drop height result in better splat/substrate interfacial adhesion, and hence less stress relaxation at the interface.

In this dissertation, an original methodology was developed to investigate and examine the manufacturing processes of thermal spraying used in producing thermal sprayed coatings at the splat level. The fundamental mechanisms of splat deposition, including impact, adhesion, stress-strain evolution, and cracking and debonding creation were fully investigated. The phenomena of single splats deposition are usually difficult to observe and investigate in the field of thermal spraying. This study provides a possible method to study the process of splat deposition, especially in stress evolution and fracture creation. Effects of several drop impact conditions on residual stress and fracture behaviors were fully studied, and the results can provide scientific suggestions to the actual thermal spraying techniques. The obtained results and the research methods proposed in this dissertation may also contribute to other industrial fields, such as casting, welding, warm spraying, ink-jet printing, and additive manufacturing, in which thermal stress is usually generated due to solidification and cooling of the materials.

Although the understanding of stress evolution and fracture behaviours of solidified splats have been improved according to the current results, further work is still required to solve several unknown issues. First of all, the impact process of splats, including flattening, recoiling, and solidification on the substrate is needed to numerically calculated. Because this can help to predict and control the geometry of deposited splats according to the initial impact conditions. The calculated splat geometry can also be utilized to perform FEM simulation so that the stress-strain and possible fractures can be predicted without any experiments. In addition, in-depth research is required to study the fluid-solid interaction at interfaces. Especially, the interfacial bonding mechanisms and the effect on stress generation and fracture creation demand further experimental and numerical research.

References

[1] P.K. Rohatgi, R. Asthana, S. Das, Solidification, structures, and properties of cast metal-ceramic particle composites, Int. Met. Rev. 31 (1986) 115–139.

[2] A.A. Keste, S.H. Gawande, C. Sarkar, Design optimization of precision casting for residual stress reduction, J. Comput. Des. Eng. 3 (2016) 140–150.

[3] D. Deng, FEM prediction of welding residual stress and distortion in carbon steel considering phase transformation effects, Mater. Des. 30 (2009) 359–366.

[4] P. Knoedel, S. Gkatzogiannis, T. Ummenhofer, Practical aspects of welding residual stress simulation, J. Constr. Steel Res. 132 (2017) 83–96.

[5] M. Megahed, H.W. Mindt, N. N'Dri, H. Duan, O. Desmaison, Metal additive-manufacturing process and residual stress modeling, Integr. Mater. Manuf. Innov. 5 (2016) 61–93..

[6] B.A. Szost, S. Terzi, F. Martina, D. Boisselier, A. Prytuliak, T. Pirling, M. Hofmann, D.J. Jarvis, A comparative study of additive manufacturing techniques: Residual stress and microstructural analysis of CLAD and WAAM printed Ti-6Al-4V components, Mater. Des. 89 (2016) 559–567.

[7] P. Fauchais, A. Vardelle, B. Dussoubs, Quo Vadis Thermal Spraying? J. Therm. Spray Technol. 10 (2001) 44–66.

[8] S. Sampath, X.Y. Jiang, J. Matejicek, L. Prchlik, A. Kulkarni, A. Vaidya, Role of thermal spray processing method on the microstructure, residual stress and properties of coatings: An integrated study of Ni-5 wt. % Al bond coats, Mater. Sci. Eng. A. 364 (2004) 216–231.

[9] B. Choudhury, M. Chandrasekaran, Investigation on welding characteristics of aerospace materials - A review, Mater. Today Proc. 4 (2017) 7519–7526.

[10] D. Jiang, Q. Zhang, M. Zhao, H. Xia, S. Wang, Y. Li, Effects of welds distribution and high-low temperature humidity alternating aging on sealing performance of weld-bonded stainless steel structures, J. Manuf. Process. 48 (2019) 77–85.

[11] K.M. Hong, Y.C. Shin, Prospects of laser welding technology in the automotive industry: A review, J. Mater. Process. Technol. 245 (2017) 46–69.

[12] C. Hull, M. Feygin, Y. Baron, R. Sanders, E. Sachs, A. Lightman, T. Wohlers, Rapid prototyping: Current technology and future potential, Rapid Prototyp. J. 1 (1995) 11–19.

[13] H.N. Chia, B.M. Wu, Recent advances in 3D printing of biomaterials, J. Biol. Eng. 9.1 (2015) 1–14.

[14] B. Liang, C. Ding, Thermal shock resistances of nanostructured and conventional zirconia coatings deposited by atmospheric plasma spraying, Surf. Coat. Technol. 197 (2005) 185–192.

[15] M. Oksa, E. Turunen, T. Suhonen, T. Varis, S.P. Hannula, Optimization and characterization of high velocity oxy-fuel sprayed coatings: Techniques, materials, and applications, Coatings. 1 (2011) 17–52.

[16] J.B. Cheng, X.B. Liang, B.S Xu, Y.X Wu, Formation and properties of Fe-based amorphous/nanocrystalline alloy coating prepared by wire arc spraying process, J. Non. Cryst. Solids. 355 (2009) 1673–1678.

[17] A. Killinger, M. Kuhn, R. Gadow, High-Velocity Suspension Flame Spraying (HVSFS), a new approach for spraying nanoparticles with hypersonic speed, Surf. Coat. Technol. 201 (2006) 1922–1929.

[18] L. Gannon, Y. Liu, N. Pegg, M.J. Smith, Effect of welding-induced residual stress and distortion on ship hull girder ultimate strength, Mar. Struct. 28 (2012) 25–49.

[19] W. Cui, A.E. Mansour, Effects of welding distortions and residual stresses on the ultimate strength of long rectangular plates under uniaxial compression, Mar. Struct. 11 (1998) 251–269.

[20] S. Oukach, H. Hamdi, M. El Ganaoui, B. Pateyron, Thermo-mechanical simulation of residual stresses in plasma sprayed coatings, Appl. J. Envir. Eng. Sci. 2 (2018) 270–281.

[21] N.P. Padture, M. Gell, E.H. Jordan, Thermal barrier coatings for gas-turbine engine applications, Science, 296 (2002) 280–284.

[22] C. Li, X. Zhang, Y. Chen, J. Carr, S. Jacques, J. Behnsen, M. di Michiel, P. Xiao, R. Cernik, Understanding the residual stress distribution through the thickness of atmosphere plasma sprayed (APS) thermal barrier coatings (TBCs) by high energy synchrotron XRD; digital image correlation (DIC) and image based modelling, Acta Mater. 132 (2017) 1–12.

[23] S. Kuroda, T. Fukushima, S. Kitahara, Significance of quenching stress in the cohesion and adhesion of thermally sprayed coatings, J. Therm. Spray Technol. 1 (1992) 325–332.

[24] M. Arai, E. Wada, K. Kishimoto, Residual Stress Analysis of Ceramic Thermal Barrier Coating Based on Thermal Spray Process, J. Solid Mech. Mater. Eng. 1 (2007) 1251–1261.

[25] R. Vaßen, M.O. Jarligo, T. Steinke, D.E. Mack, D. Stöver, Overview on advanced thermal barrier coatings, Surf. Coat. Technol. 205 (2010) 938–942.

[26] M. Białas, Finite element analysis of stress distribution in thermal barrier coatings. Surf. Coat. Technol. 202 (2008) 6002–6010.

[27] M. Sebastiani, G. Bolelli, L. Lusvarghi, P.P. Bandyopadhyay, E. Bemporad, High resolution residual stress measurement on amorphous and crystalline plasma-sprayed single-splats, Surf. Coat. Technol. 206 (2012) 4872–4880.

[28] R. Devasia, A. Painuly, D. Devapal, K.J. Sreejith, Continuous fiber reinforced ceramic matrix composites, Fiber Reinforced Composites, 22 (2021) 669–795.

[29] G. Mehboob, M.J. Liu, T. Xu, S. Hussain, G. Mehboob, A. Tahir, A review on failure mechanism of thermal barrier coatings and strategies to extend their lifetime, Ceram. Int. 46 (2020) 8497–8521.

[30] X. Qiao, Y.M. Wang, W.X. Weng, B.L. Liu, Q. Li, Influence of pores on mechanical properties of plasma sprayed coatings: Case study of YSZ thermal barrier coatings, Ceram. Int. 44 (2018) 21564–21577.

[31] J. Jiang, D. Wu, W. Wang, X. Zhao, X. Ma, B. Wang, H.J. Shi, Fracture behavior of TBCs with cooling hole structure under cyclic thermal loadings, Ceram. Int. 46 (2020) 3644–3654.

[32] A.A. Abubakar, A.F.M. Arif, S.S. Akhtar, Evolution of internal cracks and residual stress during deposition of TBC, Ceram. Int. 46 (2020) 26731–26753.

[33] G.G. Stoney, The tensions of metallic films deposited by electrolysis, Proc. R. Soc. Lond. Ser. A, 82 (1909) 172–175.

[34] S. Kuroda, T. Fukushima, S. Kitahara, Simultaneous measurement of coating thickness and deposition stress during thermal spraying, Thin Solid Films, 164 (1988) 157–163.

[35] S. Kuroda, T. Dendo, S. Kitahara, Quenching stress in plasma sprayed coatings and its correlation with the deposit microstructure, J. Therm. Spray Technol. 4 (1995) 75–84.

[36] J. Matejicek, S. Sampath, In situ measurement of residual stresses and elastic moduli in thermal sprayed coatings part 1: Apparatus and analysis, Acta Mater. 51 (2003) 863–872.

[37] J. Matejicek, S. Sampath, D. Gilmore, R. Neiser, In situ measurement of residual stresses and elastic moduli in thermal sprayed coatings part 2: Processing effects on properties of Mo coatings, Acta Mater. 51 (2003) 873–885.

[38] S. Sampath, V. Srinivasan, A. Valarezo, A. Vaidya, T. Streibl, Sensing, control, and in situ measurement of coating properties: An integrated approach toward

establishing process-property correlations, J. Therm. Spray Technol. 18 (2009) 243–255.

[39] J. Matejicek, S. Sampath, Intrinsic residual stresses in single splats produced by thermal spray processes, Acta Mater. 49 (2001) 1993–1999.

[40] J. Pina, A. Dias, J.L. Lebrun, Study by X-ray diffraction and mechanical analysis of the residual stress generation during thermal spraying, Mater. Sci. Eng. A. 347 (2003) 21–31.

[41] F. Fanicchia, X. Maeder, J. Ast, A.A. Taylor, Y. Guo, M.N. Polyakov, J. Michler, D.A. Axinte, Residual stress and adhesion of thermal spray coatings : Microscopic view by solidification and crystallisation analysis in the epitaxial CoNiCrAlY single splat, Mater. Des. 153 (2018) 36–46.

[42] M. Mellali, P. Fauchais, A. Grimaud, Influence of substrate roughness and temperature on the adhesion/cohesion of alumina coatings, Surf. Coat. Technol. 81 (1996) 275–286.

[43] V.V. Sobolev, J.M. Guilemany, J. Nutting, J.R. Miquel, Development of substrate-coating adhesion in thermal spraying, Int. Mater. Rev. 42 (1997) 117–136.

[44] M.H. Staia, E. Ramos, A. Carrasquero, A. Roman, J. Lesage, D. Chicot, G. Mesmacque, Effect of substrate roughness induced by grit blasting upon adhesion of WC-17% Co thermal sprayed coatings, Thin Solid Films, 377 (2000) 657–664.

[45] Y. Okajima, M. Sakaguchi, H. Inoue, A finite element assessment of influential factors in evaluating interfacial fracture toughness of thermal barrier coating, Surf. Coat. Technol. 313 (2017) 184–190.

[46] F. Zhou, Z. Zhang, S. Liu, L. Wang, J. Jia, Y. Wang, X. Gong, J. Gou, C. Deng, M. Liu, Effect of heat treatment and synergistic rare-earth modified NiCrAlY on bonding strength of nanostructured 8YSZ coatings, Appl. Surf. Sci. 480 (2019) 636–645.

[47] C.R.C. Lima, J.M. Guilemany, Adhesion improvements of Thermal Barrier Coatings with HVOF thermally sprayed bond coats, Surf. Coat. Technol. 201 (2007) 4694–4701.

[48] A. Vencl, S. Arostegui, G. Favaro, F. Zivic, M. Mrdak, S. Mitrović, V. Popovic, Evaluation of adhesion/cohesion bond strength of the thick plasma spray coatings by scratch testing on coatings cross-sections, Tribol. Int. 44 (2011) 1281–1288.

[49] ASTM D4541–17, Standard test method for pull-off strength of coatings using portable Adhesion testers, ASTM International, West Conshohocken.

[50] ASTM C633–13, Standard test method for adhesion or cohesion strength of thermal spray coatings, ASTM International, West Conshohocken.

[51] E.E. Balić, M. Hadad, P.P. Bandyopadhyay, J. Michler, Fundamentals of adhesion of thermal spray coatings: Adhesion of single splats, Acta Mater. 57 (2009) 5921–5926.

[52] D. Goldbaum, J.M. Shockley, R.R. Chromik, A. Rezaeian, S. Yue, J.G. Legoux, E. Irissou, The effect of deposition conditions on adhesion strength of Ti and Ti6Al4V cold spray splats, J. Therm. Spray Technol. 21 (2012) 288–303.

[53] S.Y. Chen, G.Z Ma, H.D Wang, P.F He, H.M Wang, M. Liu, Evaluation of adhesion strength between amorphous splat and substrate by micro scratch method, Surf. Coat. Technol. 344 (2018) 43–51.

[54] A.K. Keshri, D. Lahiri, A. Agarwal, Carbon nanotubes improve the adhesion strength of a ceramic splat to the steel substrate, Carbon, 49 (2011) 4340–4347.

[55] R.R. Chromik, D. Goldbaum, J.M. Shockley, S. Yue, E. Irissou, J.G. Legoux, N.X. Randall, Modified ball bond shear test for determination of adhesion strength of cold spray splats, Surf. Coat. Technol. 205 (2010) 1409–1414.

[56] V.N.V. Munagala, S.I. Imbriglio, R.R. Chromik, The influence of powder properties on the adhesion strength and microstructural evolution of cold sprayed Ti6Al4V single splats, Mater. Lett. 244 (2019) 58–61.

[57] M. Murakawa, S. Takeuchi, Quantitative adhesion strength measurement of diamond coatings, Thin Solid Films, 181 (1989) 443–450.

[58] Z. Xie, J. Zhu, W. Guo, Scraping test and adhesion measurements of diamond and nickel electroless coatings, Mater. Charact. 44 (2000) 347–352.

[59] K. Shimamoto, S. Batorova, K. Houjou, H. Akiyama, C. Sato, Accelerated test method for water resistance of adhesive joints by interfacial cutting of open-faced specimens, J. Adhes. 97 (2021) 1255–1270.

[60] A.M. Worthington, On the forms assumed by drops of liquids falling vertically on a horizontal plate, Proc. R. Soc. Lond. 25 (1877) 261–272.

[61] Y.S. Joung, C.R. Buie, Aerosol generation by raindrop impact on soil, Nat. Commun. 6.1 (2015) 1–9.

[62] V. Bergeron, D. Bonn, J.Y. Martin, L. Vovelle, Controlling droplet deposition with polymer additives, Nature, 405.6788 (2000) 772–775.

[63] M. Singh, H.M. Haverinen, P. Dhagat, G.E. Jabbour, Inkjet printing — Process and its applications, Adv. Mater. 22 (2010) 673–685.

[64] E. Tekin, P.J. Smith, U.S. Schubert, Inkjet printing as a deposition and patterning tool for polymers and inorganic particles, Soft Matter. (2008) 703–713.

[65] D.B.V Dam, C.L. Clerc, Experimental study of the impact of an ink-jet printed droplet on a solid substrate, Phys. Fluids. 16 (2004) 3403–3414.

[66] R. Mcpherson, On the formation of thermally sprayed alumina coatings, J. Mater. Sci. 15 (1980) 3141–3149.

[67] P. Fauchais, Understanding plasma spraying, J. Phys. D. Appl. Phys. 37 (2004) 86–108.

[68] Z. Levin, P.V. Hobbs, Splashing of water drops on solid and wetted surfaces: hydrodynamics and charge separation, Philos. Trans. Royal Soc. A, 269 (1971) 555–585.

[69] C. Mundo, M. Sommerfeld, C. Tropeal, Droplet-wall collisions: experimental studies of the deformation and breakup process, Int. J. Multiphase Flow, 21 (1995) 151–173.

[70] F.J. Heymann, On the shock wave velocity and impact pressure in high-speed liquid-solid impact, J. Basic Eng. 90 (1968) 400–402.

[71] I.V. Roisman, R. Rioboo, C. Tropea. Normal impact of a liquid drop on a dry surface: model for spreading and receding, Proc. R. Soc. Lond. A. 458 (2002) 1411–1430.

[72] C. Ukiwe, D.Y. Kwok, On the maximum spreading diameter of impacting droplets on well-prepared solid surfaces, Langmuir. 21 (2005) 666–673.

[73] T.W. Clyne, S.C. Gill, Residual stresses in thermal spray coatings and their effect on interfacial adhesion: A review of recent work, J. Therm. Spray Technol. 5 (1996) 401–418.

[74] M. Vardelle, A. Vardelle, A.C. Leger, P. Fauchais, D. Gobin, Influence of Particle Parameters at Impact on Splat Formation and Solidification in Plasma Spraying Processes, J. Therm. Spray Technol. 4 (1994) 50–58.

[75] K. Alamara, S. Saber-Samandari, P.R. Stoddart, C.C. Berndt, Effect of substrate temperature on the splat formation of flame sprayed polypropylene, Surf. Coat. Technol. 206 (2011) 1180–1187.

[76] R.G. Azar, S. Shakeri, S. Chandra, J. Mostaghimi, Interactions between molten metal droplets impinging on a solid surface, Int. J. Heat Mass Transf. 46 (2003) 1395–1407.

[77] S. Chandra, C.T. Avedisian, Observations of droplet impingement on a ceramic porous surface, Int. J. Heat Mass Transf. 35 (1992) 2377–2388.

[78] M.P. Fard, R. Bhola, S. Chandra, J. Mostaghimi, Deposition of tin droplets on a steel: simulations and experiments, Int. J. Heat Mass Transf. 41 (1998) 2929–2945.

[79] M. Bussmann, S. Chandra, J. Mostaghimi, Numerical results of off-angle thermal spray particle impact, ITSC99 Proc. 783 (1999) 783–786.

[80] R. Bhola, S. Chandra, Parameters controlling solidification of molten wax droplets falling on a solid surface, J. Mater. Sci. 34 (1999) 4883–4894.

[81] S. Dadvar, S. Chandra, N. Ashgriz, Adhesion of wax droplets to porous polymer surfaces, J. Adhes. 91 (2014) 538–555.

[82] Y. Saito, K. Saito, T. Atake, Theoretical analysis of heat-flux differential scanning calorimetry based on a general model, Thermochim. Acta, 99 (1986) 299–307.

[83] W.J. Parker, R.J. Jenkins, C.P. Butler, G.L Abbott, Flash method of determining thermal diffusivity, heat capacity, and thermal conductivity. J. Appl. Phys. 32 (1961) 1679–1684.

[84] ASTM D6272–17, Standard test method for flexural properties of unreinforced and reinforced plastics and electrical insulating materials by four-point bending, ASTM International, West Conshohocken.

[85] A. Nechache, A.H. Bouzid, Creep analysis of bolted flange joints, Int. J. Press. Vessels Pip. 84 (2007) 185–194.

[86] J. Betten, Creep mechanics, Springer Science & Business Media, 2008.

[87] Abaqus, Version. "6.14 Documentation." Dassault Systemes Simulia Corporation 651 (2014).

[88] S.P Timoshenko, Strength of materials. Part II. Advanced theory and problems, New York: D, 1930.

[89] A. Amano, M. Sakaguchi, Y. Kurokawa, Y. Okajima, H. Inoue, Measurement of quenching strain in paraffin drop test modelling thermal spray process, Trans. JSME (in Japanese) 83 (2017) 1–14, https://doi.org/10.1299/transjsme.17-00377.

[90] S.D. Aziz, S. Chandra, Impact, recoil and splashing of molten metal droplets, Int. J. Heat Mass Transf. 43 (2000) 2841–2857.

[91] M.P. Fard, V. Pershin, S. Chandra, J. Mostaghimi, Splat shapes in a thermal spray coating process : simulations and experiments, J. Therm. Spray Technol. 11 (2002) 206–217.

[92] M. Bussmann, J. Mostaghimi, S. Chandra, On a three-dimensional volume tracking model of droplet impact, Phys. Fluids. 11 (1999) 1406–1417.

[93] M.P. Fard, S. Chandra, J. Mostaghimi, A three-dimensional model of droplet impact and solidification, Int. J. Heat Mass Transf. 45 (2002) 2229–2242.

[94] M.P. Fard, Y.M. Qiao, S. Chandra, J. Mostaghimi, Capillary effects during droplet impact on a solid surface, Phys. Fluids 8 (1996) 650–659.

[95] P. Nautiyal, C. Zhang, B. Boesl, A. Agarwal, Interfacial deformation and failure mechanisms at the single-splat length scale revealed in-situ by indentation of cold sprayed aluminum microparticles, Mater. Sci. Eng. A, 824 (2021) 141828.

[96] R. Ghasemi, H. Vakilifard, Plasma-sprayed nanostructured YSZ thermal barrier coatings: thermal insulation capability and adhesion strength, Ceram. Int. 43.12 (2017) 8556–8563.

[97] Z. Mohammadi, A.A. Ziaei-Moayyed, A. S.M. Mesgar, Grit blasting of Ti–6Al–4V alloy: Optimization and its effect on adhesion strength of plasma-sprayed hydroxyapatite coatings, J. Mater. Process. Technol. 194 (2007) 15–23.

[98] P. Fauchais, M. Fukumoto, A. Vardelle, M. Vardelle, Knowledge concerning splat formation: an invited review, J. Therm. Spray Technol. 13 (2004) 337–360.

[99] Y. Nishimatsu, The mechanics of rock cutting, Int. J. Rock Mech. Min. Sci. 9 (1972) 261–270.

[100] M.E. Merchant, Mechanics of the metal cutting process. I. Orthogonal cutting and a type 2 chip, J. Appl. Phys. 16 (1945) 267–275.

[101] D.A. Stephenson, J.S. Agapiou, Metal cutting theory and practice, 3rd edition, CRC press, 2016, p. 418.

[102] S. Chinchanikar, S.K. Choudhury, Effect of work material hardness and cutting parameters on performance of coated carbide tool when turning hardened steel: An optimization approach, Measurement, 46 (2013) 1572–1584.

[103] J.S. Jadhav, B.R. Jadhav, Experimental study of effect of cutting parameters on cutting force in turning process, Int. J. Innov. Res. Adv. Eng. 1 (2014) 240–248.

[104] A. Kumar, M.M. Mahapatra, P.K. Jha, Effect of machining parameters on cutting force and surface roughness of in situ Al–4.5%Cu/TiC metal matrix composites, Measurement, 48 (2014) 325–332.

[105] Metals Handbook, American Society for Metals, Cleveland, Ohio, USA, 1948.

[106] E. Suhir, Analysis of interfacial thermal stresses in a trimaterial assembly, Int. J. Appl. Phys. 89 (2001) 3685–3697.

[107] W.L. Yin, Interfacial Thermal Stresses in Layered Structures: The Stepped Edge Problem, J. Electron. Packag. 117 (1995) 153–158.

[108] Y. Feng, L. Wu, Analysis of interfacial thermal stresses of chip-substrate structure, Int. J. Solids Struct. 38 (2001) 1551–1562.

[109] E. Suhir, Predicted thermal stresses in a bimaterial assembly adhesively bonded at the ends, Int. J. Appl. Phys. 89.1 (2001) 120–129.

[110] The Engineering ToolBox, https://www.engineeringtoolbox.com/convective-heat-transfer-d_430.html, (accessed 25 November 2021).

[111] L. Wang, X.H. Zhong, Y.X. Zhao, J.S. Yang, S.Y. Tao, W. Zhang, Y. Wang, X.G. Sun, Effect of interface on the thermal conductivity of thermal barrier coatings: A numerical simulation study, Int. J. Heat Mass Transf. 79 (2014) 954–967.

[112] K.S. Ravichandran, K. An, R.E. Dutton, S.L. Semiatin, Thermal Conductivity of Plasma-Sprayed Monolithic and Multilayer Coatings of Alumina and Yttria-Stabilized Zirconia, J. Am. Ceram. Soc. 82 (1999) 673–682.

[113] C.M. Heveran, J. Xu, V.K. Sarin, S.N. Basu, Simulation of stresses in TBC – EBC coating systems for ceramic components in gas turbines, Surf. Coat. Technol. 235 (2013) 354–360.

[114] K. Sfar, J. Aktaa, D. Munz, Numerical investigation of residual stress fields and crack behavior in TBC systems, Mater. Sci. Eng. A, 333 (2002) 351–360.

[115] S. Sampath, X.Y. Jiang, J. Matejicek, A.C. Leger, A. Vardelle, Substrate temperature effects on splat formation , microstructure development and properties of plasma sprayed coatings Part I: Case study for partially stabilized zirconia, Mater. Sci. Eng. A, 272 (1999) 181–188.

[116] X. Jiang, J. Matejicek, S. Sampath, Substrate temperature effects on the splat formation, microstructure development and properties of plasma sprayed coatings Part II: case study for molybdenum, Mater. Sci. Eng. A, 272 (1999) 189–198.

[117] A. Vaidya, T. Streibl, L. Li, S. Sampath, O. Kovarik, R. Greenlaw, An integrated study of thermal spray process–structure–property correlations: A case study for plasma sprayed molybdenum coatings, Mater. Sci. Eng. A, 403 (2005) 191–204.

[118] X. Zhang, M. Watanabe, S. Kuroda, Effects of processing conditions on the mechanical properties and deformation behaviors of plasma-sprayed thermal barrier coatings : Evaluation of residual stresses and mechanical properties of thermal barrier coatings on the basis of in situ curvature measurement under a wide range of spray parameters, Acta Mater. 61 (2013) 1037–1047.

[119] W. Tillmann, L. Hagen, W. Luo, Process parameter settings and their effect on residual stresses in WC/W2C reinforced iron-based arc sprayed coatings, Coatings, (2017) 7.

[120] R. Xu, X. Fan, T.J. Wang, Mechanisms governing the interfacial delamination of thermal barrier coating system with double ceramic layers, Appl. Surf. Sci. 370 (2016) 394–402.

[121] K. Ito, H. Kuriki, M. Enoki, A numerical study on generation mechanism of vertical cracks in top coat of TBCs during APS deposition, J. Therm. Spray Technol. 24 (2015) 730–738.

[122] S. Widjaja, A.M. Limarga, T.H. Yip, Modeling of residual stresses in a plasma-sprayed zirconia/alumina functionally graded-thermal barrier coating, Thin Solid Films, 434 (2003) 216–227.

Appendix A

Estimation of interfacial thermal resistance

In Chapter 5 and Chapter 6, FE simulation is performed assuming the solidified splat to be bonded with the substrate perfectly. In the actual situation, imperfect bonding must exist and slow down the heat transfer through the interface. In Appendix A, interfacial thermal resistance between the splat and the substrate under different drop heights will be estimated by comparing the numerical results and experimental measurements of substrate temperature evolution. Effect of interface thermal resistance on residual strain will be discussed then.

Experimental measurements of temperature evolution at substrate back surface, T_1 is summarized in Fig. A.1 under different drop heights when paraffin wax is HNP-9, droplet temperature is 140 °C, and substrate pre-set temperature is 20 °C. Higher drop heights

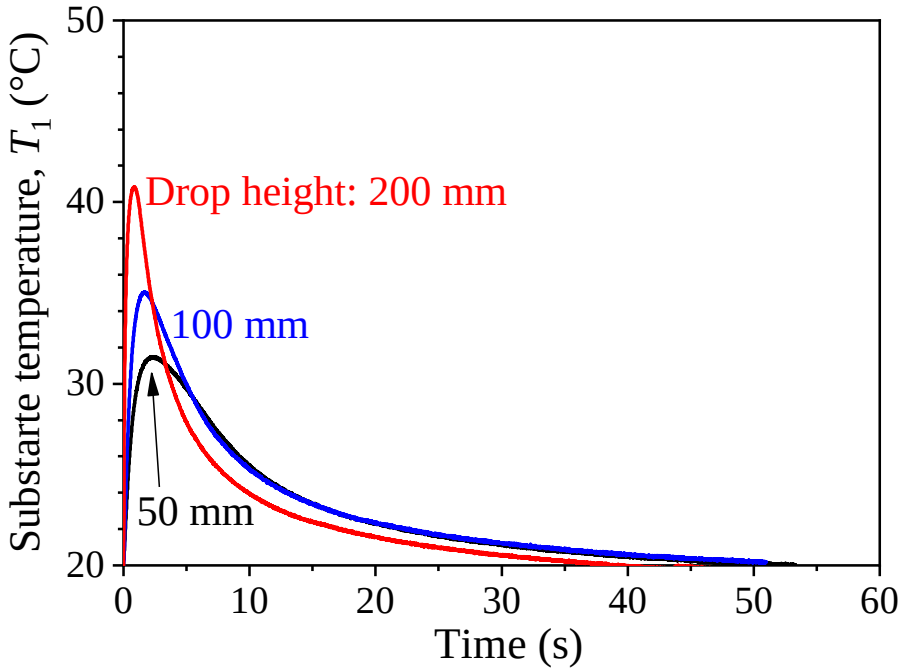

Fig. A.1 Experimental measurements of temperature evolution at substrate back surface under different drop heights.

lead to sharper temperature rising and larger maximum temperature, which might be caused by higher drop impact velocity and better interfacial bonding.

Because the interfacial thermal resistance is almost impossible to measure, several finite element simulations are performed changing the values of gap conductance ranging from 100 W/(m^2·K) to 1×10^7 W/(m^2·K) to find the most appropriate value. Here, gap conductance C_{gap} is determined as follows in ABAQUS,

$$q = C_{gap}\left(\theta_A - \theta_B\right), \tag{A.1}$$

where q means heat flux, θ_A and θ_B are the temperatures of splat and substrate at the interface, respectively. A larger C_{gap} means a better interfacial bonding with lower interfacial thermal resistance. It should be noted that the FE model used here is different from those in Chapter 5 and Chapter 6, in which the splat and the substrate share nodes at the interface. In Appendix A, the splat and the substrate belong to separate parts and a contact interaction is applied between splat bottom surface and substrate top surface in which sliding and detachment are not permitted during simulation.

Calculation results of substrate temperature evolutions are compared with experimental measurement in Fig. A.2 when drop height is 50 mm. It can be found that the numerical result predicts the experimental measurement best when C_{gap} is 400 W/(m^2·K). When drop heights are 100 mm and 200 mm, the numerical results predict experimental measurements best when C_{gap} are 800 W/(m^2·K) and 10000 W/(m^2·K), respectively as shown in Fig. A.3. Values of C_{gap} increase with the increase of drop height, and it suggests that a better interfacial bonding with faster interfacial heat transfer is achieved under a higher impact velocity.

Numerical results of residual strains are shown in Table A.1 when drop height is 50 mm. According to Fig. A.2, when C_{gap} is larger than 1×10^5 W/(m^2·K), the maximum value of substrate temperature does not change anymore. It means the effect of interfacial thermal resistance is very limited when C_{gap} is larger than 1×10^5 W/(m^2·K). According to Table

A.1, after considering the actual interfacial thermal resistance (C_{gap} = 400 W/(m^2·K)), the calculated residual strain decreases slightly, which might be caused by longer creep time of paraffin the splat during its cooling process.

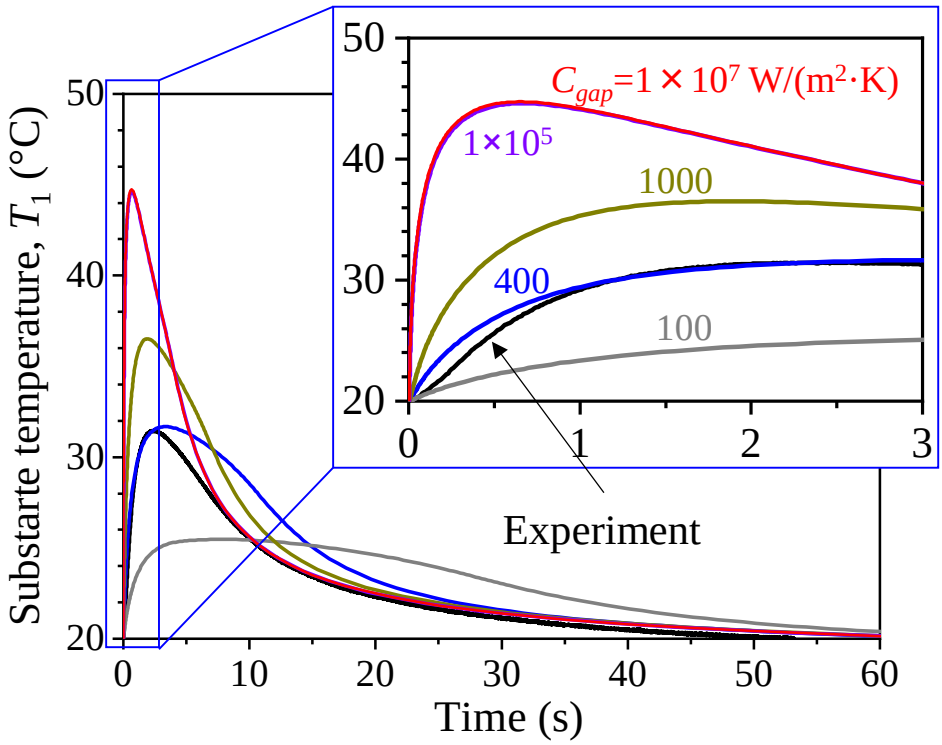

Fig. A.2 Comparison of experimental measurement and numerical results of substrate temperature evolutions when drop height is 50 mm. The other drop impact conditions are same with Fig. A.1.

Table A.1 Numerical results of residual strains when drop height is 50 mm. The other drop impact conditions are same with Fig. A.2.

C_{gap} (W/(m^2·K))	ε_r (μst)
1×10^7	58.14
400	57.26

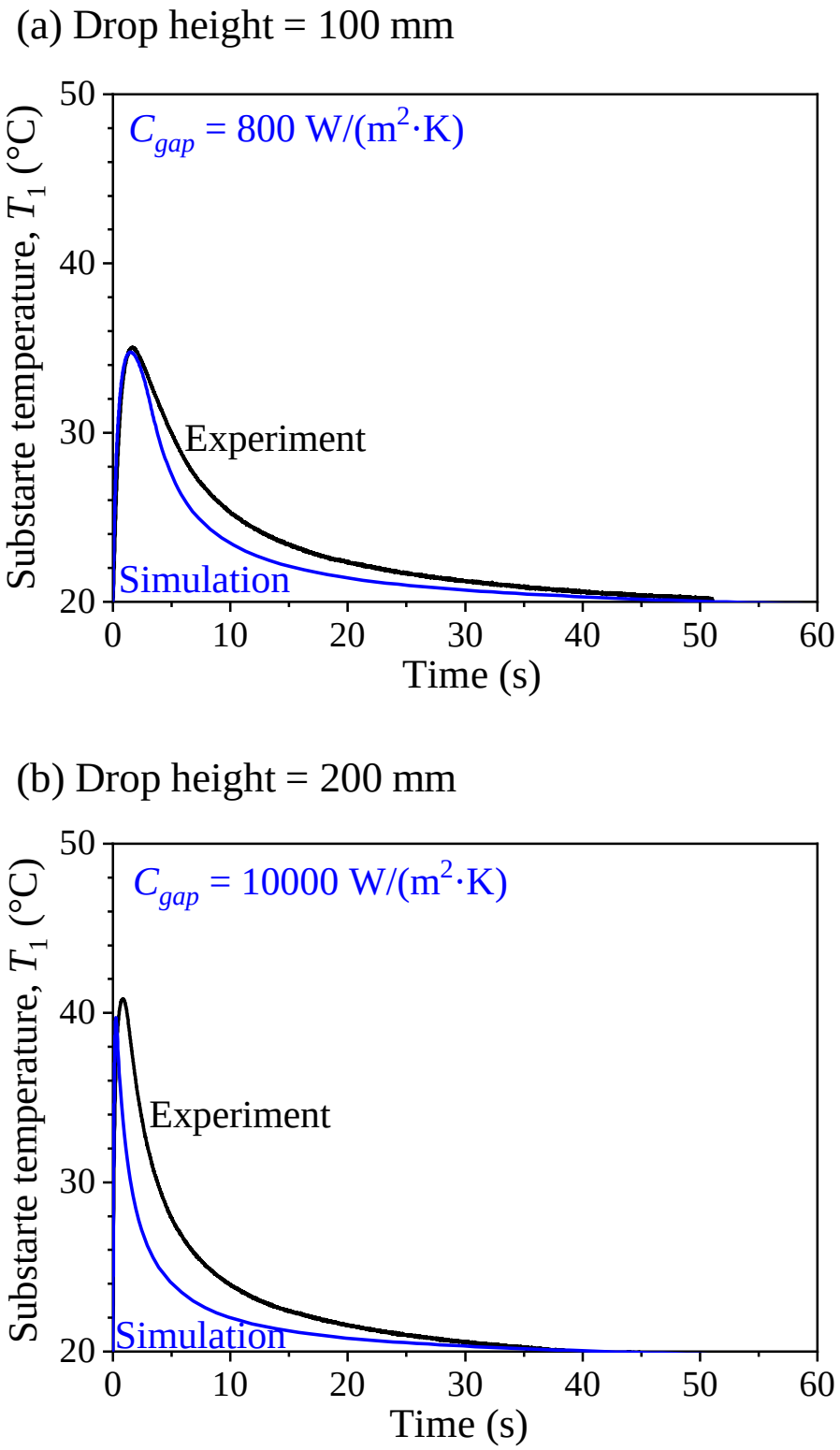

Fig. A.3 Comparison of experimental measurements and numerical results of substrate temperature evolutions when drop heights are (a) 100 mm and (b) 200 mm. The other drop impact conditions are same with Fig. A.1.

Appendix B

Estimation of heat transfer coefficient

In Chapter 6, only convective heat transfer coefficient is considered during the simulation and the heat transfer coefficient was assumed as 5 W/(m^2·K). In Appendix B, radiant heat transfer will be considered to estimate the total heat transfer coefficient of splat. And the results will be verified by comparing the numerical results with experimental results of substrate temperature evolutions.

First, coefficient of radiant heat transfer of splat is estimated. The radiative heat transfer rate, $\dot{Q}$ between splat and surrounding wall can be calculated by,

$$\dot{Q} = F_{splat\to sur}\frac{\sigma}{\dfrac{1}{\varepsilon_{splat}}+\dfrac{A_{splat}}{A_{sur}}\left(\dfrac{1}{\varepsilon_{sur}}-1\right)}A_{splat}\left(T_{splat}{}^4 - T_{sur}{}^4\right), \tag{B.1}$$

in which $F_{splat\to sur}$ is the view factor from splat to surrounding wall, σ is Stefan–Boltzmann constant, A_{splat} and A_{sur} are areas of splat and surrounding wall, ε_{splat} and ε_{sur} are emissivities of splat and surrounding wall. A_{splat} is assumed to be much smaller than A_{sur}. Coefficient of radiant heat transfer, h_r can be estimated as the following equation,

$$h_r = \frac{\dot{Q}}{\left(T_{splat}-T_{sur}\right)A_{splat}} = F_{splat\to sur}\varepsilon_{splat}\sigma\left(T_{splat}+T_{sur}\right)\left(T_{splat}{}^2+T_{sur}{}^2\right). \tag{B.2}$$

Here, values of $F_{splat\to sur}$ and ε_{splat} are assumed as 1 and 0.8, respectively. σ is 5.67×10^{-8} W/(m^2·K^4). The values of h_r can be finally calculated as 4.6-8.2 W/(m^2·K) when splat temperature changes from 20 °C to 140 °C during the drop test. Considering the convective heat transfer coefficient, the total heat transfer coefficient is expected to range

from 10 W/(m^2·K) to 20 W/(m^2·K). To verify the estimation result, temperature evolution at substrate back surface is numerically calculated changing the heat transfer coefficients between 5 W/(m^2·K) and 100 W/(m^2·K). According to Appendix A, C_{gap} is set as 400 W/(m^2·K). The calculation results are shown in Fig. B.1 along with experimental measurement when drop height is 50 mm. It can be found that the best prediction is achieved at a heat transfer coefficient of 10 W/(m^2·K).

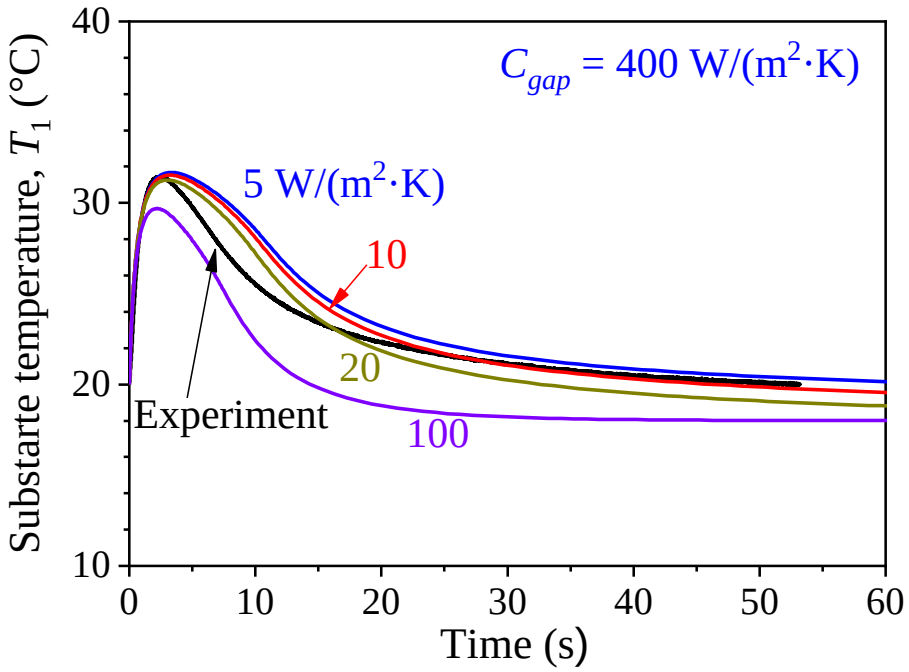

Fig. B.1 Comparison of experimental measurement and numerical results of substrate temperature evolutions changing the values of heat transfer coefficients when drop height is 50 mm. The other drop impact conditions are same with Fig. A.1.

List of publications

Journal papers

[1] Chao Kang, Motoki Sakaguchi, Akito Saito, and Hirotsugu Inoue. Adhesion strength of paraffin droplet impacted and solidified on metal substrate. *Results in Physics*. Vol. 34, pp. 105310, Mar. 2022.

[2] Chao Kang, Motoki Sakaguchi, and Hirotsugu Inoue. Contribution of creep to strain evolution in a paraffin droplet during and after rapid solidification on a metal substrate. *Surface and Coatings Technology*. Vol. 399, pp. 126145, Oct. 2020.

[3] Chao Kang, Motoki Sakaguchi, Ayumi Amano, Yu Kurokawa, and Hirotsugu Inoue. Quenching stress and fracture of paraffin droplet during solidification and adhesion on metallic substrate. *Surface and Coatings Technology*. Vol. 374, pp. 868-877, Sep. 2019.

International conferences

[1] Chao Kang, Motoki Sakaguchi, and Hirotsugu Inoue. A numerical study on creep deformation of a paraffin droplet impacted and solidified on a metal substrate. The 8th International Conference on Creep, Fatigue and Creep-Fatigue Interaction. Aug. 2021.

[2] Motoki Sakaguchi, Chao Kang, and Hirotsugu Inoue. Deformation and fracture during solidification and adhesion process of paraffin droplet modelling thermal spray. The 9th Global Conference on Materials Science and Engineering. Nov. 2020.

[3] Chao Kang, Motoki Sakaguchi, Akito Saito, and Hirotsugu Inoue. Cracking and delamination during solidification and adhesion process of paraffin droplet impacted on a metal substrate. 10th Japan-China Bilateral Symposium on High Temperature Strength of Materials. Oct. 2019.

[4] Chao Kang, Motoki Sakaguchi, Yu Kurokawa, and Hirotsugu Inoue. Quenching

strain and fractures during solidification and adhesion process of paraffin droplet. The 15th Asia-Pacific Conference on Fracture and Strength. Oct. 2018.

Domestic conferences

[1] Chao Kang, Motoki Sakaguchi, and Hirotsugu Inoue. Creep deformation during the solidification and adhesion process of a paraffin droplet. Proceedings of the 58th Symposium on Strength of Materials at High Temperatures. Dec. 2020. (In Japanese)

[2] Akito Saito, Motoki Sakaguchi, Chao Kang, Yu Kurokawa, and Hirotsugu Inoue. Effect of substrate temperature on stress development during solidification and adhesion process of molten paraffin dropped onto substrate. M&M2019, JSME. Nov. 2019. (In Japanese)

[3] Chao Kang, Motoki Sakaguchi, Akito Saito, Yu Kurokawa, and Hirotsugu Inoue. Quantitative evaluation of cracking and debonding behaviors during the impact, solidification and adhesion process of a paraffin droplet. Proceedings of the 69th JSMS Annual Meetings. May 2019. (In Japanese)

[4] Akito Saito, Motoki Sakaguchi, Chao Kang, Yu Kurokawa, and Hirotsugu Inoue. Solidification and adhesion of molten paraffin impacted on metal substrate and subsequent cracking and delamination of the solidified coating. M&M2018, JSME. Dec. 2018. (In Japanese)

[5] Chao Kang, Saito Saitou, Motoki Sakaguchi, Yu Kurokawa, and Hirotsugu Inoue. Stress and fracture during solidification and adhesion process of paraffin droplet impacted on metallic substrate (Effects of paraffin material and impact velocity). Proceedings of the 68th JSMS Annual Meetings. May 2018. (In Japanese)

Acknowledgments

First, I would like to express my deepest gratitude to my major supervisor Assoc. Prof. Motoki Sakaguchi for offering me this opportunity to complete my master's and doctoral studies at Tokyo Tech. Over the past four and a half years, it has been really fortunate for me to work with such an innovative and knowledgeable advisor, by whom I have been inspired and guided to become a better researcher. He has provided me with all the needed support, and has boosted my interest in scientific research. I would also like to extend my deepest gratitude to my co-supervisor Prof. Hirotsugu Inoue for his endless patience in teaching me, and for his invaluable suggestions on my research. The completion of my dissertation would not have been possible without the supervision of him. I am also very grateful to Assis. Prof. Yu Kurokawa for his valuable instructions and contributions to my research. His wide knowledge in both experimental design and numerical calculation has helped me a lot in completing this dissertation. My faithful appreciation also goes to my PhD examination committee: Prof. Akira Todoroki, Prof. Chiaki Sato, and Prof. Kazuyoshi Fushinobu, for their helpful advice and comments on my research.

Many thanks to Ayumi Amano and Akito Saito, my former colleagues at Inoue Sakaguchi Laboratory, who have taught me many experimental tips during the beginning stage of my research, and to all other colleagues, especially Junyao Zhou, Koichiro Mogi, Kota Chiya, Ikki Ikeda for the technical support. Special thanks to laboratory assistant staff Mihoko Yamada who has helped me a lot especially when I just joined Tokyo Tech as an international student, and to my colleague Shiyu Suzuki who has helped me a lot during my study at Tokyo Tech.

Finally, I will dedicate this dissertation to my parents, who are the most important people in my life. Without them I would never have any possibility to study abroad. Their unconditional and endless love, support, and faith have been encouraging and motivating me to move on during my PhD.